



LUND UNIVERSITY
Faculty of Science

Design, Construction and Characterization of a Portable Fast-Neutron Detector

Nicholai Mauritzson

Thesis submitted for the degree of Master of Science
Project duration: 9 months

Supervised by Kevin Fissum and Douglas Di Julio

Department of Physics
Division of Nuclear Physics
May 2017

Acknowledgements

This thesis has been authored following funding from the European Spallation Source ERIC (ESS). The project reported on in this thesis was carried out in association with the Neutron Optics and Shielding Group of ESS. Support was also given from the Detector Group of ESS. The Source Testing Facility (STF) and the Source-based Neutron Irradiation Group (SONNIG) at the Department of Nuclear Physics, Lund University, Sweden graciously hosted the experiments.



Sonnig

Abstract

At European Spallation Source ERIC, 2 GeV proton bunches will be accelerated towards a tungsten target where spallation will occur, producing a wide neutron energy spectrum. Despite the shielding and moderators in place to stop and/or reduce their energy, a significant portion of the most energetic neutrons, called prompt neutrons, might still reach the sample position of a neutron-scattering instrument. It has been previously shown that these prompt neutrons contribute to a degradation of the signal-to-noise ratio of the detectors. Clearly, a tool for identifying sources of fast-neutron background would be very valuable. The design goals of the envisioned Portable Fast-Neutron Diagnostic Detector include portability, durability, fast response and the ability for performing self-triggering time-of-flight measurements complete with tracking to localize fast-neutron sources. Within the context of this thesis, the detector system was conceptualized, designed and a prototype assembled. Testing was carried out with a plutonium/beryllium source and a industry-standard liquid scintillator detector to define a tagged fast-neutron beam (2.8–6.3 MeV). It was shown that the neutron response is energy dependent and improves at lower energies. Fast-neutron tracking capabilities of the detector were demonstrated.

Contents

1	Introduction	1
1.1	The Neutron	1
1.1.1	Basics	1
1.1.2	Spallation	2
1.1.3	Moderation	3
1.1.4	Beam Guides	3
1.1.5	Detection	4
1.1.6	Applications	5
1.2	Energetic Background at Spallation Sources	6
1.3	Project and Goals	8
2	Methods	11
2.1	Scintillators	11
2.1.1	Organic	12
2.1.2	Inorganic	13
2.2	Scintillation-Photon Attenuation	15
2.3	Signal Processing and Electronics	16
2.3.1	Photomultiplier Tubes	16
2.3.2	Discriminators	16
2.3.3	Charge-to-Digital Converter	17
2.3.4	Time-to-Digital Converter	18
2.4	Neutron Identification	18
2.4.1	Pulse-Shape Discrimination	18
2.4.2	Time-of-Flight	19
3	Materials	21
3.1	Detector Development	21
3.1.1	Cutting of Scintillator	21
3.1.2	Wrapping	24
3.1.3	Light-Leak Tests	25
3.1.4	PUG Configuration	26
3.2	Detector-Response Study	29
3.2.1	Cosmic-Ray Muons	29
3.2.2	Setup	29
3.2.3	Energy Resolution	31
3.2.4	Position Resolution	32
3.2.5	Light-Attenuation Length	34

4	Measurement at the Source Testing Facility	37
4.1	Experimental Setup	37
4.1.1	Neutron Tagging	37
4.1.2	Measurements	40
4.1.3	Definition of the Fast-Neutron Beam	41
4.2	Selected Results	43
4.2.1	Bar 1, Bar 2 Energy Deposition	43
4.2.2	Neutron-Tracking Study	46
5	Summary	49
5.1	Overview	49
5.2	Conclusions	49
5.3	Outlook	50
5.4	Suggestions for Improvement	50
	Appendices	53
A	Contributions of the Author	55
B	Poster at ICANS XXII, 2017	57
C	Technical Drawings and Bill of Materials	59

List of Figures

1.1.1 Overview of the spallation process.	2
1.1.2 Neutron reflection and the critical-angle dependence.	3
1.1.3 Neutron-proton scattering.	5
1.1.4 Complementary x-ray and neutron images.	6
1.2.1 Simulated spallation neutron-spectrum per incident proton for ESS.	6
1.2.2 The prompt-neutron problem.	7
1.2.3 Sources of fast-neutron background	8
1.3.1 Conceptual design of PUG.	9
2.1.1 Main decay scintillation-light components of a scintillator material.	12
2.1.2 Energy-level diagram of electronic π -levels	13
2.1.3 Electronic band structure of an inorganic scintillator.	14
2.2.1 Photon interaction cross sections for lead.	15
2.3.1 A scintillator and photomultiplier tube.	16
2.3.2 Illustration of timing “walk” for a discriminator.	17
2.3.3 Constant-fraction discrimination.	17
2.3.4 QDC functionality.	18
2.4.1 Principles of pulse-shape discrimination.	19
3.1.1 Scintillator Test-cut 1.	22
3.1.2 Scintillator Test-cut 2.	22
3.1.3 Scintillator Test-cut 3.	23
3.1.4 Scintillator Test-cut 4.	23
3.1.5 Photo of scintillator bars after cutting and polishing.	24
3.1.6 Images of the wrapping process of the scintillator bars.	25
3.1.7 Scintillator-bar configuration.	26
3.1.8 Design of detector frame.	27
3.1.9 Static load simulation of detector frame.	28
3.2.1 Stopping power of charged particles in NE102 plastic scintillator	29
3.2.2 Cosmic-ray muon experimental setup.	30
3.2.3 Muon-trigger electronics	30
3.2.4 Cosmic-ray muon signal and integration.	31
3.2.5 Energy resolution of NE110 for 20 MeV cosmic-ray muons.	32
3.2.6 Time difference between two cosmic-ray muon signals.	33
3.2.7 Relative pulse timing.	34
4.1.1 Photograph of a PUG bar	37
4.1.2 The fast-neutron tagging setup.	38
4.1.3 Real-time arrival of pulses for the TOF setup.	39
4.1.4 A typical TOF spectrum.	40

4.1.5 Experimental setup shown from the top.	40
4.1.6 Photograph of the experimental setup	41
4.1.7 <i>PS</i> vs TOF for the NE213 detector.	42
4.2.1 Experimental setup.	43
4.2.2 Deposited-energy spectra for tagged neutrons.	44
4.2.3 Flight-time spectra for tagged neutrons.	46
4.2.4 Extreme neutron trajectories.	47

List of Tables

1.1.1 Neutron-energy ranges.	4
1.1.2 Q-values for common thermal-neutron reactions.	4
1.1.3 Maximum energy transfer for neutron-nucleus scattering.	5
2.1.1 Material characteristics of NE110 and NE213.	13
2.1.2 Material characteristics of YAP(Ce) and NaI(Tl).	14
3.1.1 Results from light-leak tests.	25
3.2.1 Energy-resolution measurements.	32
3.2.2 Position-resolution measurements.	34
3.2.3 Attenuation-length measurement.	35
4.1.1 Neutron TOF cut limits for the NE213 detector.	42
4.2.1 Measured flight time.	48

List of Abbreviations

BOM	Bill of Materials
CFD	Constant Fraction Discriminator
CM	Center of Mass
DAQ	Data Acquisition
ESS	European Spallation Source
LG	Long Gate
LINAC	Linear Accelerator
MCA	Multi Channel Analyser
PID	Particle Identification
PMT	Photomultiplier Tube
PSD	Pulse-shape Discrimination
PUG	Portable Fast-neutron Diagnostic Detector
QDC	Charge to Digital Converter
SG	Short Gate
S/N	Signal-to-noise
SNS	Spallation Neutron Source
STF	Source Testing Facility
TDC	Time to Digital Converter
TOF	Time-of-flight
TPI	Teeth per Inch

Chapter 1

Introduction

Currently under construction, The European Spallation Source ERIC (ESS) will be the brightest spallation-neutron source in the world [1]. It will accelerate proton bunches using a linear accelerator (LINAC) towards a tungsten target. The repetition rate of the proton bunches is planned to be 14 Hz with a 2.86 ms pulse length, a never before undertaken configuration. Spallation within the target material will result in the production of free neutrons. After production, the neutrons will be moderated and guided along neutron beam guides towards instrument stations. ESS will house scientists from the fields of material research, biology, medicine and chemistry. The facility is planned to be in operation by 2023.

The project reported on in this thesis was carried out in association with the Neutron Optics and Shielding group of ESS¹. The focus of this thesis is the design, construction and testing of a fast-neutron detector prototype to be used for the characterization of high-energy background at spallation sources. The envisioned Portable Fast-Neutron Diagnostic Detector (PUG) will have two arrays of neutron-sensitive detectors which can move independently of each other to potentially allow for time-of-flight (TOF) measurements and tracking capabilities. Neutron tracking is not easily performed, making this undertaking a considerable challenge.

1.1 The Neutron

1.1.1 Basics

Discovered by Chadwick in 1932 [2], the neutron is a neutral subatomic particle that together with the proton makes up the nucleus of the atom. The neutron has almost the same mass as the proton and belongs to the baryon family of subatomic particles. This means that the neutron is composed of quarks – specifically, one “up” quark and two “down” quarks (udd). As each of the quarks have their own charge (up: $+\frac{2}{3}e$, down: $-\frac{1}{3}e$), this produces a non-symmetric internal charge distribution giving the neutron an overall magnetic moment [3]. Thus, even though the charge-neutral neutron does not interact with electric fields, it does interact weakly with magnetic fields.

While a bound neutron is stable, a free neutron is not. The neutron has a mean

¹Support was also provided by the Detector Group.

lifetime of about 15 minutes. It then undergoes a beta decay according to:

$$n^0 \rightarrow p^+ + e^- + \bar{\nu}_e, \quad (1.1.1)$$

where the decay products are a proton (p^+), electron (e^-) and an electron-associated antineutrino ($\bar{\nu}_e$). As previously mentioned, by virtue of being a neutral particle, the neutron does not interact electromagnetically with atomic electrons and thus can penetrate deeply into very dense materials. At meV energies, neutrons have wavelengths on the order of the inter-atomic distance (10^{-10} m), which allows for the investigation of atomic phenomenon. Thus, free neutrons are excellent probes of matter.

1.1.2 Spallation

Free neutrons can be produced via induced fission or from actinide/beryllium sources, for example. PUG is envisioned to track spallation neutrons. Spallation may occur when an energetic beam of protons hits a stationary target consisting of a neutron-rich material like tungsten. Neutrons are freed as the high-energy protons strike the target and break apart its atoms. The freed neutrons likely have a very high energy which can vary up to the energy of the incident proton beam. Figure 1.1.1 shows a schematic overview of the spallation process. This process occurs in three main stages [4]: *cascade*, *transition* and *evaporation*. As the energetic proton strikes the target, it transfers energy to the individual nucleons and might result in the release of high-energy particles capable of further spallation. This is known as the cascade stage. In the subsequent transition stage, the energy transferred to the individual nucleons spreads throughout the nucleus. As a result, several nucleons might be ejected. During the transition stage, the nucleus ends up in a highly excited state and subsequently releases its energy in the evaporation stage. Several free neutrons, protons and other forms of radiation may be emitted. The evaporation stage results in the largest amount of free neutrons. For even heavier targets like depleted uranium and lead, high energy fission can compete with the evaporation stage during nuclear de-excitation [5].

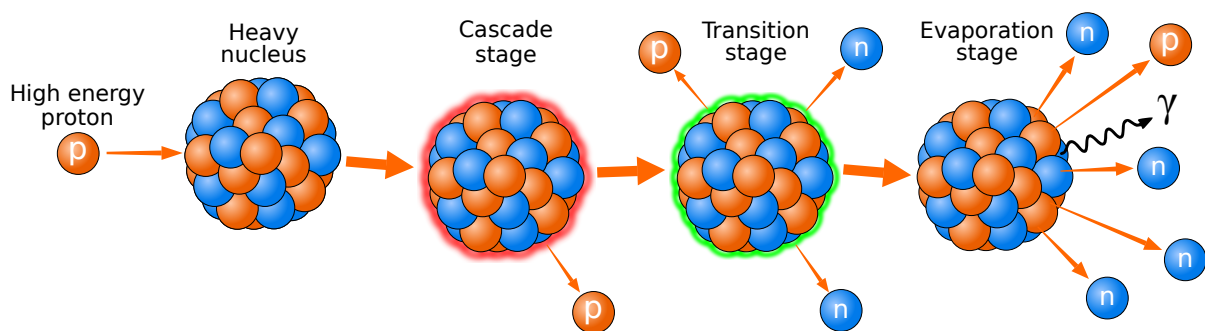


Figure 1.1.1: Overview of the spallation process. A high-energy incident proton (red) strikes a heavy nucleus which then passes through three stages: The Cascade stage (red outline), the transition stage (green outline) and the Evaporation stage (rightmost image). Neutrons (blue) and other forms of radiation such as protons and γ -rays (black) may be emitted. The evaporation stage results in the largest number of free neutrons.

One advantage of a spallation neutron source is that large numbers of neutrons can be freed for each spallation event. Furthermore, the proton beam is likely pulsed. This

results in pulses of spallation neutrons, which can be advantageous for measurements as “quiet time” exists between each beam pulse (see Sec. 2.4.2). Generally, neutrons used for material research need to be of a much lower energy than they are after the spallation process. This requires sophisticated methods of *moderating* (Sec. 1.1.3) and guiding them (Sec. 1.1.4).

1.1.3 Moderation

Moderation is a process where an energetic neutron interacts through scattering with a material and loses a large portion (but not all) of its energy. Moderator materials are often hydrogen rich or consist of some other light nuclei. As shown in Table 1.1.3, a neutron is kinematically able to transfer a larger portion of its energy to a lighter nucleus via scattering which means that the moderation process will be more efficient for light moderators. A neutron will in general continue this scattering process through the moderating material until it reaches thermal equilibrium with its surroundings. At this point, it will likely be absorbed by a moderator nucleus. Since the point of the moderation process is only to decrease the energy of the neutron, the size and composition of the moderator need to be carefully considered to ensure that the maximum number of neutrons with the desired energy survive the moderation process.

1.1.4 Beam Guides

The main purpose of neutron beam guides is to transport neutrons between the spallation source and the instrument station and focus them at the sample. Beams of charged particles can be focused and guided using external magnetic fields. This will not work for neutral particles. Instead, it is possible to use the wavelike characteristics of neutrons to “guide” them along a predetermined path, essentially creating a neutron “mirror”. For a neutron to be reflected at the surface of the waveguide material, it must have an incident angle that is smaller than the critical angle θ_C (see Fig. 1.1.2).

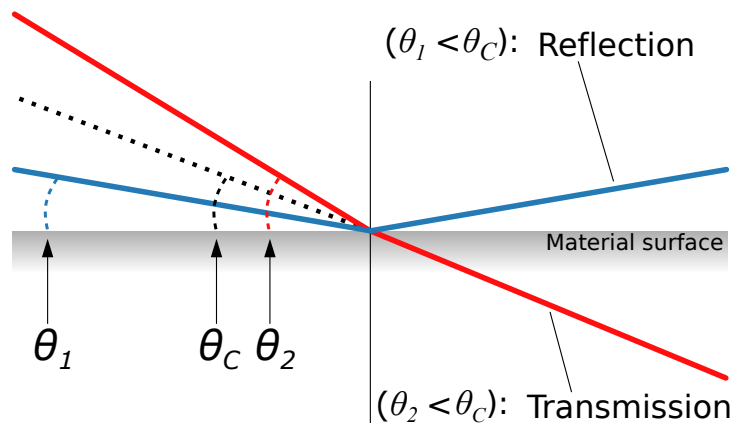


Figure 1.1.2: Neutron reflection and the critical-angle dependence. Two different angles of incidence θ_1 (blue) and θ_2 (red) are shown along with the critical angle θ_C . θ_2 results in transmission and θ_1 in reflection. The grey shaded area represents the surface of the material.

The critical angle must be considered when designing a neutron beam guide. It is a material characteristic dependent on the index of refraction and atomic mass of the coating

material as well as the energy of the neutrons. More advanced configurations also exist, where several layers of different materials are used to enable the reflection of neutrons of varying energies. These reflectors are known as *super mirrors* [6].

1.1.5 Detection

Since a neutron does not have charge, the neutron itself does not leave a direct signal in a detector. It can however be detected indirectly, through events like capture, scattering or fission. The efficiency of detection is often related to the energy of the neutron and the atomic number of the detector material. Neutron energies are often divided into the following energy ranges:

Type	Energy
<i>Cold</i> neutrons	~ 2.2 meV
<i>Thermal</i> neutrons	~ 25 meV
<i>Epithermal</i> neutrons	~ 1 eV
<i>Fast</i> neutrons	> 0.5 MeV

Table 1.1.1: Neutron-energy ranges. Thermal neutrons are in thermal equilibrium with their surroundings.

Consider neutrons in the fast-neutron range and thermal-neutron range as representative. At thermal energies, neutrons may be detected via the by-products of nuclear reactions. The longer the time spent by a neutron close to a nucleus due to its lower velocity, the higher the probability that it is affected by the strong force. This can lead to a nuclear reaction. Some useful thermal-neutron reactions are given in Table 1.1.2.

Element	Reaction	Q
${}^3\text{He}$	$n + {}^3\text{He} \rightarrow {}^3\text{H} + \text{p}$	0.76 MeV
${}^{10}\text{B}$	$n + {}^{10}\text{B} \rightarrow {}^7\text{Li} + \alpha$	2.31 MeV
${}^6\text{Li}$	$n + {}^6\text{Li} \rightarrow {}^3\text{H} + \alpha$	4.78 MeV

Table 1.1.2: Q -values for common thermal-neutron reactions. The reactions shown are the most probable for the specific element. The Q -value is the energy released in the process, which takes the form of kinetic energy shared by the products.

Various neutron-sensitive elements can be used to optimize a detector for a specific neutron energy. Furthermore, this knowledge can also be used to design more efficient neutron shielding [7, 8]. In fact, detecting neutrons and shielding neutrons are conceptually very similar.

In the case of fast neutrons, the main interaction method is scattering. It is then the ionizing recoil particle energy (E_R) that is measured. This process produces a broad energy spectrum since the scattered neutrons can transfer all or none (or anything in between) of their energy to the recoil. Figure 1.1.3 shows a neutron with incident energy E_n scattering off a proton, causing the proton to recoil with energy E_R and continuing with a reduced energy E'_n . In general, the recoiling energy for any nucleus is given by [9]:

$$E_R = \frac{4A}{(1+A)^2} (\cos^2 \theta) E_n, \quad (1.1.2)$$

where θ is the neutron-scattering angle and A is the mass of the target nucleus. The maximum energy transfer thus occurs at $\theta = 0^\circ$, meaning that the incident neutron will stop and the recoiling nucleus will travel in the original direction of the neutron. Table 1.1.3 shows a number of light elements and the maximum energy transfer possible.

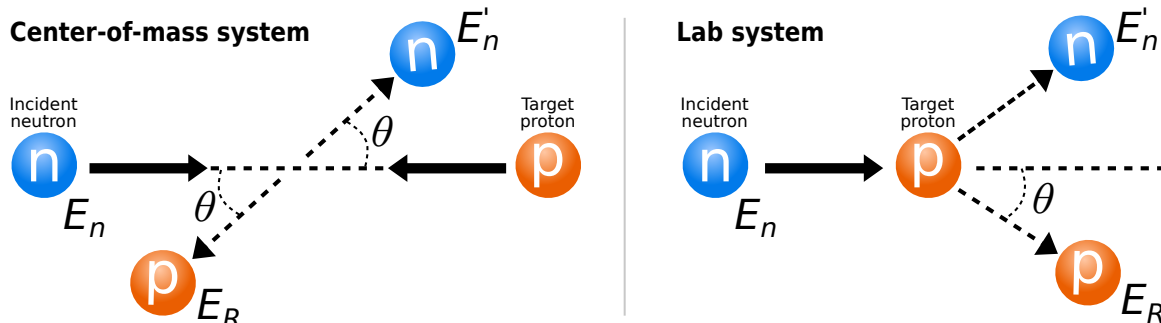


Figure 1.1.3: Neutron-proton scattering. Center-of-mass (left) and Lab system (right). Left panel: an incident neutron (blue) with energy E_n scatters off a proton (red) at an angle θ . The neutron transfers energy to the proton, giving it a recoil energy E_R . The neutron then continues with a reduced energy E'_n . Right panel: as above, but for the Lab system.

Target Nucleus	A	$(E_R/E_n)_{\max}$
^1H	1	1.000
^2H	2	0.889
^3He	3	0.750
^4He	4	0.640
^{12}C	12	0.284
^{16}O	16	0.221

Table 1.1.3: Maximum energy transfer for neutron-nucleus scattering. For heavier nuclei, the maximum possible energy transfer is even less than for ^{16}O [9].

Note that neutron scattering may also leave the target nucleus in an excited state where the subsequent de-excitation products can then be detected. For extremely high energies (>100 MeV), hadronic showers can form where the interaction between the neutron and nucleus results in a multitude of particles. This is a very important process for neutron detection in high-energy physics [10].

1.1.6 Applications

Neutron scattering is widely used to probe materials. Three-dimensional images of the samples under study may result. As neutrons generally only see the atomic nucleus, neutron scattering also allows for the differentiation of isotopes in the sample. Another technique known as magnetic neutron scattering utilizes the interaction between the magnetic moment of the neutron and the internal magnetic fields of materials to determine information about magnetic structure and electron spin. Figure 1.1.4 shows complementary X-ray and neutron images of an old 35 mm film camera. A darker shade indicates reduced radiation penetration. In the left panel, the x-rays can barely penetrate the metal casing of the cameras, but any less dense material like the plastic components is almost

invisible to the radiation. In contrast, the right panel shows that the neutron beam is able to resolve details hidden by the metal casing but is instead stopped by the hydrogen-rich plastic components. Together, these images clearly illustrate the complementary nature of the two very different probes.

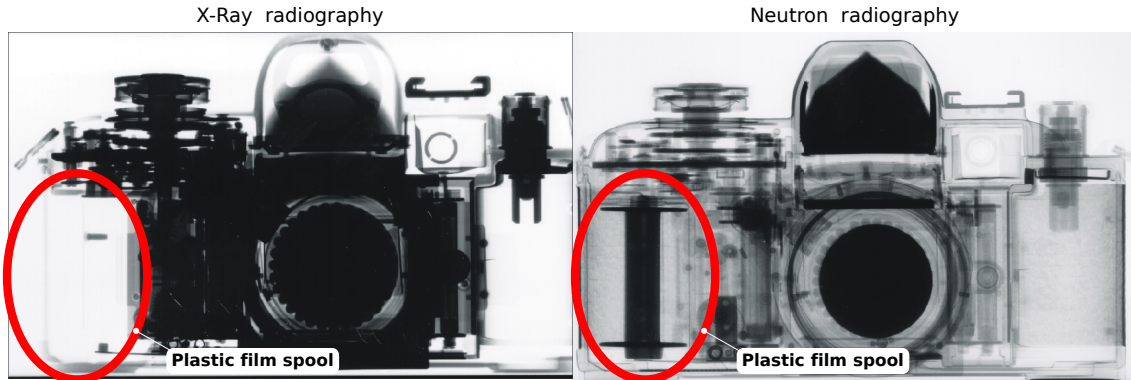


Figure 1.1.4: X-ray (left) and neutron images (right). Figure adapted from [11].

1.2 Energetic Background at Spallation Sources

Ideally, all neutrons reaching instrument stations at a spallation-neutron source will have an energy on the order of meV. However, in reality, even after moderation and significant shielding, the incident spectrum of neutrons will extend from the desired energy up to a significant portion of the incident energy of the proton beam, an example of which is shown in Fig. 1.2.1.

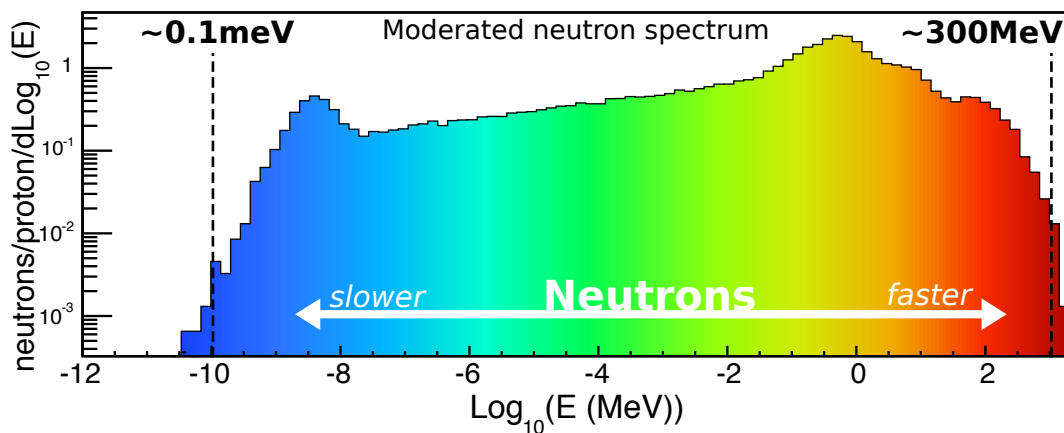


Figure 1.2.1: Simulated spallation neutron-spectrum per incident proton for ESS. This is the moderated spectrum where all neutrons ranging from slower (blue) to faster (red) are shown. Figure adapted from [12].

Prompt neutrons are the most energetic component of the neutron spectrum. Prompt neutrons are undesirable and there are several methods used to deal with them. For example, neutron choppers which mechanically block the neutron beam at specific times relative to the spallation event may be employed. Further, the neutron-beam guide may be “bent” which will result in lower-energy neutrons following the guide while higher energy neutrons continue in a straight trajectory and escape. Unfortunately, prompt neu-

trons cannot be completely eliminated.

Figure 1.2.2 illustrates the prompt-neutron problem – essentially “cross-talk” between two beam pulses as a function of time. The fastest prompt neutrons are the first to reach the detector with the remainder of the energy spectrum arriving subsequently. In the “Current pulse” frame, instruments which are designed to use the lowest-energy neutrons from the “Previous pulse” will have that part of the spectrum obscured by the current prompt-neutron component, as shown in the “Region of overlap”.

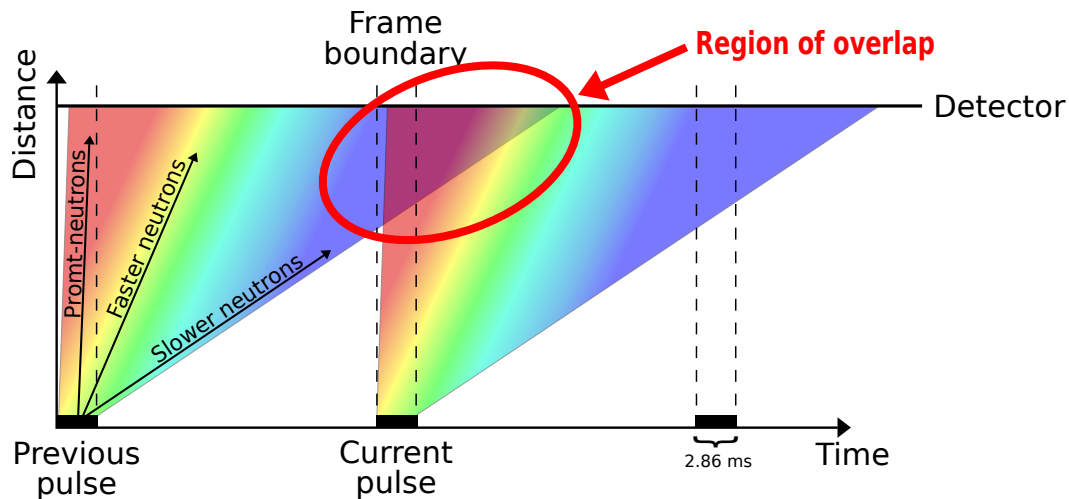


Figure 1.2.2: The prompt-neutron problem. The dashed lines are the start and stop of the proton pulses and the neutron spectrum is color-coded from red (fastest) to blue (slowest). The “Region of overlap” (red ellipse) at the detector position is the concern. Figure adapted from [13].

Studies made at the Spallation Neutron Source (SNS, Oak Ridge National Laboratory, USA) [14] have shown that these prompt neutrons can contribute a significant background signal at the sample position of a neutron-scattering instrument. Systematic studies done at SNS on the HYSPEC instrument put the prompt-neutron pulse contributions from sources other than neighboring instruments and neutron-beam guides at about 40% [15]. This is a significant contribution.

Figure 1.2.3 shows a schematic view of a spallation source together with sources of proton-beam pulse-correlated high-energy neutrons. These are:

- (a) a proton interacts with the LINAC resulting in pre-target spallation. These pre-target spallation neutrons could possibly reach the instrument station via *neutron skyshine*, a process which has been observed at other proton-accelerator facilities [16];
- (b) a neutron travelling directly from the target to the instrument station (b_1). This might also occur through scattering (b_2). Another contribution is directly through the neutron beam guide (not shown);
- (c) a neutron escaping the neutron-beam guide;
- (d) a neutron scattering at the instrument station and interacting with one or more of the detectors.

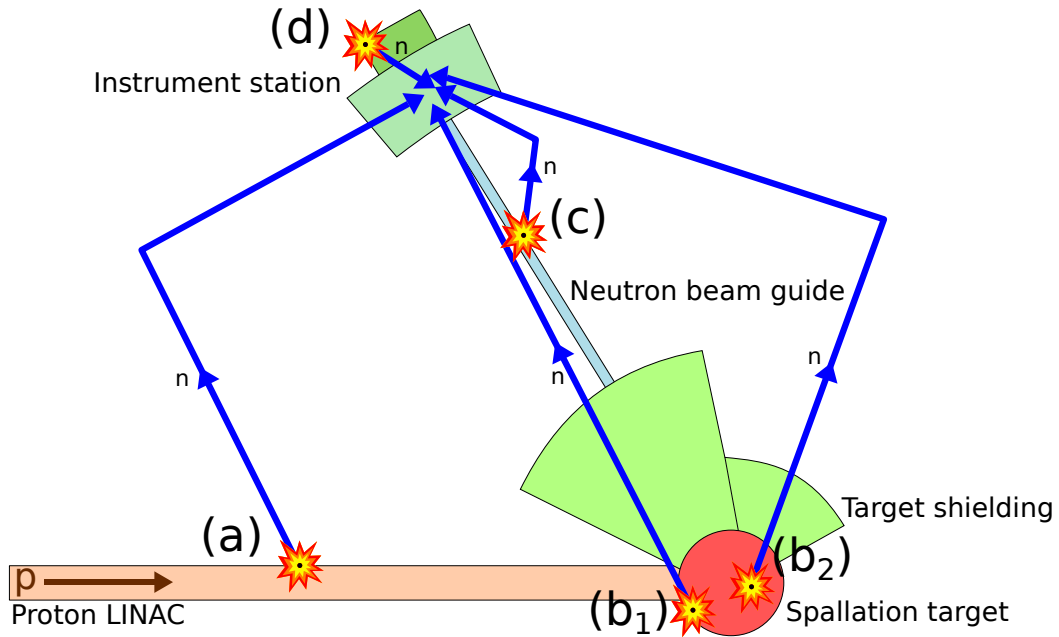


Figure 1.2.3: Sources of fast-neutron background. The proton LINAC is shown in orange, the target shielding, instrument shielding and instrument station in green and the spallation target in red. The neutron-beam guide is shown in light-blue. The dark-blue trajectories are unwanted neutron backgrounds.

1.3 Project and Goals

Clearly, a tool for identifying sources of fast-neutron background could be very valuable. This crucial gap in diagnostic technologies may be filled by the PUG, which is proposed to consist of two arrays of plastic scintillator bars mounted on two independent frames. This may allow for self-triggering time-of-flight (TOF) measurements (see Sec. 2.4.2) and ultimately for tracking of fast neutrons. The two detector arrays are foreseen to be used in various configurations; for example, as a TOF wall using the proton-beam pulse as the start signal or in a stacked configuration resulting in a higher detection efficiency. Furthermore, even though the detector was developed for fast-neutron detection, it will also allow for excellent charged-particle detection and tracking. Figure 1.3.1 shows the conceptual design of the two detector arrays of PUG.

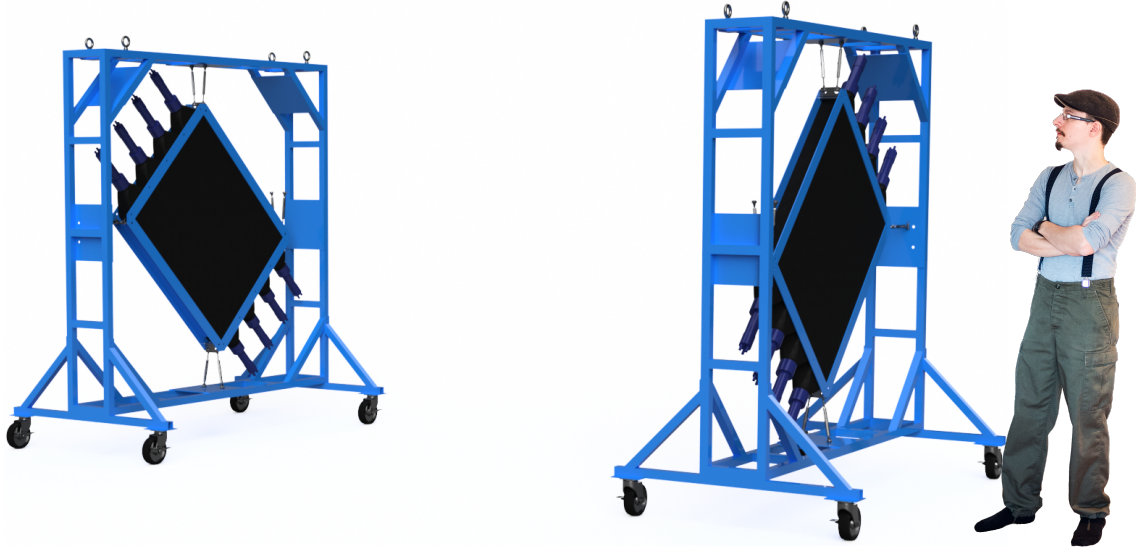


Figure 1.3.1: Conceptual design of PUG. The two detector arrays are shown in black and the mounting frame in blue. Each detector array measures $190 \times 190 \times 30 \text{ cm}^3$ (not including the frame legs and casters) with a total mass of 240 kg each.

The ultimate goal of this project is the development of a fast-neutron detector which can be used to investigate and diagnose high-energy background, mainly from pulse-correlated prompt fast-neutrons, at spallation facilities. The investigation reported on here has been carried out at the Source Testing Facility (STF) at Lund University, Sweden.

The remainder of the thesis is organised in the following manner. In Chapter 2, the principles and mechanisms behind scintillation processes are discussed and an overview of two different types of neutron-identification methods is presented. In Chapter 3, the fabrication of the scintillator detectors, including cutting of the scintillator material and light-leak testing are presented. A detailed discussion of the full-sized detector configuration and suspension frame is also presented. Furthermore, testing of the scintillator material using cosmic-ray muons is presented and includes a study of the materials resolution, position resolution and light attenuation. In Chapter 4, fast-neutron measurements performed at the Source Testing Facility are discussed in detail. An in-depth presentation of the method employed to define the fast-neutron beam used for the PUG irradiations is made, and selected experimental results pertinent to fast-neutron tracking are discussed in detail. In Chapter 5, a project summary is presented, including overview, conclusions, future outlook and suggestions for improvement.

Chapter 2

Methods

2.1 Scintillators

Particle detectors are commonly made from a scintillator material. As photons or particles interact with the material, they may transfer part, or all, of their energy and a flash of light known as a *scintillation* is created. The total amount of scintillation light created is often directly proportional to the energy deposited by the incident particle. For charged particles, this is the product of the energy-loss gradient (dE/dx) and the range of the charged particle, while for particles like the neutron this corresponds to the product of the energy-loss gradient and the range of the recoiling post-scatter charged particles (Sec. 1.1.5). The light from the scintillation events may be collected and converted into analog electrical signals by photomultiplier tubes (PMTs) (Sec. 2.3.1) which are optically attached to the scintillator material.

Scintillation detectors are generally considered to be fast. The rise time and the fall time of the scintillation pulse is relatively short. Thus, a scintillator-based detector is able to “reset” quickly after an event, which allows for events which occur close in time to be separated. This increases the maximum sustainable count rate of the detector since the *dead time*, the time it takes for the scintillation-light pulse to decay, is small.

The decay of the light output during a scintillation event can be decomposed into *prompt* and *delayed* components:

$$N(t) = \underbrace{Ae^{-t/\tau_p}}_{\text{prompt}} + \underbrace{Be^{-t/\tau_d}}_{\text{delayed}}, \quad (2.1.1)$$

where $N(t)$ is the number of scintillation photons emitted at time t , A is the amplitude of the prompt pulse, τ_p is the decay constant of the prompt pulse, B is the amplitude of the delayed pulse and τ_d is the decay constant of the delayed pulse. Prompt light generally has the highest amplitude and also decays quickly while delayed light generally has a lower amplitude and decays slowly. Figure 2.1.1 shows an example of prompt and delayed scintillation-light components along with the corresponding total light output.

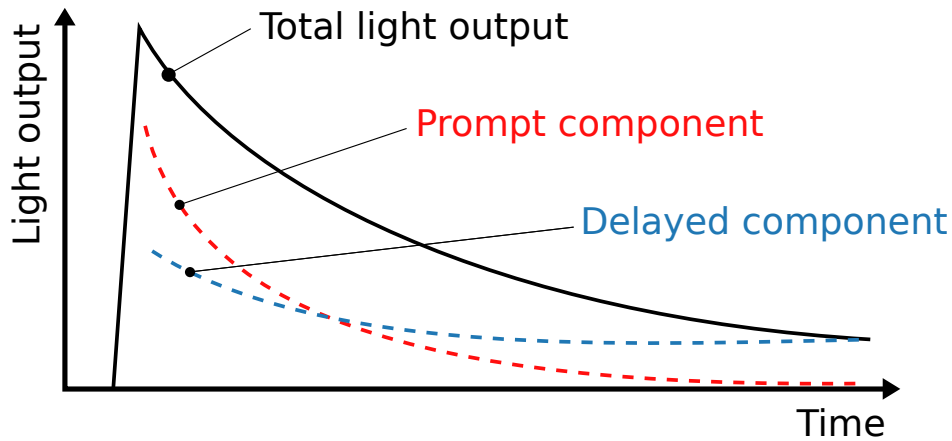


Figure 2.1.1: Main decay scintillation-light components of a scintillator material. The prompt component (dashed red line) and delayed component (dashed blue line) sum to the total light output (solid black line). Figure from [17].

Note that wide variations in the behaviour of different types of scintillation materials are possible.

2.1.1 Organic

Organic scintillators consist of hydrocarbons in benzene-ring structures. Scintillation arises when ionizing radiation interacts with molecular valence electrons which then undergo an energy transition. The valence electrons are bound in what is known as π -orbitals which are common to the entire molecule. These excitations will likely leave the electron in either a singlet (S , $s = 0$) or triplet (T , $s = 1$) state, which are different sets of energy levels indicated by the spin quantum number (s) of the system. Figure 2.1.2 shows a schematic overview of these states and the π -orbital energy levels. S_0 is the singlet ground state and S^* and S^{**} are low-energy excited states. The triplet states are similarly represented. The thinner lines above each energy level represent the vibrational states of the molecule. As the ionizing radiation interacts with the molecule all states can be excited. The excited S^{**} states decay to the S^* state through a process called *internal degradation*, and scintillation light is not emitted. It is the subsequent decay from S^* to S_0 that gives rise to prompt scintillation photons. Electrons which end up in the triplet states decay through a similar internal degradation process to T_0 . Decay from T_0 to S_0 is forbidden by selection rules. However, the T_0 state might be thermally excited to the S^* state through intermolecular interactions, and then decay normally to S_0 [9]. This process takes longer and gives rise to delayed scintillation photons. An important aspect of a scintillator is that it is transparent to its own emission light. This is achieved here since electrons in the S^* states can transition to the vibrational states of S_0 .

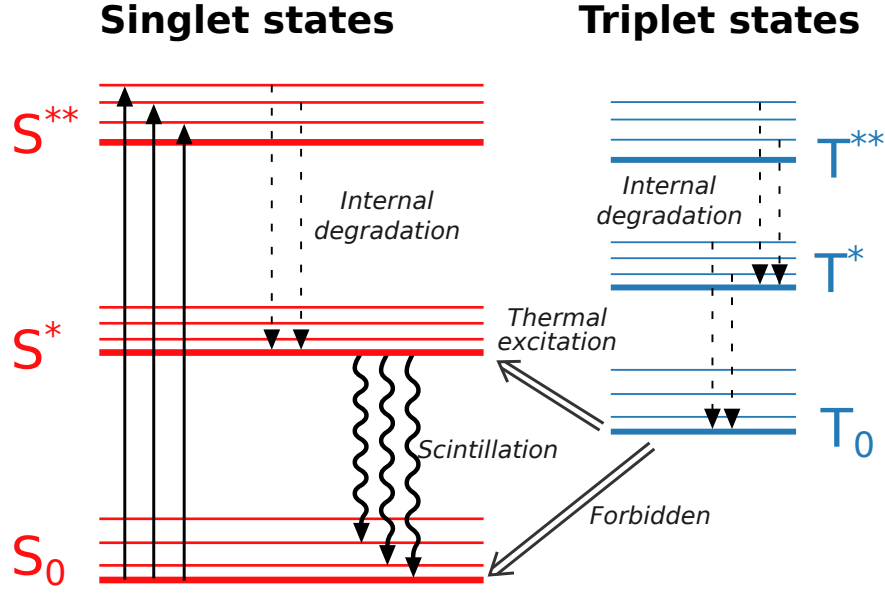


Figure 2.1.2: Energy-level diagram of electronic π -levels. Singlet (red) and triplet (blue) states are shown. The thick lines represent energy levels and the thin lines represent vibrational levels. Figure from [17].

A characteristic feature of an organic scintillator is the short (order of 10s of ns) decay time of the scintillation light pulse¹, which makes them particularly effective when a high count rate is anticipated so that a low dead time may be achieved.

In the case of solid organic (plastic) scintillators, one of their main advantages is their flexibility. They are relatively inexpensive and can be machined and formed to almost any dimension. They are also considered extremely fast (even for an organic scintillator) with decay constants of 2–3 ns, dependent on the type of plastic. Organic scintillators are also available in liquid form where one or more scintillating materials are mixed. The benefit of this is the ability to create custom scintillator materials quite easily or to modify a commercial material for a specific application. Table 2.1.1 shows the characteristics of the two organic scintillator materials used in this thesis.

Scintillator	Type	Density ρ [g/cm ³]	Index of refraction n	Wavelength λ^{\max} [nm]	decay constant τ [ns]
NE110	Plastic	1.032	1.580	434	3.3
NE213	Liquid	0.873	1.508	425	3.7

Table 2.1.1: Material characteristics of NE110 and NE213. Data from [18].

2.1.2 Inorganic

Most inorganic scintillators consist of a crystalline structure doped with a small amount of impurities known as *activators*. Inorganic scintillators are usually much slower than organic scintillators, with decay constants 2–3 orders of magnitude longer. This longer decay comes from the delayed term in Eq. (2.1.1). Figure 2.1.3 below shows a schematic

¹The total light output (Fig. 2.1.1), which is the sum of the prompt and delayed components.

of the excitation and scintillation process of an inorganic crystal scintillator. The incoming ionizing radiation excites an electron from the valence band to the conduction band where it is energetically free to move throughout the crystal lattice. The added activator results in energy states within the band gap that facilitate a direct transition to a lower energy. This is the main mechanism for scintillation-light production. This also makes the scintillator transparent to its own scintillation light.

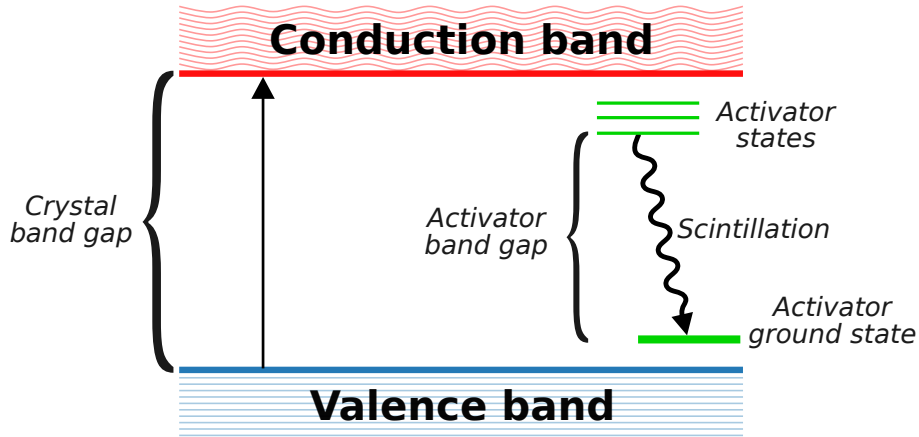


Figure 2.1.3: Electronic band structure of an inorganic scintillator. The valence (blue) and conduction (red) bands are shown. An electron excited to the conduction band can, via the near-lying activator states (green), reach the activator ground state and emit scintillation light.

A major drawback of inorganic scintillators is the fact that they need to be grown, which is a slow and expensive process. This also limits the maximum size of most detectors to 10s of centimeters. Furthermore, most common inorganic scintillators are hydroscopic in nature, which means they attract moisture from air at room temperature. Moisture in inorganic crystals harms their structure so they must be carefully sealed after manufacturing which makes any subsequent modifications challenging. That said, given the higher atomic number and density of the crystalline material, inorganic scintillators generally have a higher stopping power, making them more efficient. The energy resolution measured with an inorganic scintillator is often superior to that measured using an organic scintillator as their scintillation-light output is much larger. This makes inorganic scintillators very well suited for high-energy γ -ray and electron detection.

For the work done in this thesis, a cerium-activated yttrium aluminium perovskite (YAP(Ce)) inorganic crystal was used. Table 2.1.2 shows the characteristics of YAP(Ce) along with another (common) inorganic scintillator, thallium-activated sodium iodide (NaI(Tl)).

Scintillator	Type	Density ρ [g/cm ³]	Index of refraction n	Wavelength λ^{\max} [nm]	decay constant τ [ns]
YAP(Ce)	Crystal	5.37	1.950	370	25
NaI(Tl)	Crystal	3.67	1.775	413	230

Table 2.1.2: Material characteristics of YAP(Ce) and NaI(Tl). Data from [19].

2.2 Scintillation-Photon Attenuation

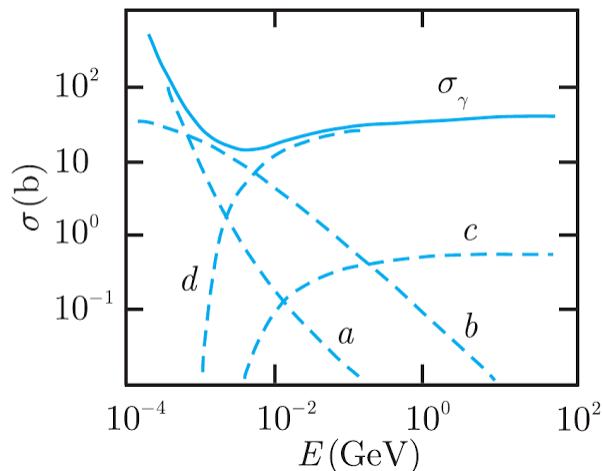


Figure 2.2.1: Photon interaction cross sections for lead. a) Photoelectric effect, b) Compton scattering, c) Pair production in the field of the atomic electrons, d) Pair production in the field of the atomic nucleus. The solid line is the total photon cross section σ_γ . Figure from [10].

Photon-matter interactions occur via three mechanisms:

- 1) Photoelectric effect (line *a* in Fig. 2.2.1): The photon is absorbed by a bound electron which is then ejected from the atom carrying with it the entire photon energy less the electron binding-energy.
- 2) Compton scattering (line *b* in Fig. 2.2.1): The photon transfers a certain amount of its energy to an electron, freeing it from the atom. The energy and direction of the photon changes after the scattering. This results in a wide range of energies for the emitted electron. Compton scattering requires the photon energy to be relatively high in comparison to the binding energy of the electron.
- 3) Pair production (lines *c* and *d* in Fig. 2.2.1): The photon interacts with the atomic electrons or nucleus resulting in an electron and positron pair. For this transformation to occur, the photon energy needs to be at least twice the rest energy of an electron, 1.022 MeV. Excess photon energy is shared equally by the pair as kinetic energy.

A beam of photons travelling through a material interacting in any of these ways will lose intensity. This process is known as *attenuation*. This effect is important for scintillator materials, where the scintillation light is attenuated as it transverses the material. The light attenuation is given by:

$$I(x) = I_0 e^{-\alpha(E_\gamma)x}, \quad (2.2.1)$$

where I_0 is the original scintillation-light intensity, x is the distance the scintillation light travels in the material, $\alpha(E_\gamma)$ is the attenuation coefficient of the material and E_γ is the energy of the scintillation light. The attenuation coefficient is an energy-dependent property of a material, but in the case of scintillators which normally emit light in a narrow energy range, it can be taken to be constant.

2.3 Signal Processing and Electronics

2.3.1 Photomultiplier Tubes

To detect the light from a scintillation event, photomultiplier tubes (PMTs) are often used. PMTs are extremely light-sensitive detectors. Figure 2.3.1 shows a schematic overview of a scintillator and PMT setup. The photocathode is coated with a photosensitive material, which absorbs an incident scintillation photon and emits a single photoelectron through the photoelectric effect. Inside the (evacuated) tube, the photoelectron is directed to the first *dynode* via an electric field. Here, secondary electrons are released. The electrons are accelerated across several electron-multiplier dynodes. This process produces an increasingly large pulse of electrons at each dynode in an avalanche-like process until a measurable current pulse reaches the anode. At this point, the originally absorbed scintillation photon has been converted into a detectable electric signal.

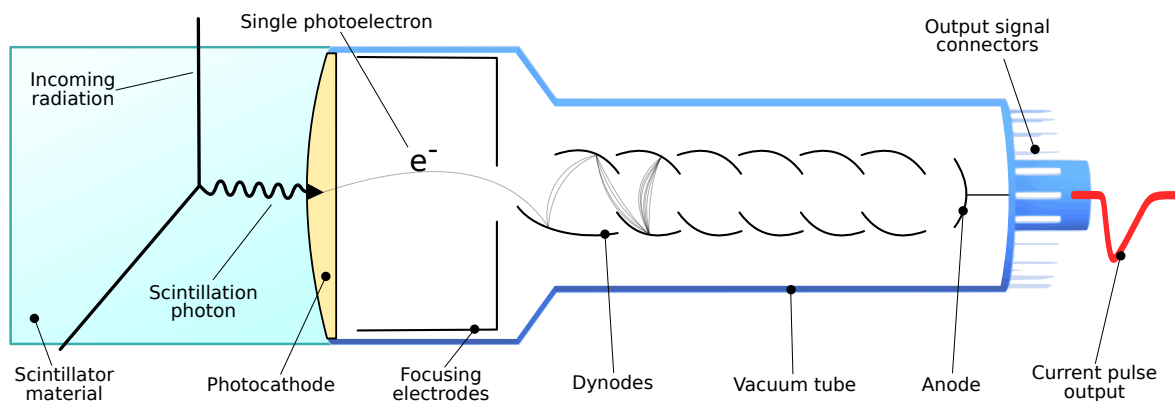


Figure 2.3.1: A scintillator and photomultiplier tube. Incident radiation creates a scintillation photon in the scintillator material (blue). The scintillation photon is absorbed in the photocathode (yellow) and a single photoelectron is freed. This photoelectron is multiplied across the dynodes into a detectable current pulse at the anode (red).

The current pulse delivered to the anode of the PMT is often proportional to the energy deposited in the scintillator by the incident radiation. Note that this is generally not the case for neutrons, as discussed in Sec. 1.1.5.

2.3.2 Discriminators

A discriminator is used to set a *threshold* which determines the minimum amplitude a signal must have in order to result in a logical “true” condition. The length of the logic pulse is usually variable. Logic signals are used to build event *triggers*. For the work performed here, discriminators were extensively used, specifically *constant-fraction discriminators* (CFDs). The difference between a leading-edge discriminator and CFD is that a CFD not only discriminates the signal amplitude but it also eliminates the “walk” that occurs between two signals of different amplitude. Consider Fig. 2.3.2 where two coincident signals with different amplitudes both cross the threshold but at slightly different times since the rise time of the pulses is amplitude dependent. Since the trigger occurs when the signal crosses the threshold, “walk” (an unwanted delay) results. The CFD used here solves this problem by splitting the incoming signal into two pulses (see

Fig. 2.3.3). One is inverted, the other is delayed and finally both are summed. The CFD triggers on the zero-crossing point of the summed signal which produces a “walk-free” timing spectrum.

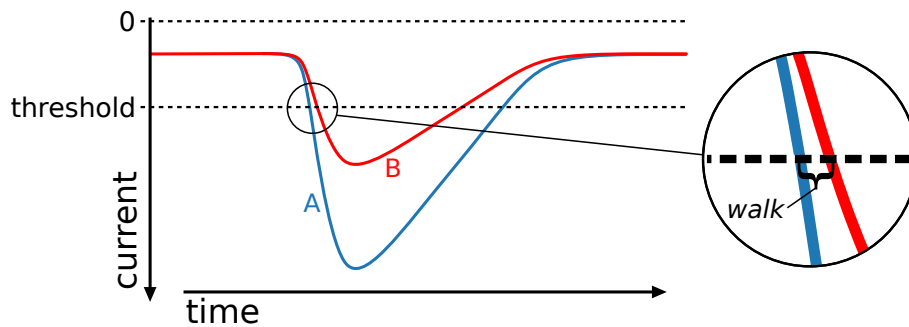


Figure 2.3.2: Illustration of timing “walk” for a discriminator. Two coincident current pulses, red and blue, exceeding the discriminator threshold are shown. Both signals will result in logic true but with a slight time difference known as “walk”. Figure from [20].

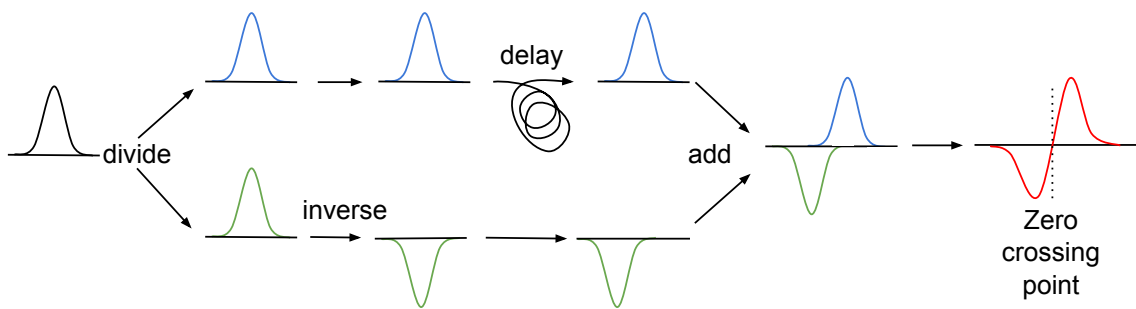


Figure 2.3.3: Constant-fraction discrimination. The original pulse (black) gets split (blue and green). The green signal is inverted and the blue signal delayed before they are both summed together. The trigger is now defined by the zero-crossing point. Figure from [20].

2.3.3 Charge-to-Digital Converter

The charge Q collected at the anode of the PMT can be obtained by integrating the current pulse over time. Using a charge-to-digital converter (QDC) is one method for this. QDCs are electronic units which integrate an analog signal with respect to a logical gate signal which sets the start (T_{start}) and stop (T_{stop}) times for the integration, respectively.

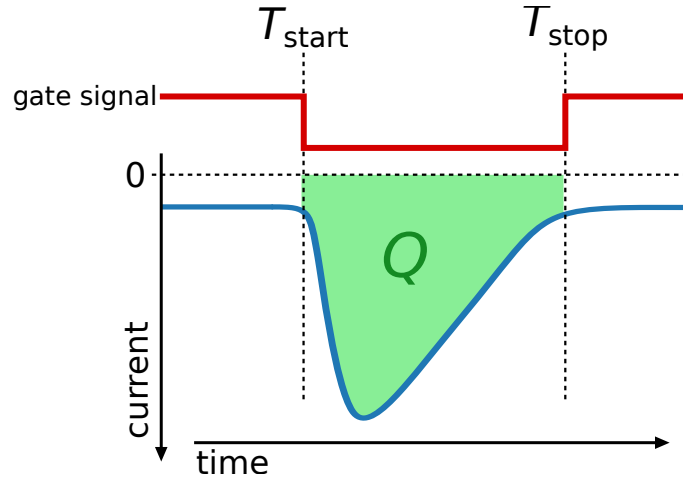


Figure 2.3.4: QDC functionality. The current pulse (blue) is integrated over time $\Delta t = T_{\text{stop}} - T_{\text{start}}$ which is set by a gate signal (red) to obtain the total charge Q (green).

This charge can then, for example, be passed to a multichannel analyser which sorts each QDC value and produces a histogram of event-related charges.

2.3.4 Time-to-Digital Converter

A time-to-digital converter (TDC) is a device often used to measure event timing relative to a common start. This relative timing can be used to identify interesting events. For example, in detector systems with multiple channels, TDC information from each of the channels can provide knowledge on the correlation between channels for a single event or between events for a single channel. Event-based TDC information has been extensively used for the work performed in this thesis. More information on using TDCs can be found in Sec. 4.1.1.

2.4 Neutron Identification

2.4.1 Pulse-Shape Discrimination

For certain scintillators, the difference between the prompt and delayed scintillation-light yield depends strongly on the incident particle. For example, an electron will produce one shape of pulse while a proton will produce a differently shaped pulse. This feature facilitates a technique known as *pulse-shape discrimination* (PSD) for particle identification (PID). The underlying mechanism originates from the fact that the prompt and delayed components of the scintillation-light yield come from different excited states of the scintillator. Different incident particles will excite the prompt and delayed states in different ratios, producing different shapes of the scintillation-light pulse. Figure 2.4.1 shows an example of γ -ray (ionizing electron) and neutron (ionizing proton) pulse shapes produced by a NE213 liquid scintillator. As can be seen, the recoiling-proton (neutron-associated) interaction produces substantially more delayed scintillation light.

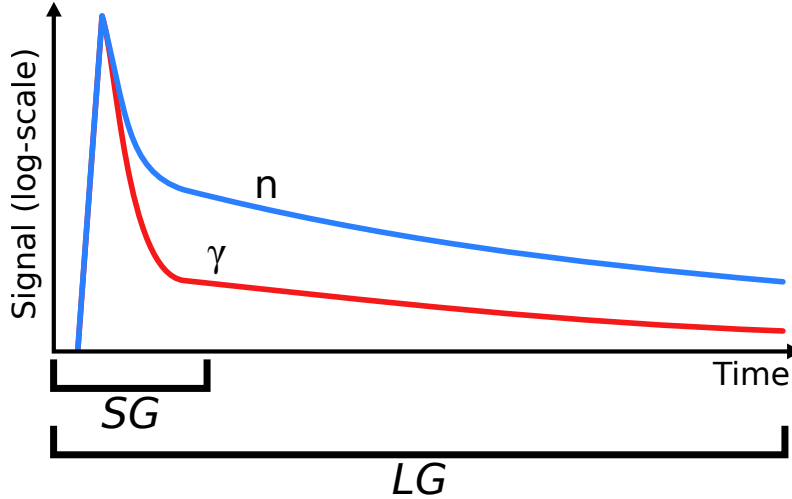


Figure 2.4.1: Principles of pulse-shape discrimination. Pulse-shape difference between γ -rays and neutrons for a NE213 liquid scintillator. The neutron (blue) and γ -ray (red) signals arise from recoiling protons and electrons, respectively. Short-gate (SG) and long-gate (LG) integration windows which facilitate PSD are also shown.

To attain a measurable difference between two pulse shapes, a diagnostic *pulse-shape* (PS) may be derived:

$$PS = \frac{LG - SG}{LG}, \quad (2.4.1)$$

where LG is a long-gate integration window and SG is a short-gate integration window. By integrating the pulses over two substantially different times, a meaningful difference may be determined. For this specific case, it means that larger PS values generally correspond to neutrons. PSD has been extensively employed in this thesis.

2.4.2 Time-of-Flight

The determination of the energy of a charged particle is straightforward. Assuming there is enough material for the particle to stop, the resultant signal should be proportional to the deposited energy. However, for neutral particles like the neutron, this is quite different. The secondary events produced by a neutron will almost always only carry a portion of the energy of the neutron which means that it is almost impossible to determine the total energy of the original neutron from these secondary events².

Instead, it is common practice to time the neutron over a known distance. The resulting time-of-flight (TOF) may then be used to determine the kinetic energy (E_k^n) of the neutron by:

$$E_k^n = \frac{1}{2}m_n \left(\frac{d}{TOF} \right)^2, \quad (2.4.2)$$

where m_n is the mass of the neutron and d is the known distance. This timing difference which leads to TOF can be obtained in several ways. For example, detectors at spallation

²A neutron calorimeter is special detector designed to detect all of the secondary events associated with a neutron and in doing so, establish the energy of the original neutron. Calorimeters are very complicated and expensive devices.

facilities use the pulse timing of the proton beam incident on the target as a reference point. The PUG project will attempt to measure TOF without an external trigger, instead looking at the time difference between the neutron signals in the upstream and downstream bars.

Chapter 3

Materials

3.1 Detector Development

The design of the detector was constrained by the scintillator material, light-guides and photomultiplier tubes (PMTs) readily available. At the start of the project there were a total of 10 existing $300 \times 20 \times 10 \text{ cm}^3$ scintillator bars each coupled to a pair of PMTs via a pair of light guides available for modification.

3.1.1 Cutting of Scintillator

The first step was to cut 3 m long NE110 organic plastic scintillator bar to lengths of 1 m. The scintillator material is sensitive to applied mechanical and thermal stress¹ and the “softening point” of the material is $75 \text{ }^\circ\text{C}$ ². If this temperature is exceeded, the properties of the plastic are affected which will reduce the scintillation-light production of the material. Since it is not uncommon for temperatures to exceed $75 \text{ }^\circ\text{C}$ during machining, care was taken not to overheat the material. Furthermore, mechanical stress applied to the material during cutting could produce cracks, resulting in the deterioration of scintillation-light transmission. The quality of the surface finish after cutting is also vital to the transmission of light to the light guides and PMTs which are attached to the ends of the bars. Therefore, the ends of the newly cut scintillator bars were all carefully polished.

To study the best way of cutting the scintillator material, two types of hand saws and two electro-mechanical saws were used on other scrap scintillator bars of the same material. The test material was slightly smaller with a cross-sectional area of $13.5 \times 11 \text{ cm}^2$ as opposed to the $10 \times 20 \text{ cm}^2$ of the PUG bars. To keep the temperature low during cutting, a water and soap mixture was used as coolant. The TPI indicates how many “teeth per inch” the cutting tool has and is directly proportional to the mechanical strain put on the material being cut. A lower TPI usually means larger teeth and a more “aggressive” cut while a larger TPI means smaller teeth and a “finer” cut.

¹*Machining and polishing of plastic scintillators*, Eljen Technologies.

²Eljen Technologies material documentation EJ-208 (NE110 equivalent material).

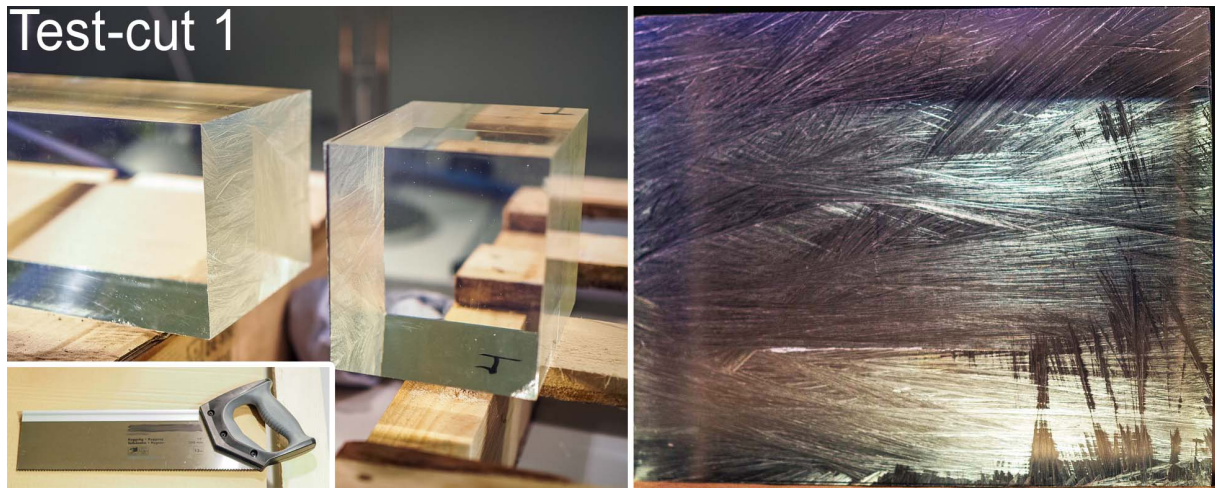


Figure 3.1.1: Scintillator Test-cut 1, performed using a 13 TPI handsaw. (left panel) the cut-off piece and (right panel) a close-up of the surface finish (right panel) for Test-cut 1 is shown. An image of the saw used to perform this cut is included in the bottom left panel corner.

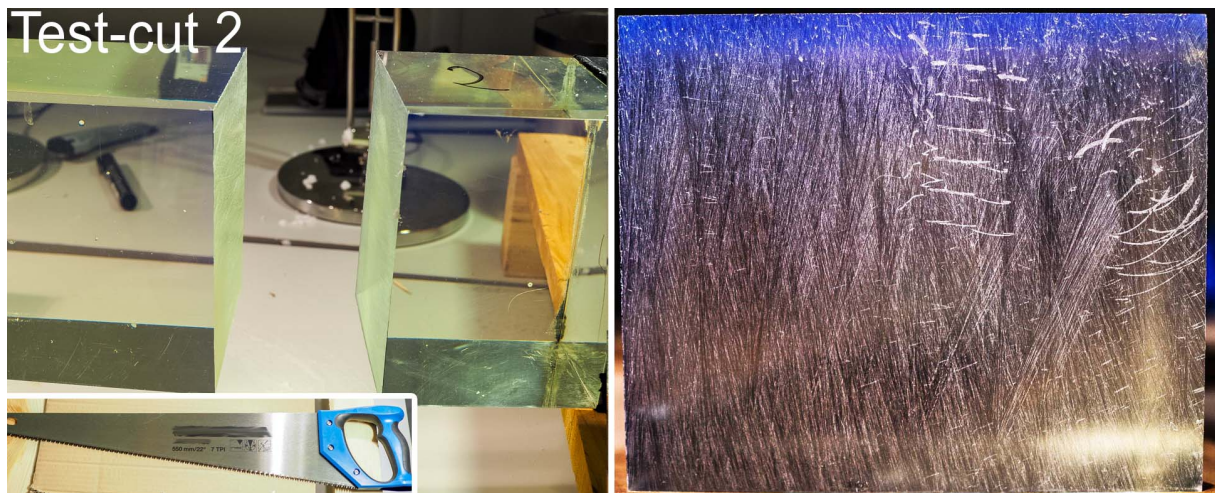


Figure 3.1.2: Scintillator Test-cut 2, performed using a 7 TPI handsaw. (Left panel) the cut-off piece and (right panel) a close-up of the surface finish for Test-cut 2 is shown. An image of the saw used to perform this cut is included in the bottom left panel corner.

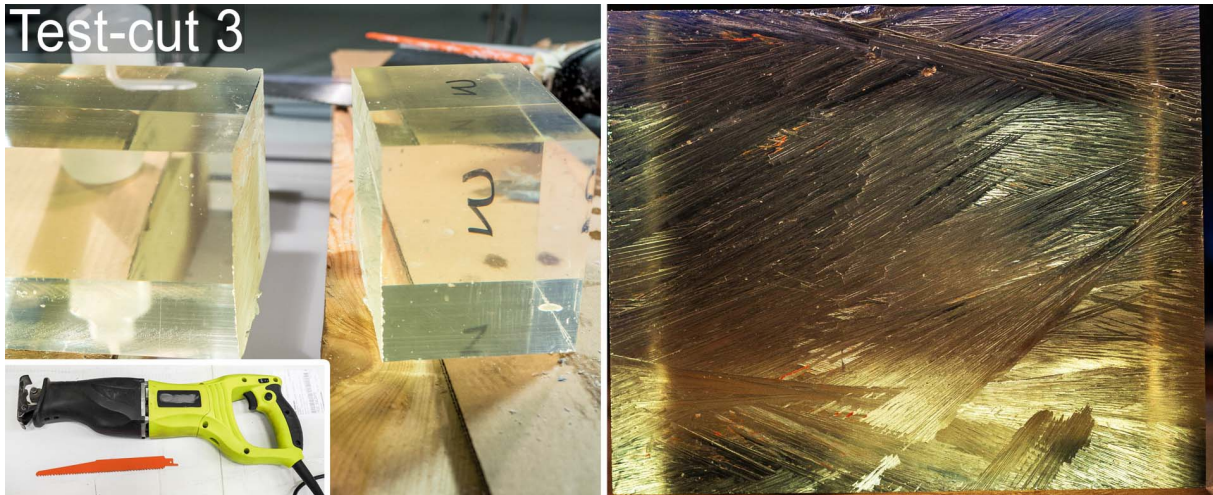


Figure 3.1.3: Scintillator Test-cut 3, performed using a 6 TPI bi-metal blade on reciprocating saw. (Left panel) the cut-off piece and (right panel) a close-up of the surface finish for Test-cut 3 is shown. An image of the saw used to perform this cut is included in the bottom left panel corner.

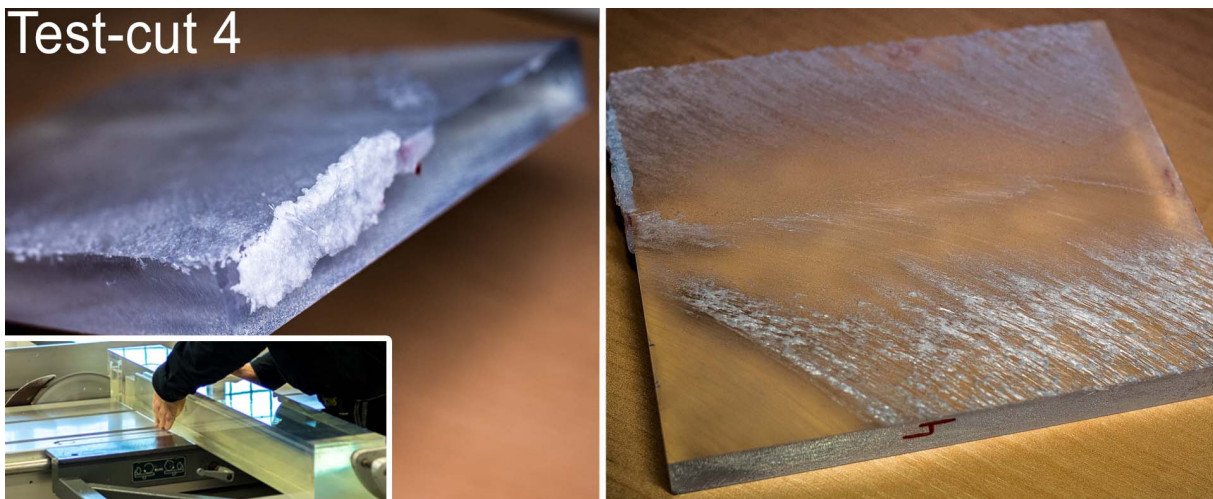


Figure 3.1.4: Scintillator Test-cut 4, performed using an Industrial table saw with a carbide-tip blade. (Left panel) the cut-off piece and (right panel) a close-up of the surface finish for Test-cut 4 is shown. An image of the saw used to perform this cut is included in the bottom left panel corner.

The surfaces resulting from Test-cut 2 were smoother compared to the other surfaces of the other tests. Test-cut 1 and Test-cut 3 both performed well but resulted in slightly worse surfaces. Test-cut 4 was simply too aggressive and quickly melted the material. As shown in Fig. 3.1.4, the start of the cut resulted in a smooth finish, but as the blade cut deeper into the material the softening temperature was exceeded and it melted. Conceivably, if the speed of the saw used in Test-cut 4 could be significantly lowered and coolant used, this method may be of use. After the cutting tests, the bars were monitored for any cracking but no change was observed for any of the bars.

The Test-cut 2 method was selected for cutting the 3 m bars to length. To keep the saw perpendicular to the bar during the cut, a jig was constructed. A straighter cut

means that less material needed to be taken off during the subsequent polishing. Figure 3.1.5 shows the ends of the 1 m scintillator bars after cutting and polishing. Eight bars (plus one spare) were produced. The polishing was outsourced to a mechanical workshop [21] where they used a vertical mill to take off material in many very shallow passes.

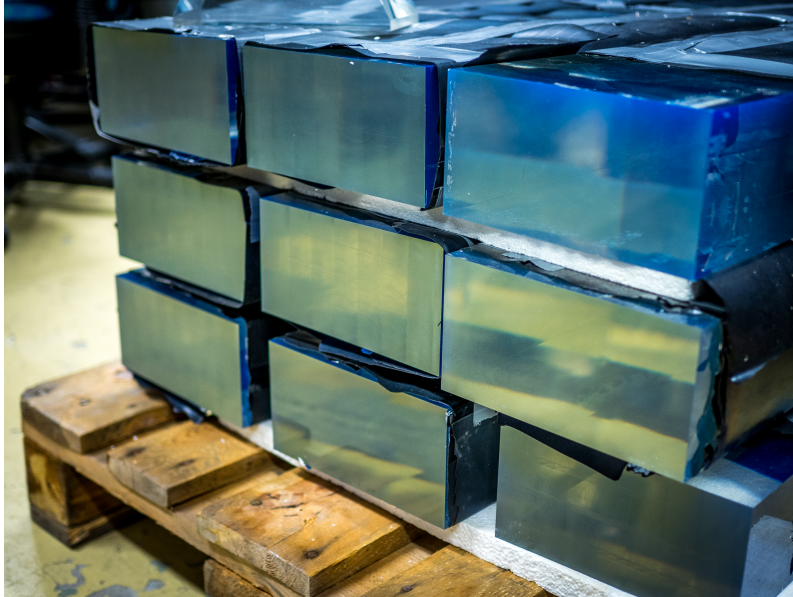


Figure 3.1.5: Photo of scintillator bars after cutting and polishing.

3.1.2 Wrapping

The next step was to glue two of the light guides and PMTs onto the ends of the newly polished scintillator bars using EPO-TEK 301-2 optically transparent epoxy. Two scintillator bars were assembled for testing. Once the glued had dried, the bars needed to be made light tight. This was done by first wrapping the scintillator bar in one layer of 0.03 mm thick aluminium foil (Fig. 3.1.6a). The purpose of the aluminium foil is two-fold. It adds a layer of material which helps to block external light but also acts as a reflector for the scintillation light, a portion of which might otherwise escape the detector. Subsequently, all corners and joints were reinforced with one layer of 0.2 mm thick vinyl tape (Fig. 3.1.6b) and finally two layers of 0.1 mm thick matte-black vinyl were wrapped over the entire length of the bars (Fig. 3.1.6c).

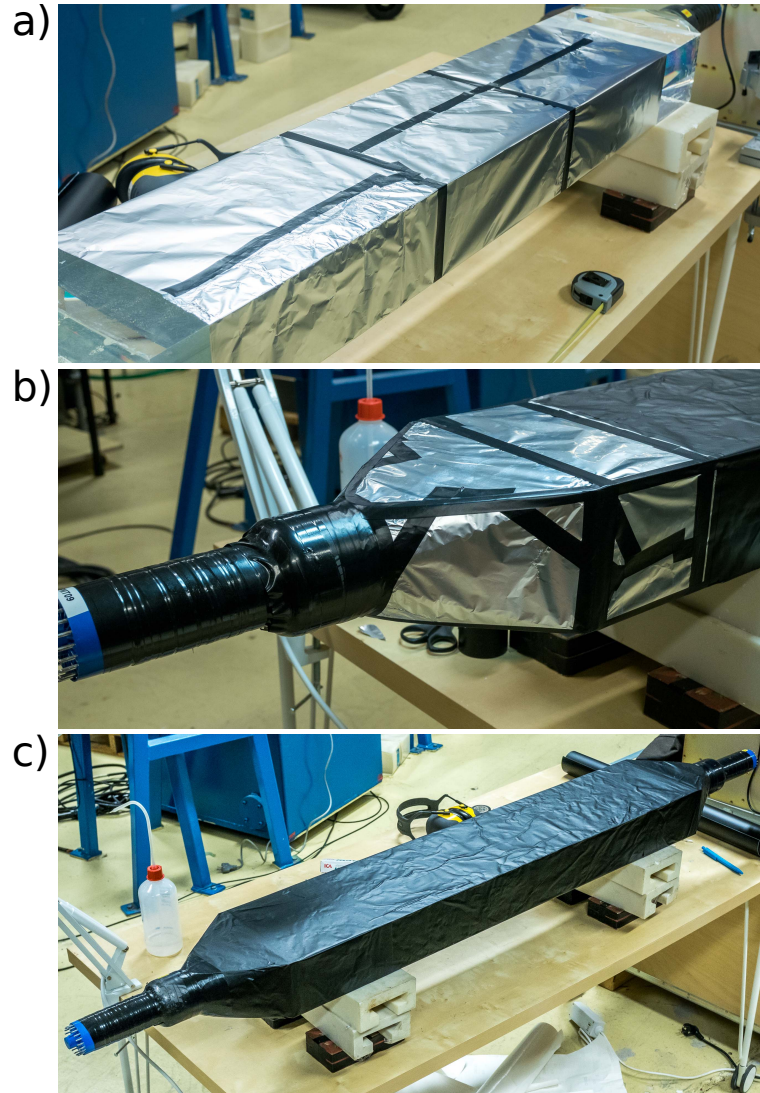


Figure 3.1.6: Images showing the wrapping of the scintillator bars. (a) aluminium foil, (b) vinyl tape reinforcement, (c) two layers of vinyl.

3.1.3 Light-Leak Tests

Three tests were performed to verify how light tight the newly wrapped bars were. One of the PMTs was powered and its signal recorded with a Teledyne Lecroy HD04054 digital oscilloscope. First, the signal was recorded with the newly wrapped bar. Then, a layer of thick fabric was wrapped around the scintillator detector. And finally, the room was darkened. A trigger threshold of -20 mV DC set at the oscilloscope was used for all measurements. The trigger rates from the oscilloscope were recorded and normalised against a 300 s measurement time.

	Wrapped	Wrapped+Fabric	Wrapped+Fabric+Dark room
Rates [s^{-1}]	22.4 ± 0.1	21.9 ± 0.1	20.4 ± 0.1

Table 3.1.1: Results from light-leak tests. Count rates registered by the oscilloscope as a function of wrapping.

As shown in Table 3.1.1, the rate is reduced slightly when extra fabric is added and

slightly further when the lights are turned off. There seems to be a very low level of external light leaking through the wrapping. Since the primary function of the wrappings around the scintillator bars is to prevent external light from overloading the extremely light sensitive PMTs, the slight increase ($\sim 9\%$) in count rate that was observed was determined to be manageable.

3.1.4 PUG Configuration

The design for the full sized PUG detector consists of two separate detector planes to enable tracking and reconstruction of particle trajectories. The distance between the two detector planes to be is variable to allow for the optimization of the balance between tracking resolution and count rate.

The final detector design consists of eight $100 \times 20 \times 10 \text{ cm}^3$ plastic scintillator bars in a two-array configuration (see Fig. 3.1.7). Each bar is equipped with two Philips XP 4312-B PMTs and both arrays will be stacked mutually perpendicular to define an xy coordinate system. This allows for a better position resolution since the event location along each bar can be derived from the timing difference between the signals in both PMTs. The sensitive detection area is $0.8 \times 0.8 \text{ m}^2 = 0.64 \text{ m}^2$.

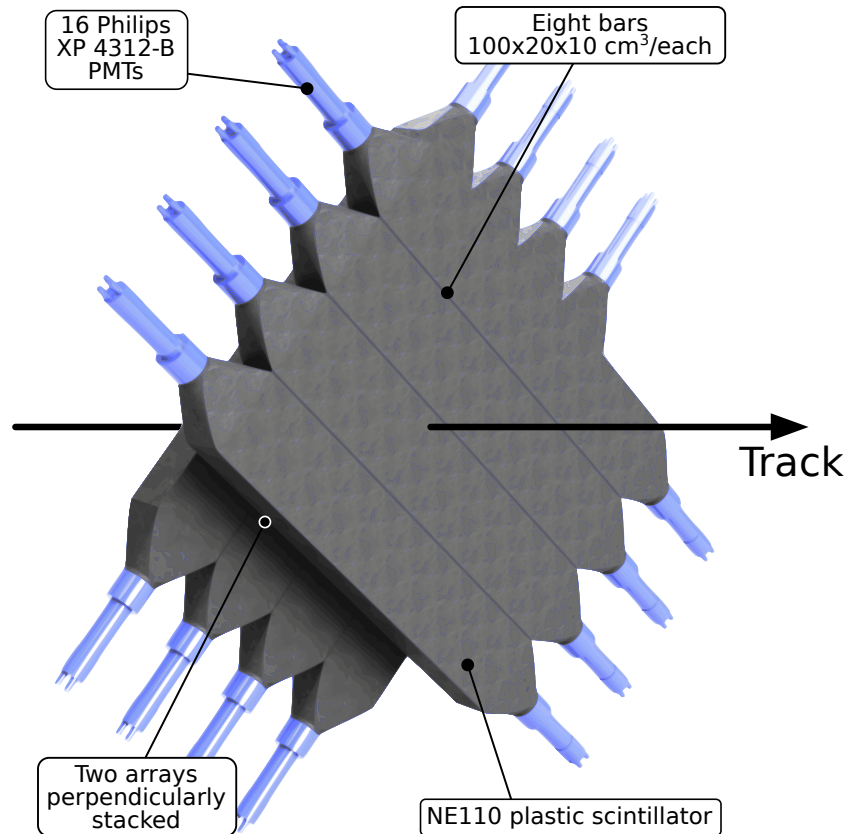


Figure 3.1.7: Scintillator-bar configuration. The scintillator material and light guides are shown in black and the PMTs are shown in blue.

The full-sized detector will have each of the detector arrays independently supported by identical frames. The frames allow the detector arrays to be independently positioned relative each other. Figure 3.1.8 shows one of the detector frames together with the scintillator bars. The scintillator bars are supported by a two-piece inner frame construction

which is suspended from the main frame by steel cables (not shown) with four sets of turn-buckles. The turn-buckles will allow for fine adjustment of the position of the inner frame. One detector array, including scintillators and its inner and outer frame, will weigh about 240 kg with external dimensions $210 \times 190 \times 30 \text{ cm}^3$ (not including the legs). Each detector frame is also equipped with lockable casters and four eye-bolts for crane suspension.

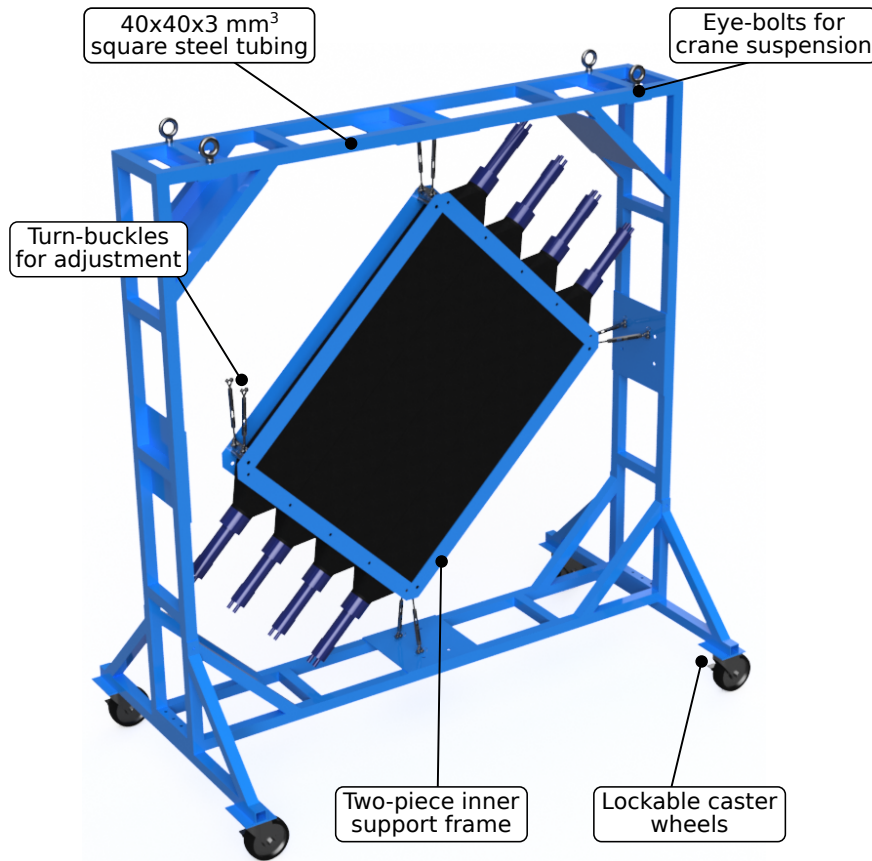


Figure 3.1.8: Design of detector frame. The scintillator bars and inner frame construction is also shown.

A static load simulation made with Autodesk Fusion 360 (2.0.2604), including the weight of the main frame, was performed. This resulted in a better understanding of the propagation of strain throughout the frame as the weight of the detector array ($\sim 120 \text{ kg}$) is applied. Weaker parts of the design were then reinforced accordingly. In this way, the structure was optimised for weight and rigidity. Figure 3.1.9 shows the simulated deflection of each of the attachment points of the inner frame. Technical drawings for fabrication of the main and inner frames are presented in Appendix C.

The two detector arrays are both rotated 45° from laboratory horizontal rather than having one array perpendicular to the floor and the other array horizontal. This enables the same suspension mechanism and design of the inner-support frame to be used for both detector arrays resulting in the second detector plane being a mirror image of the first. This also simplifies the CAD drawings and therefore the manufacturing, which reduces the cost.

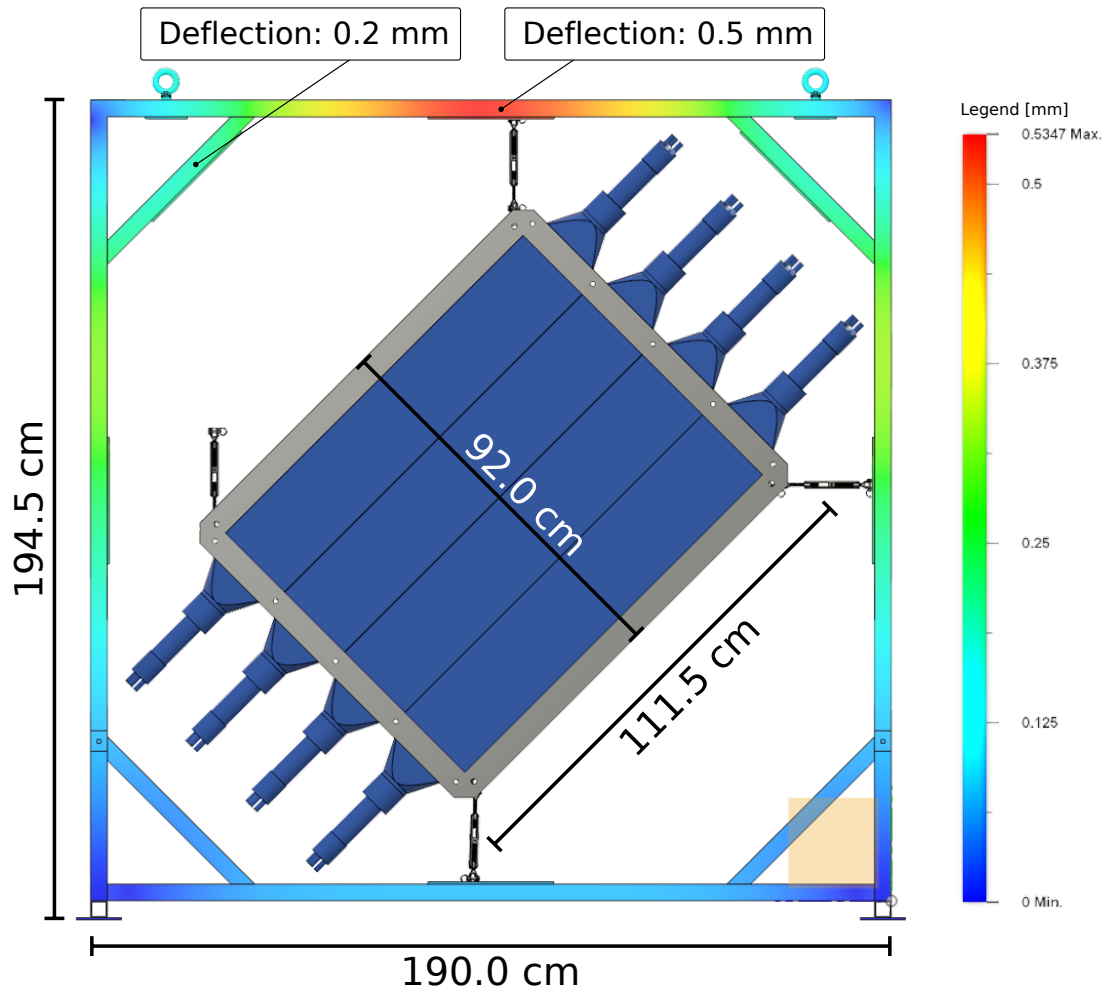


Figure 3.1.9: Static load simulation of frame. The deflection of the frame at the two load bearing points is shown along with the dimensions. The legend shows the deflection in units of mm. Red corresponds to regions of greater deflection while blue corresponds to no deflection whatsoever.

3.2 Detector-Response Study

To verify the functionality of the detector material and PMTs, several tests were devised to study the energy resolution, position resolution and light attenuation using cosmic-ray muons.

3.2.1 Cosmic-Ray Muons

Cosmic-ray muons are useful for the characterization and calibration of particle detectors [22]. On earth, these muons have an average flux-density of $\sim 1 \text{ cm}^{-2}\text{min}^{-1}$ at sea level and energies on the order of GeV [18]. Their mean-free path and energy deposition is very well known.

Figure 3.2.1 shows the stopping power of the plastic scintillator material NE102 for cosmic-ray muons. NE102 is equivalent to the NE110 material used for the detector in this project. Given the very high energies involved, the stopping power is 2 MeV/cm and since each scintillator bar is 10 cm thick, a cosmic-ray muon will deposit 20 MeV as it passes vertically through scintillator.

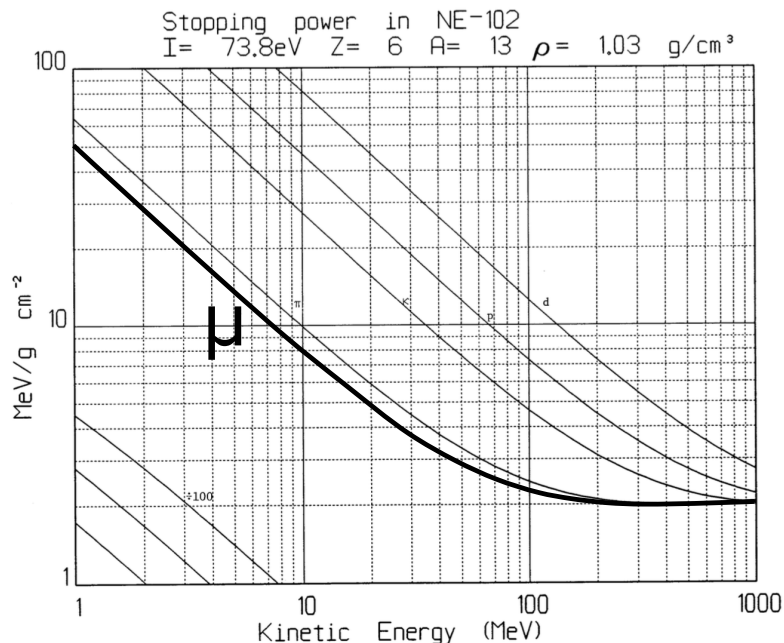


Figure 3.2.1: Stopping power of charged particles in NE102 plastic scintillator. For the cosmic-ray muons (μ) with GeV energies, the stopping power is 2 MeV/cm. Figure from [23].

3.2.2 Setup

Figure 3.2.2 shows the cosmic-ray muon setup for an uncut 3 m long scintillator bar. The general setup consists of two smaller scintillator “pads” and PMTs, one placed above (Top_{PMT}) and one below ($\text{Bottom}_{\text{PMT}}$) the main bar, used for defining the “cosmic-ray muon trigger”. The sizes of these scintillator pads are $10 \times 10 \times 0.5 \text{ cm}^3$. The purpose of the cosmic-ray muon trigger is to constrain the data readout of the main bar to cosmic-ray muons which hit at specific positions. Three experiments were performed: energy

resolution, position resolution and scintillation-light attenuation.

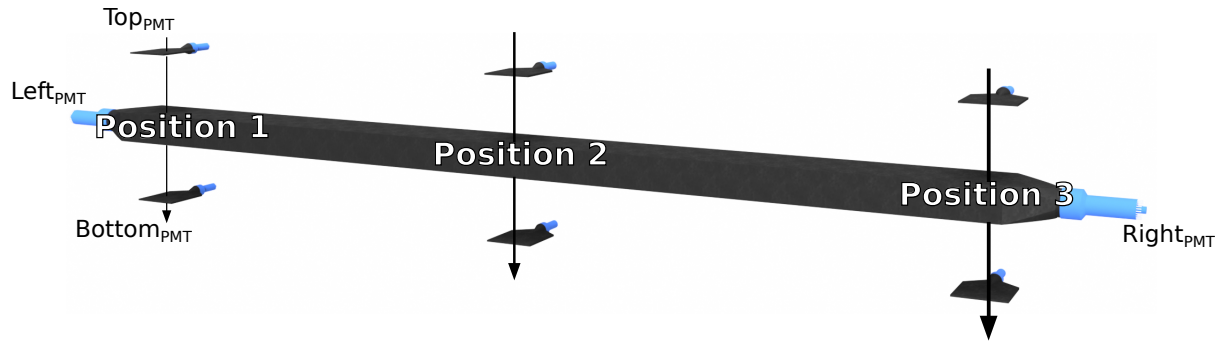


Figure 3.2.2: Cosmic-ray muon experimental setup. The long black rectangle is the scintillator bar and the PMTs are blue. Three trigger scintillator pads and cosmic-ray muon-trajectories are also indicated.

The muon-trigger schematic shown in Fig. 3.2.3 is common for all three experiments. It creates a trigger for a Teledyne Lecroy HD04054 digital oscilloscope (DAQ) which saves the signal waveforms from $\text{Right}_{\text{PMT}}$ and Left_{PMT} connected to the scintillator bars. The two constant-fraction discriminators (CFD) produce logic signals for any input signals above a pre-set threshold (see Sec. 2.3). The logic signal from each of the CFDs is passed to a coincidence module (&). If there is a simultaneous signal in both Top_{PMT} and $\text{Bottom}_{\text{PMT}}$, a trigger is created and the signal waveforms recorded. Since cosmic-ray muons have relativistic velocities, the time they take to travel between Top_{PMT} and $\text{Bottom}_{\text{PMT}}$ is negligible. Given a distance between Top_{PMT} and $\text{Bottom}_{\text{PMT}}$ of 30 cm, a cosmic-ray muon with a kinetic energy of 1 GeV will traverse this distance in ~ 0.2 ns. This time difference is indistinguishable to the coincidence module.

Prior to any measurements, both the PMTs connected to the bar were gain matched so that the amplitude of their signals were as identical as possible. This was achieved by placing the cosmic-ray muon trigger paddles in the center of the main bar (Position 2) and adjusting the voltage applied to each PMT.

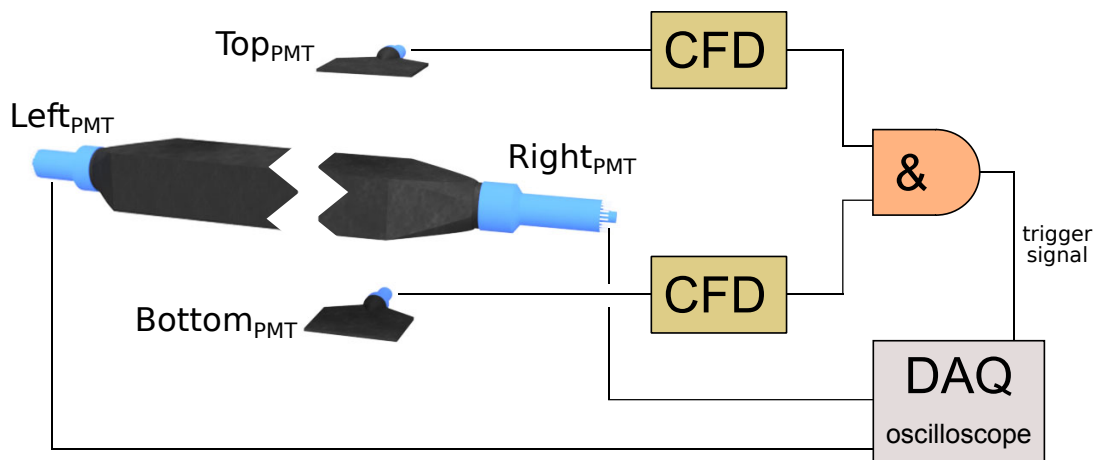


Figure 3.2.3: Muon-trigger electronics. (Left) the scintillator bar and cosmic-ray trigger scintillators are shown in black and the PMTs in blue. (Right) processing electronics block diagram.

3.2.3 Energy Resolution

Energy resolution studies were performed with the bar cut to its nominal 1 m length. Determinations of the energy resolution were performed for three different means of attaching the light guides to the scintillator bars: dry-fitted, greased (using Saint Gobain BC-630) and glued (using EPO-TEK 301-2). The results were obtained by plotting the integrated values of each pulse and fitting a Gaussian function to the distribution.

All cosmic-ray muon based analysis was performed using the digitized files from the DAQ oscilloscope and custom Python-based code. The deposited energy was obtained by integrating each pulse above a certain threshold (set at 10% of rise time) over time (see Figure 3.2.4). Using the rise time to set a threshold is more reliable than finding the maximum signal amplitude, since this point might not be very well defined depending upon the sampling frequency. The integral of the pulse is a direct measurement of the charge collected by the PMT and is therefore also proportional to the energy deposited by the cosmic-ray muon in the scintillator material.

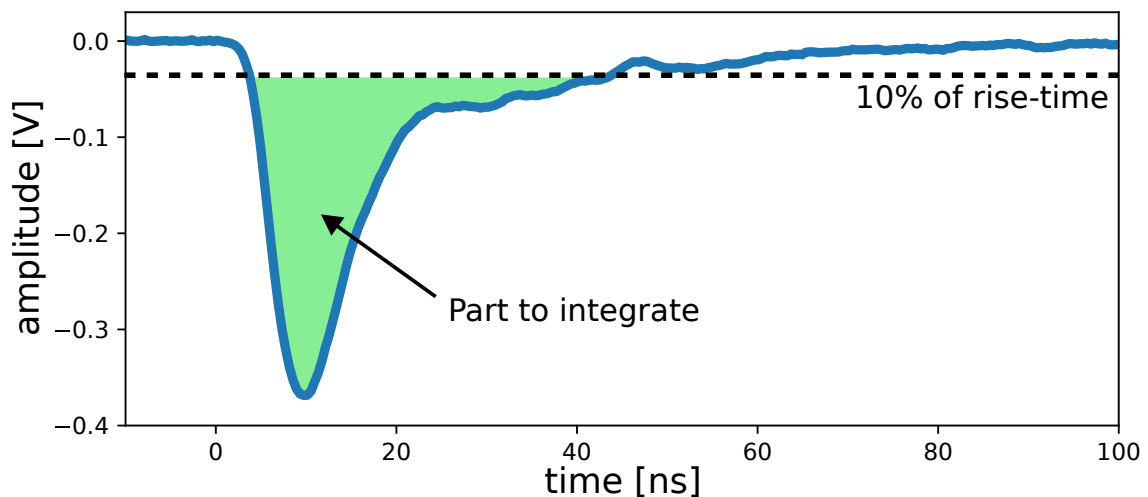


Figure 3.2.4: Cosmic-ray muon signal and integration. The dashed line represents the threshold at 10% of the signal rise time, above which the signal is integrated (green area).

All resolutions are based on the expected 20 MeV energy deposition of the cosmic-ray muon. The resolution R_{local} is given by

$$R_{\text{local}} = \frac{FWHM}{\mu}, \quad (3.2.1)$$

where $FWHM$ is the full-width-at-half-maximum and μ is the mean position of the normally distributed (Gaussian) peak. The $FWHM$ relates to the standard deviation (σ) as $FWHM = 2.355\sigma$, which then gives

$$R_{\text{local}} = 2.355 \cdot \frac{\sigma}{\mu}. \quad (3.2.2)$$

Figure 3.2.5 together with Table 3.2.1 shows the energy resolution from the three different means of attaching the light guide and PMT to the scintillator material.

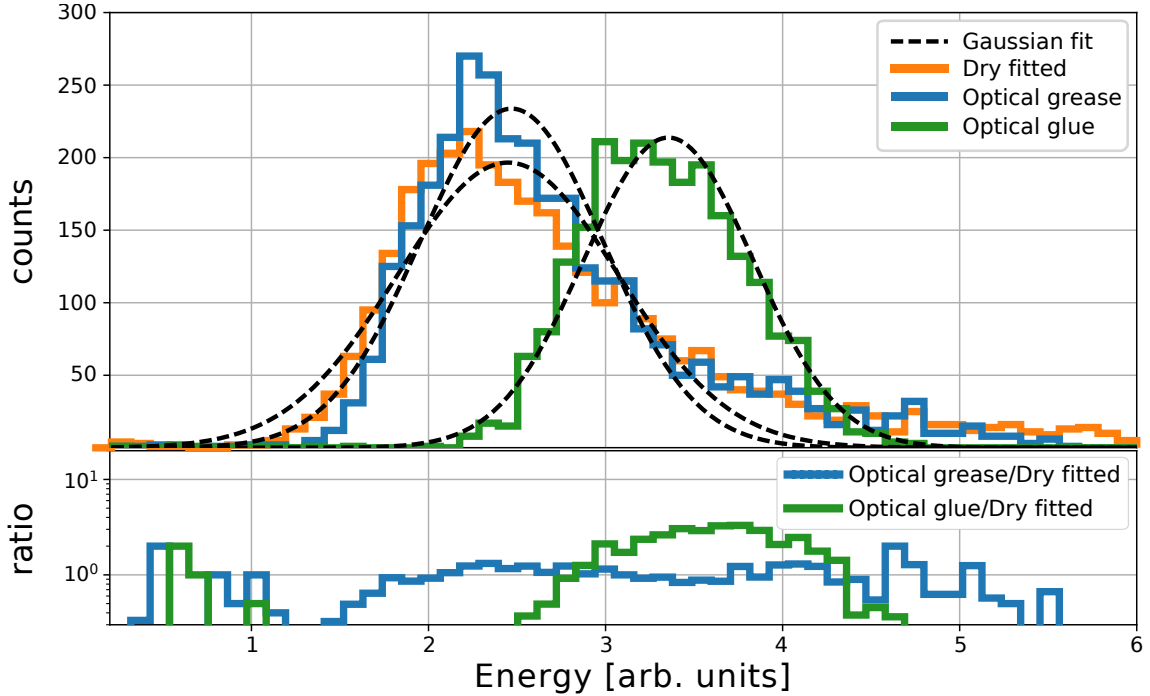


Figure 3.2.5: Energy resolution of NE110 for 20 MeV cosmic-ray muons. The top panel shows histograms of the integrated signal values for the three different cases. The bottom panel shows the ratio to the dry-fitted result. Results from three different means of attaching the light guides are: dry-fitted (orange), optical grease (blue) and optical glue (green). Corresponding Gaussian fit functions are shown as black dashed lines.

Technique	μ [arb. units]	σ [arb. units]	R_{local} [%]
Dry fitted	2.45 ± 0.03	0.63 ± 0.03	59.98 ± 2.68
Optical grease	2.47 ± 0.02	0.52 ± 0.02	49.36 ± 1.78
Optical glue	3.36 ± 0.01	0.48 ± 0.01	33.53 ± 0.72

Table 3.2.1: Energy-resolution measurements. The mean position (μ), standard deviation (σ) and resolution (R_{local}) at 20 MeV are shown.

The optical glue produced both a superior resolution compared to the other attachment methods and also a higher mean distribution value. The latter indicates that more scintillation light is transmitted across the scintillator/light guide surface. Both highlight the superior performance of optical glue compared to the other two methods and indicate a more homogeneous and solid bond between the scintillator material and the light guide. Surprisingly, the optical grease did not far outperform the dry fitted method. The optical grease produced a slightly better resolution but with a similar mean value. This could be due to the fact that the optical grease was not uniformly distributed.

3.2.4 Position Resolution

The position resolution of the detector is a measure of how well the location of the cosmic-ray muon interaction can be determined along the length of the scintillator bar. This parameter is key to the potential tracking capabilities of the full-sized detector system.

The time difference (Δt) between the arrival of the $\text{Right}_{\text{PMT}}$ signal and the arrival of the Left_{PMT} signal was determined according to

$$\Delta t = |t_{\text{Right}} - t_{\text{Left}}|. \quad (3.2.3)$$

Referring to Fig. 3.2.2, the first measurement was taken with the cosmic-ray muon trigger in the middle of the main bar (Position 2) which gives a light-path difference of $\Delta d = 0$ cm. Two other positions were then selected to increase the light-path difference to $\Delta d = 40$ cm and $\Delta d = 100$ cm, respectively. The Δt distribution of 2500 events was then plotted for each Δd .

As shown in Fig. 3.2.6, the time difference is measured from a point localized at 10% of the rise time of the signal. Whether or not the $\text{Right}_{\text{PMT}}$ or Left_{PMT} signal comes first is dependent on the experimental setup and is also arbitrary as far as the time difference is concerned. As can be seen, the signal amplitude is also different depending upon the experimental setup, which is due to the attenuation of the scintillation light as it passes along the difference lengths of the scintillator bars (see Sec. 2.2).

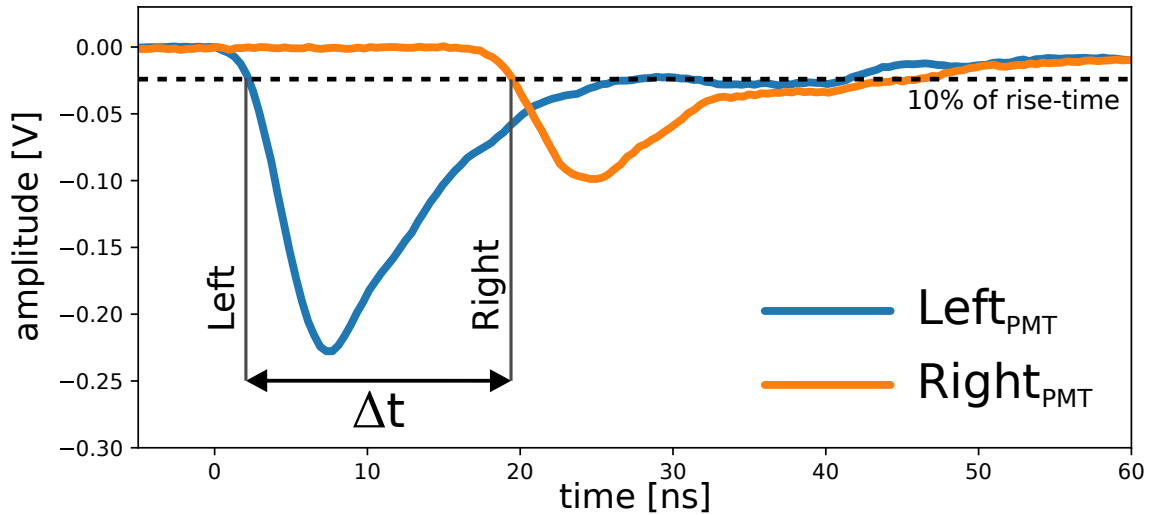


Figure 3.2.6: Time difference between two cosmic-ray muon signals. The dashed line represents the threshold cut used to determine the timing. The time difference Δt is calculated between the points (vertical bars) at which the signal exceeds the threshold. The trigger paddles were closer to the Left_{PMT} .

Figure 3.2.7 together with Table 3.2.2 shows the results of the position resolution study. With the time difference Δt between $\text{Right}_{\text{PMT}}$ and Left_{PMT} signal, it is possible to clearly differentiate the positions of the interaction. For comparison, the last column of Table 3.2.2 shows the theoretical distance d' light would travel within the scintillator material given the measured mean value (μ) as

$$d' = \mu \cdot \frac{c}{1.58}, \quad (3.2.4)$$

where c is the speed of light in a vacuum and 1.58 is the index of refraction of the scintillator material.

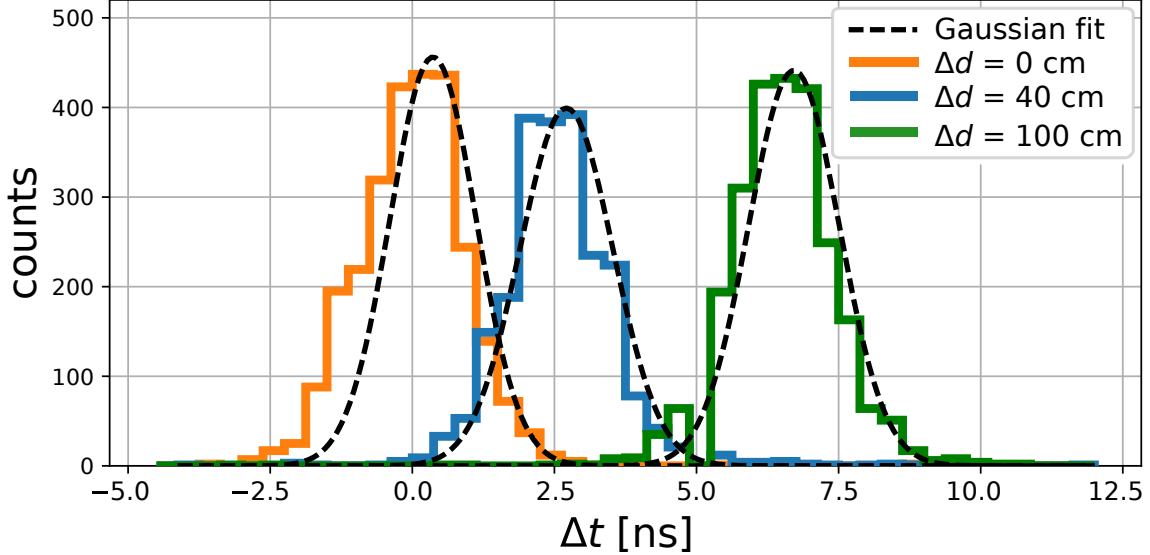


Figure 3.2.7: Relative pulse timing. The path-length differences between the two pulses are shown for (orange) $\Delta d = 0$ cm, (blue) $\Delta d = 40$ cm and (green) $\Delta d = 100$ cm. Corresponding Gaussian fit functions are shown as black dashed lines.

Position [cm]	μ [ns]	σ [ns]	d' [cm]
1: $\Delta d = 0$	0.36 ± 0.04	0.76 ± 0.04	6.8 ± 0.08
2: $\Delta d = 40$	2.71 ± 0.02	0.82 ± 0.02	51.4 ± 0.04
3: $\Delta d = 100$	6.71 ± 0.02	0.80 ± 0.02	127.3 ± 0.04

Table 3.2.2: Position-resolution measurements. The mean position (μ), standard deviation (σ) and the distance traversed d' are shown.

It is clearly possible to distinguish the point of interaction across a 1 m length of scintillator bar with a precision of better than 1 ns. The theoretical distance d' calculated from Eq.(3.2.4) is very close to the measured value for each case. The fact that they are all slightly larger may be attributed to the fact that the cosmic-ray muon trigger paddles have 10 cm wide surfaces which introduces uncertainty in the position of the cosmic-ray muon interaction. Furthermore, it is also very likely that the scintillation light produced by the ionizing cosmic-ray muon does not travel in a straight line to the PMT, but rather reflects off the inside of the scintillator material and takes a slightly longer time to reach the PMT.

3.2.5 Light-Attenuation Length

As discussed in Sec. 2.2, attenuation reduces the intensity of the scintillation light which reaches the PMTs. The attenuation coefficient of the scintillator material was experimentally determined and compared to the data sheet. This was done by placing the cosmic-ray muon trigger paddles at Position 1 (See Fig. 3.2.2) and calculating the ratio between the integrated signal values from $\text{Right}_{\text{PMT}}$ and Left_{PMT} . Using Eq.(2.2.1), the intensity I_0 is the unattenuated signal from Left_{PMT} while the intensity I is the attenuated signal from $\text{Right}_{\text{PMT}}$. Rewriting the equation and solving for the attenuation coefficient α gives

$$\alpha = -\frac{\ln\left(\frac{I}{I_0}\right)}{x}, \quad (3.2.5)$$

where x is the distance the light has travelled, in this case 3 m. The ratio was obtained by plotting it for 2900 events and fitting a Gaussian function to the distribution to determine the mean value. The *attenuation length* is the inverse of the attenuation coefficient.

Table 3.2.3 shows the result from the measured attenuation length (α^{-1}) compared with the data sheet. The measured attenuation length is within $\sim 6.5\%$ of the value specified in the data sheet.

	Attenuation length α^{-1} [cm]	Difference [%]
Measured value	374 ± 6	1
Data sheet	400	~ 6.5

Table 3.2.3: Attenuation-length measurement.

The difference in the measured attenuation coefficient with respect to the data sheet can most likely be attributed to the age of the scintillator material. The material is over 20 years old and it is generally accepted that the light yield of organic plastic scintillator materials diminishes over time [24].

Chapter 4

Measurement at the Source Testing Facility

4.1 Experimental Setup

Figure 4.1.1 shows an image of one of the two PUG bars which was built for the project (see Sec. 3.1).

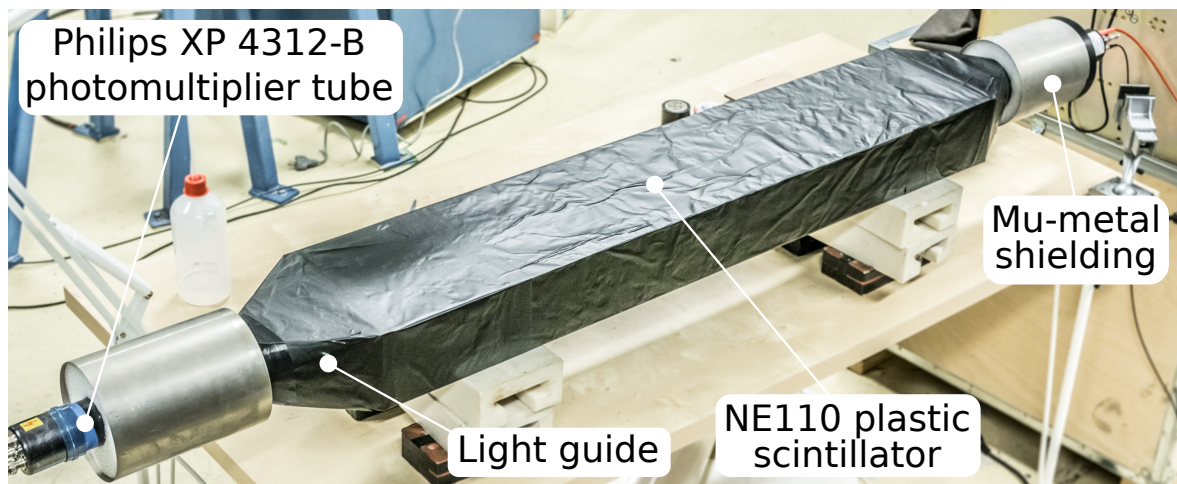


Figure 4.1.1: Photograph of a PUG bar

4.1.1 Neutron Tagging

Since the PUG is intended for fast-neutron detection, studies were performed using a pre-existing fast-neutron tagging setup [25, 26] together with a plutonium-beryllium (PuBe) neutron source. Figure 4.1.2 shows a schematic of the setup. The trigger, derived from the detection of an event in one of the PUG elements, was used to start the data-acquisition (DAQ) system, provide the integration gates for the *LG* and *SG* QDC modules and start the TOF TDC. The TOF TDC stop signal comes, after some delay, from a YAP detector.

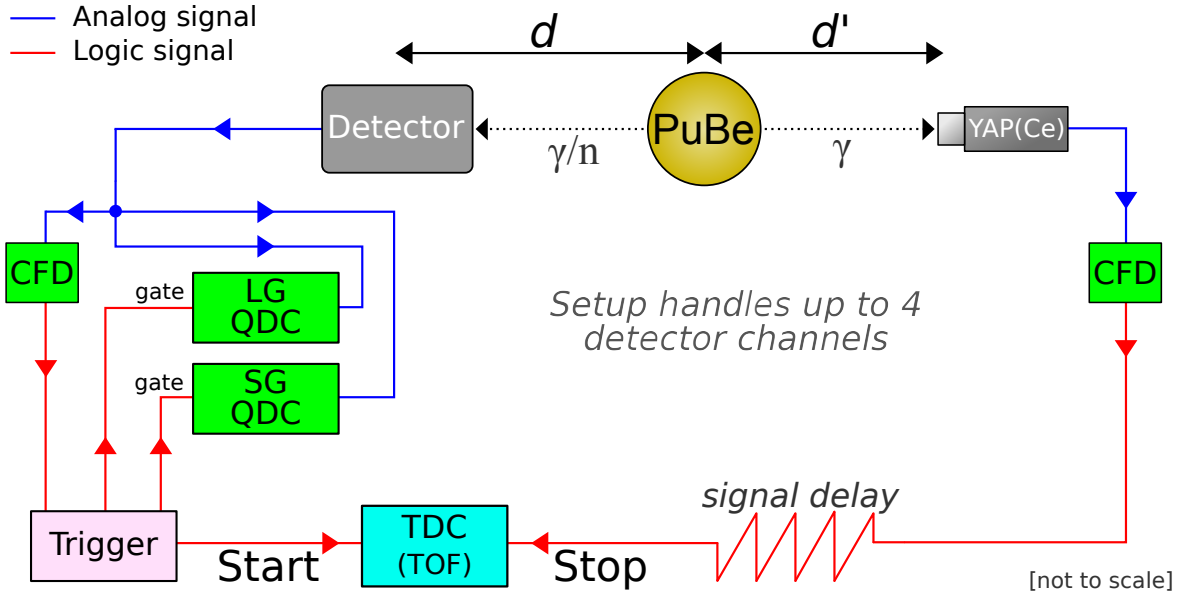


Figure 4.1.2: The fast-neutron tagging setup. The PuBe neutron source (yellow) and the Detector and YAP (gray) are shown together with a diagram of the signal-processing electronics. The analog signals are traced in blue and the logic signals are traced in red. Figure from [27].

The distance between the Detector and the center of the PuBe source is d and the distance between the YAP detector and source is d' , where d is much larger than d' . The TOF of the neutron is determined by starting and stopping a TDC in relation to the neutron-correlated emission of a 4.44 MeV γ -ray¹. Two categories of events are thus defined.

$\gamma\gamma$ -events: These events involve the simultaneous emission of two γ -rays illustrated in the top panel of Fig. 4.1.3. The emission occurs at time T_0 . Shortly thereafter, γ -ray 1 produces a signal in the YAP detector at time T_{γ_1} . Subsequently, γ -ray 2 produces a signal at time T_{γ_2} . This signal is used to start the TOF measurement. The T_{γ_1} signal is delayed with cable to arrive after T_{γ_2} and is used to stop the TOF measurement. The time differences between the signals are given by $T_{\gamma_1} - T_0 = d'/c$ and $T_{\gamma_2} - T_0 = d/c$, where c is the speed of light. For this type of event, the TOF measurement determines the time difference Δt_γ which is always the same as γ -rays all have the same speed and is marked as the “ γ -flash” in Fig. 4.1.4.

γn -events: These events involve the simultaneous emission of a neutron and an associated 4.44 MeV γ -ray from the decay of the first excited state of the carbon nucleus and is illustrated in the bottom panel of Fig. 4.1.3. The decay occurs at time T_0 . Shortly thereafter, the γ -ray produces a signal in the YAP detector at time T_{γ_1} . Subsequently, the neutron produces a signal in the Detector at time T_n . This signal is used to start the TOF measurement. The T_{γ_1} signal is delayed with cable to arrive after T_n and is used to stop the TOF measurement. The time differences between the signals are given by $T_{\gamma_1} - T_0 = d'/c$ and $T_n - T_0 = d/v_n$, where v_n is the velocity of the neutron. For this type of event, the TOF measurement determines the time difference Δt_n which is marked as “Neutrons” in Fig. 4.1.4.

¹This originates with the PuBe source from the de-excitation of ^{12}C from its first excited state according to: $\alpha + {}^9\text{Be} \rightarrow {}^{12}\text{C}^* + n$.

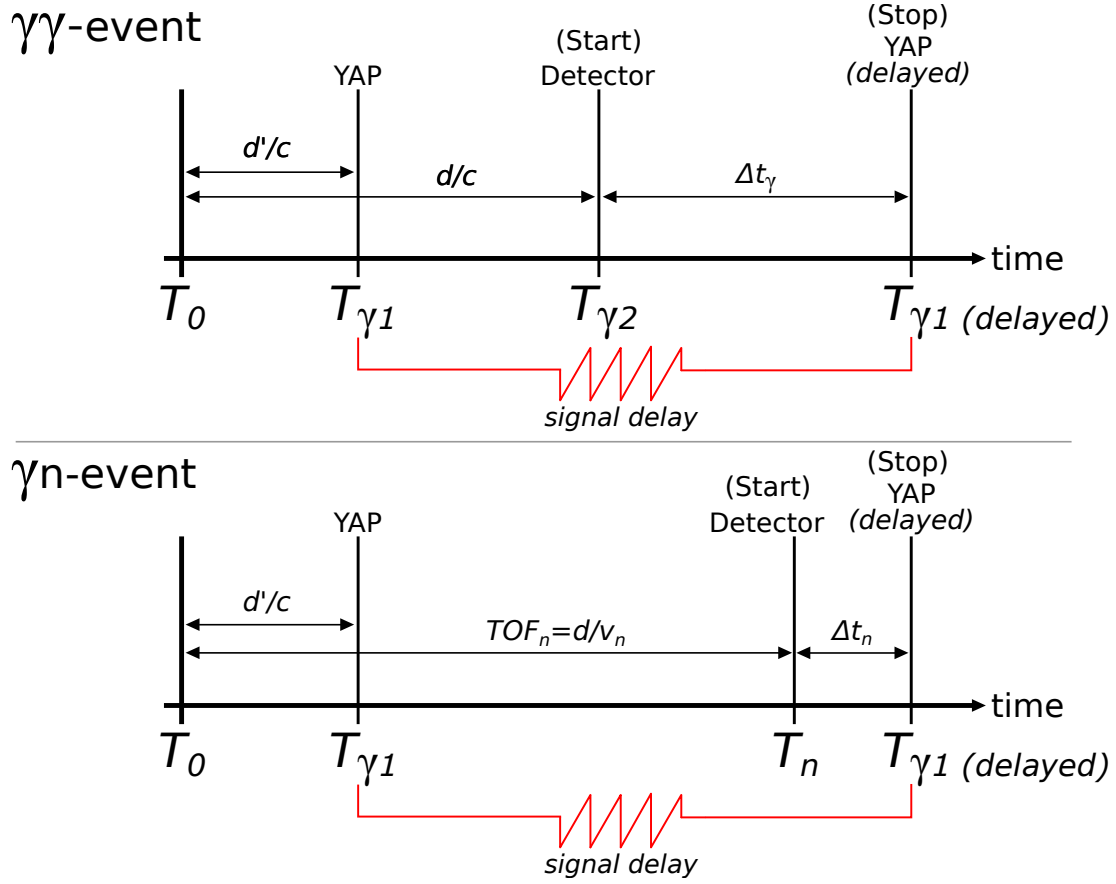


Figure 4.1.3: Real-time arrival of pulses for the TOF setup. The top panel shows the signals related to the $\gamma\gamma$ -events. The bottom panel shows the signals related to the γn -events. The vertical black lines indicate the relative arrival times of the respective signals. The red line represents the cable delay for signal $T_{\gamma 1}$.

Consider Fig. 4.1.4. The neutron TOF (TOF_n) is given by $T_0 - \Delta t_n$, where T_0 is derived from the location of the γ -flash, the known distance d and the speed of light c as $T_0 = \Delta t_\gamma + d/c$. The neutron TOF is then:

$$TOF_n = T_0 - \Delta t_n = \frac{d}{c} + \Delta t_\gamma - \Delta t_n. \quad (4.1.1)$$

Thus, perhaps even surprisingly, given the location of the γ -flash, knowledge of the distance d between the source and detector is all that is required to determine the neutron time-of-flight. This fundamental concept is the basis of the neutron time-of-flight measurements performed in this thesis.

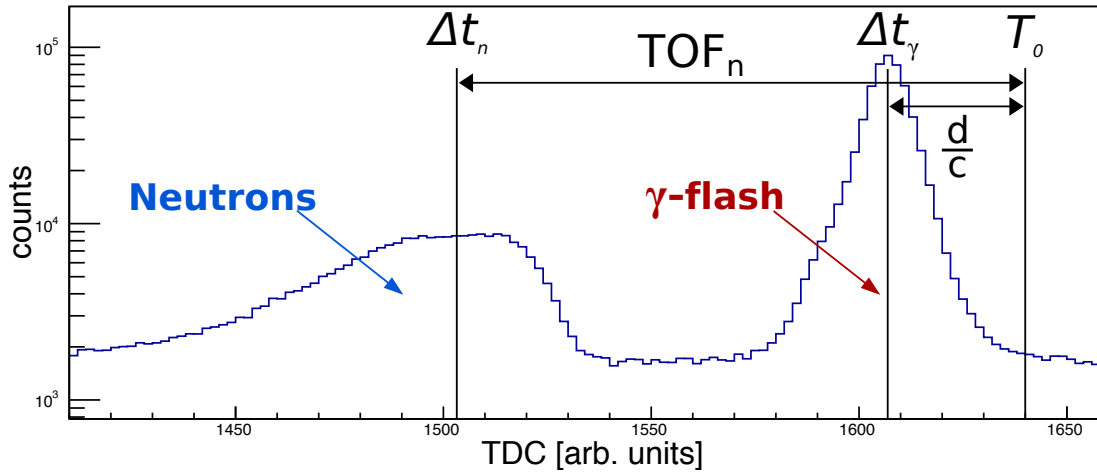


Figure 4.1.4: A typical TOF spectrum. The neutron distribution (blue, Δt_n) and the γ -flash peak (red, Δt_γ) TDC values are shown together with the location of T_0 and a flat random background. Figure from [27].

4.1.2 Measurements

Figure 4.1.5 shows a schematic of the experimental setup. The two PUG bars (Bar 1 and Bar 2) are centered in front of one of the beam ports of the “Aquarium”². Bar 1 was placed closest to the source and a NE213 liquid-scintillator detector was located downstream of both. Figure 4.1.6 shows an image of the setup with further details highlighted.

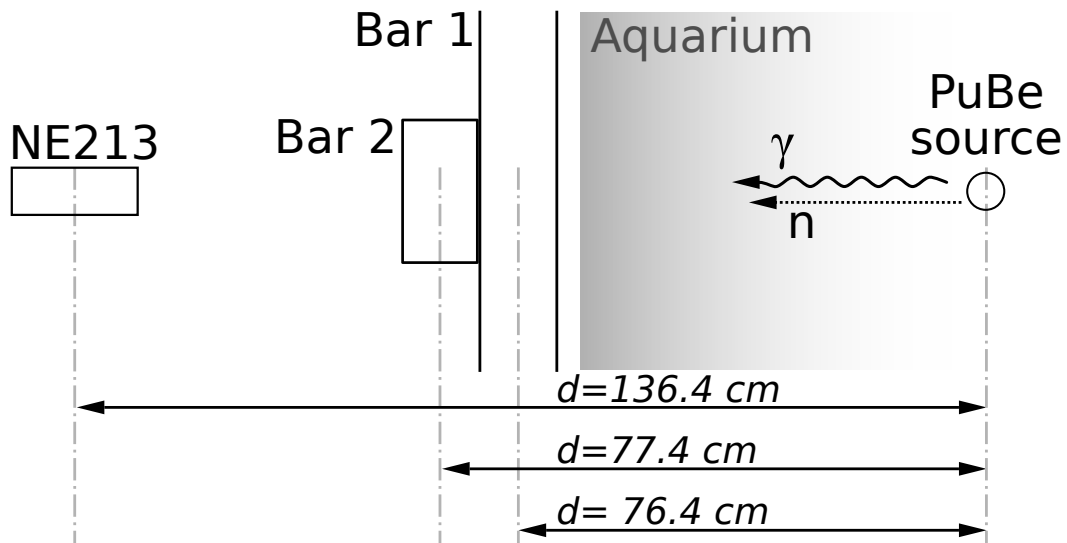


Figure 4.1.5: Experimental setup shown from the top. The Aquarium was used to define a beam of γ -rays and neutrons from the source. Centered in front of the beam port, two PUG bars (Bar 1 and Bar 2) and the NE213 detector are shown.

²The interested reader is directed to [27] for more details about the Aquarium.

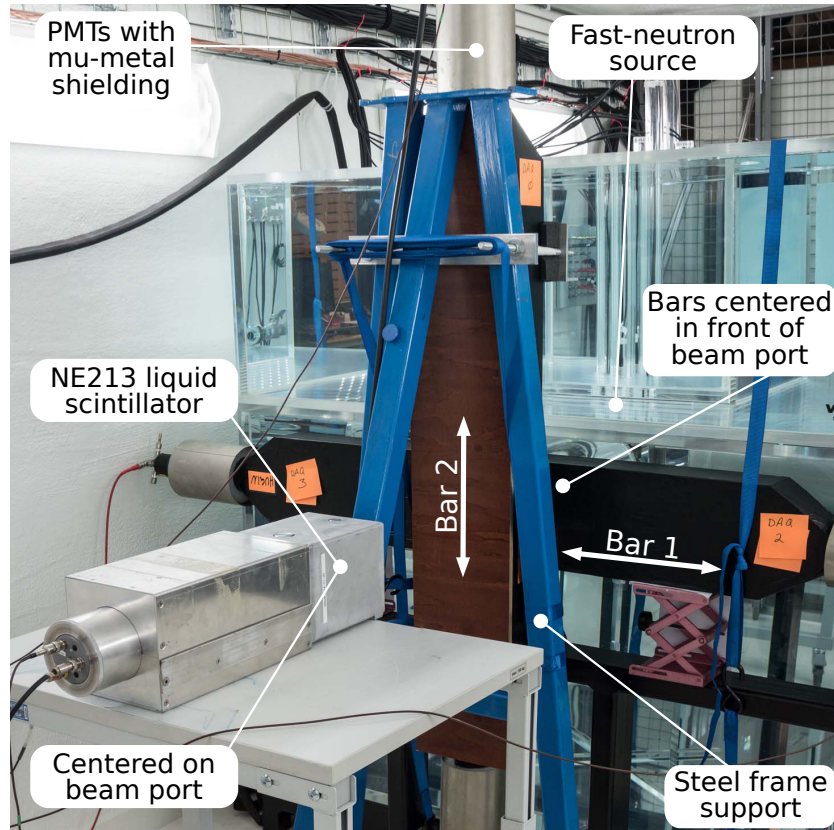


Figure 4.1.6: Photograph of the experimental setup. The view is from downstream looking back towards the source.

The idea was simple: use the NE213 detector to identify candidate neutron events and examine the response of the PUG bars to these events.

4.1.3 Definition of the Fast-Neutron Beam

To evaluate the response of the PUG bars, only events which resulted in a signal in the NE213 detector were considered. These events were plotted in a scatter plot (see Fig. 4.1.7). Events which lay in the “island” polygon were selected to be of interest. Island events were identified as neutrons with the NE213 detector by their *PS* and TOF characteristics. This method of cutting on *PS* and TOF drastically reduced the background in the PUG bars and constrained the data set to fast neutrons which essentially had a direct line of sight between the source and the NE213 detector. This geometric constraint thus resulted in neutron beam which likely passed through both Bar 1 and Bar 2.

To study the energy dependence of the corresponding signals in the PUG bars, three cuts were defined. Cut 1 considered the entire neutron island, while cuts 2 and 3 considered the higher- and lower-energy neutrons, respectively (see Table 4.1.1).

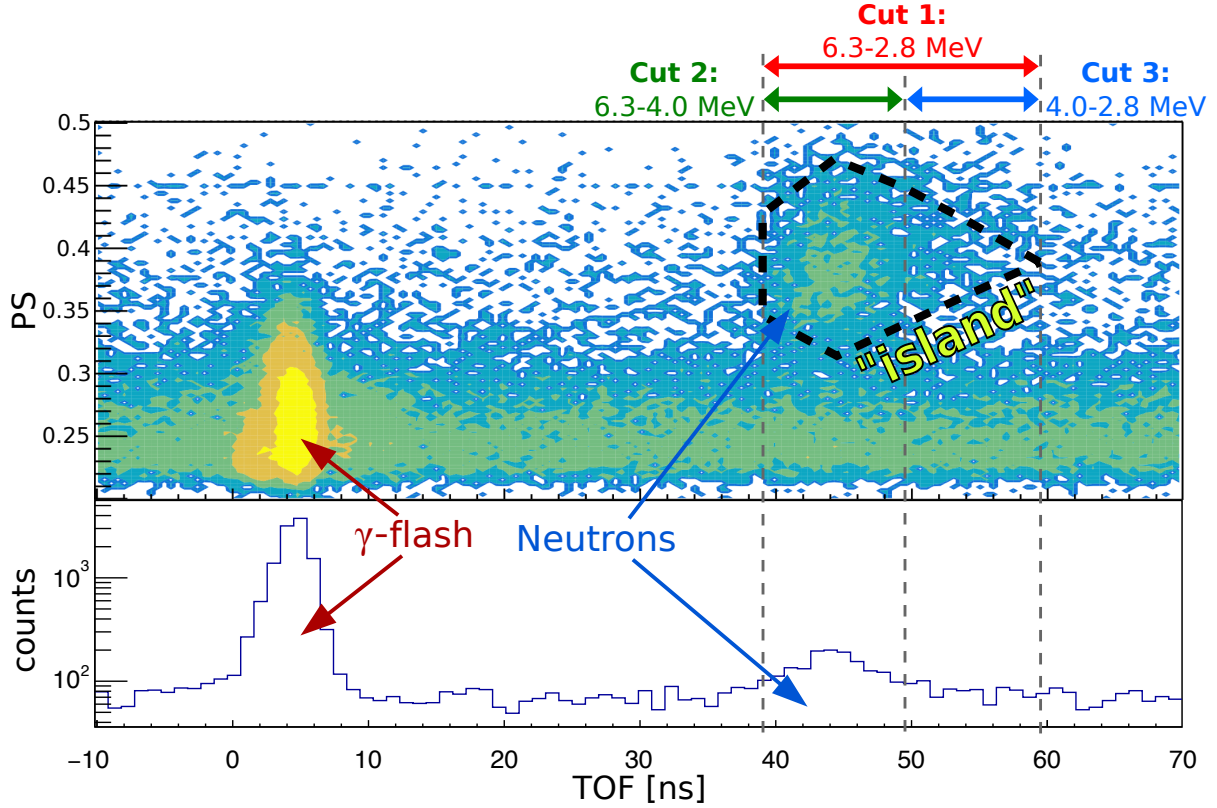


Figure 4.1.7: TOF vs PS for the NE213 detector. The top panel shows time-calibrated PS plotted against TOF. The yellow distribution is the γ -flash and the dashed black outline indicates the neutron “island”. The horizontal green band centered on $PS = 0.24$ is random events. The bottom panel shows the projection of the scatterplot onto the TOF axis. Arrows indicate the γ -flash (red) and neutron events (blue).

	TOF($d = 1.364$ m) [ns]	E_k^n [MeV]
Cut 1	39.4–59.4	6.3–2.8
Cut 2	39.4–49.4	6.3–4.0
Cut 3	49.4–59.4	4.0–2.8

Table 4.1.1: Neutron TOF cut limits for the NE213 detector. The distance $d = 1.364$ m. E_k^n is given by Eq. (4.1.1).

For the remainder of this thesis, only neutrons in this island region will be considered, and the response of the PUG bars to them will be determined.

4.2 Selected Results

4.2.1 Bar 1, Bar 2 Energy Deposition

A sketch of the prototype PUG bars together with the neutron-beam defining NE213 detector is shown in Fig. 4.2.1.

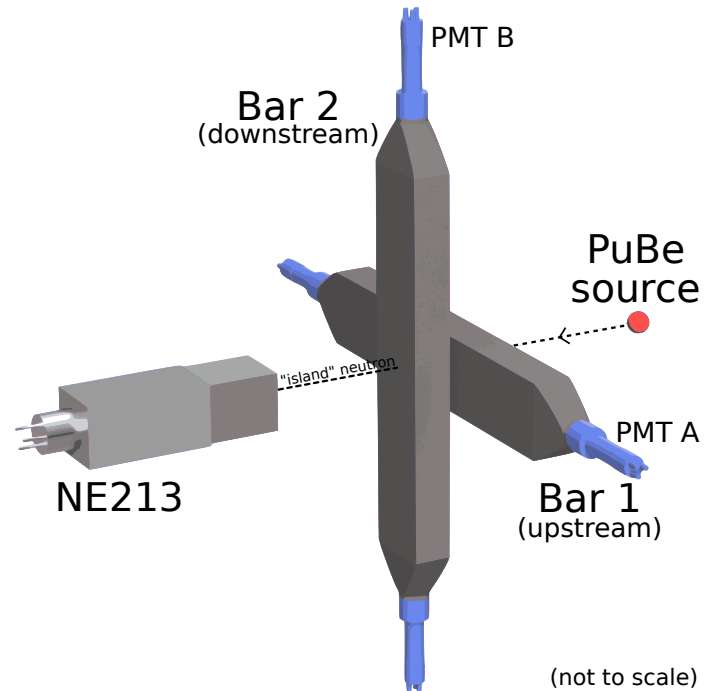


Figure 4.2.1: Experimental setup. The positions of Bar 1 and Bar 2 relative to the NE213 detector and source are shown.

Figure 4.2.2 shows deposited-energy spectra measured by PMT A of Bar 1 and PMT B of Bar 2 for events determined to be neutrons with the NE213 detector using the island-based cut described in Sec. 4.1.3. Results from only a single PMT for each bar are shown as they are representative of the spectra obtained for the other bar due to the symmetry of the setup.

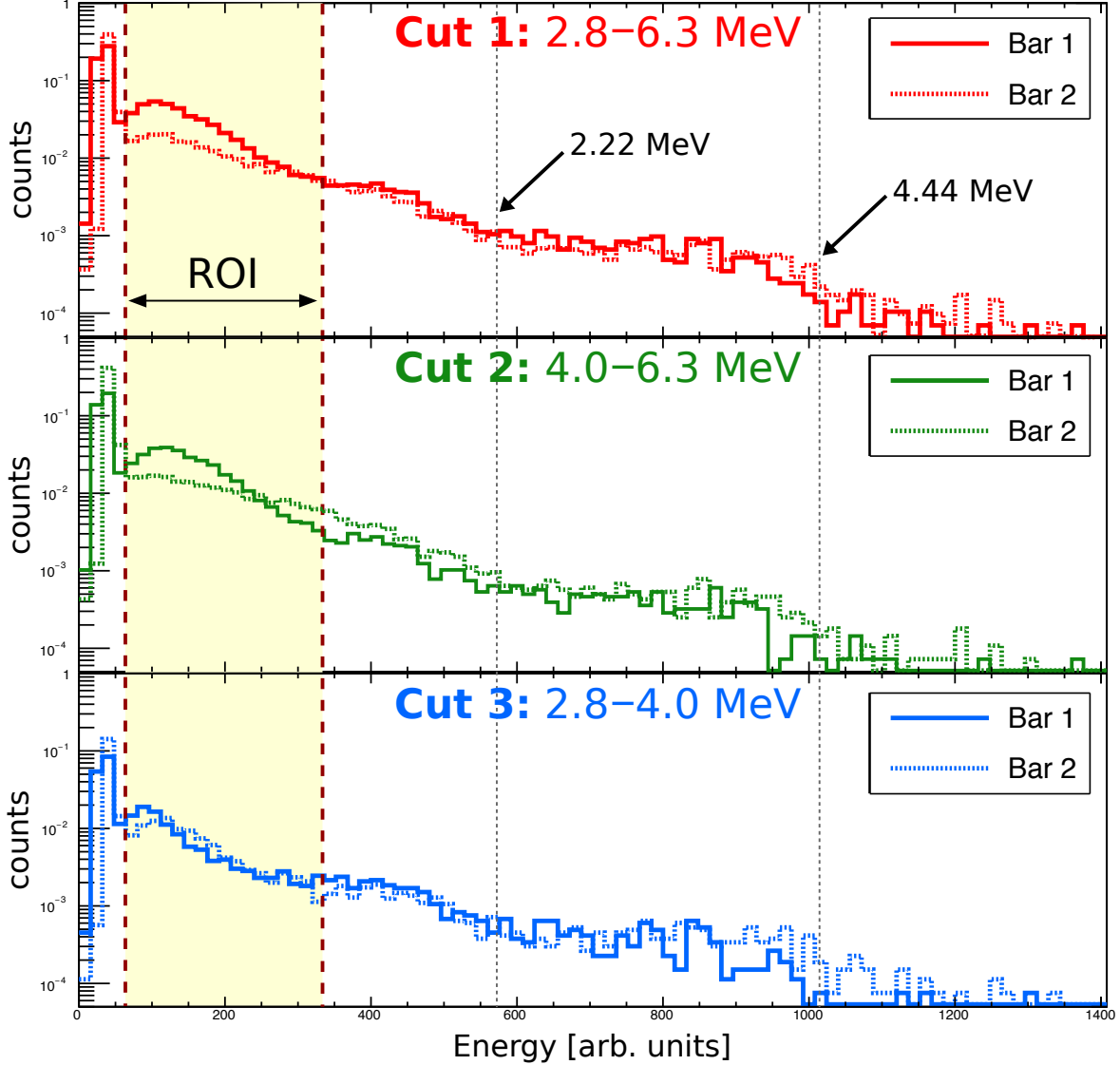


Figure 4.2.2: Deposited-energy spectra for tagged neutrons. Solid histograms: PMT A of Bar 1. Dashed histograms: PMT B of Bar 2. Top panel: all neutrons identified by the island cut shown in Fig. 4.1.7. Middle Panel: highest-energy neutrons. Bottom panel: lowest-energy neutrons. Compton edges due to random γ -rays surviving the island cut are indicated with black arrows. ROI labels the energy region in which neutrons seem to preferentially deposit their energy.

In Fig. 4.2.2, no effort has been made to precisely calibrate the spectra for neutron energy as the relation between γ -ray light yield in MeV_{ee} and neutron light yield in MeV is complicated [27] and provides little insight into the dynamics of the spectrum that is not improved upon dramatically by considering TOF. Instead, the Compton edges corresponding to 2.22 MeV and 4.44 MeV γ -rays are shown together with QDC pedestals below channel 100 which provide some feeling for the energy calibration. In each panel, the number of counts has been normalized to unity.

When the entire neutron distribution is considered (Cut 1 – see panel 1), the deposited energy spectrum for Bar 1 shows a clear enhancement in the ROI over that corresponding to Bar 2. In an effort to unfold the energy dependence of this enhancement, Cut

2 (highest-energy neutrons, 4.0–6.3 MeV) and Cut 3 (lowest-energy neutrons, 2.8–4.0 MeV) were applied to the data. When only the highest-energy neutrons are considered (see panel 2), the asymmetry in the deposited-energy spectra persists, and Bar 1 still shows a clear enhancement over Bar 2 in the ROI. When only the lowest-energy neutrons are considered (see panel 3), the deposited-energy spectra for both Bar 1 and Bar 2 essentially agree in the ROI.

If a neutron undergoes a scatter resulting in an energetic proton in Bar 1, there will be less energy available to deposit in Bar 2. Further, if a neutron undergoes a scatter resulting in an energetic proton in Bar 2, there cannot have been much energy deposited in Bar 1. Based on the results shown in Fig. 4.2.2, it would seem that according to this very simple model, higher-energy neutrons preferentially undergo scatters resulting in energetic protons in Bar 1, leaving little energy to be detected in Bar 2. However, as the neutron energy decreases, it seems that the probability of scatters resulting in sufficiently energetic recoiling protons in both bars increases. In fact, the data seem to indicate that the lower the energy, the more symmetric the response of Bar 1 and Bar 2. Of course, this line of reasoning assumes only a single interaction in each bar, which may or may not be realistic. To better understand the detection dynamics, a dedicated simulation suite using GEANT4 [28] and/or MCNP-X [29] needs to be performed. Such a simulation suite is beyond the scope of this thesis, but is currently top priority for the project.

To summarize, from the point-of-view of deposited energy, the PUG bars in this configuration seem to have a sensitivity to neutron tracks.

4.2.2 Neutron-Tracking Study

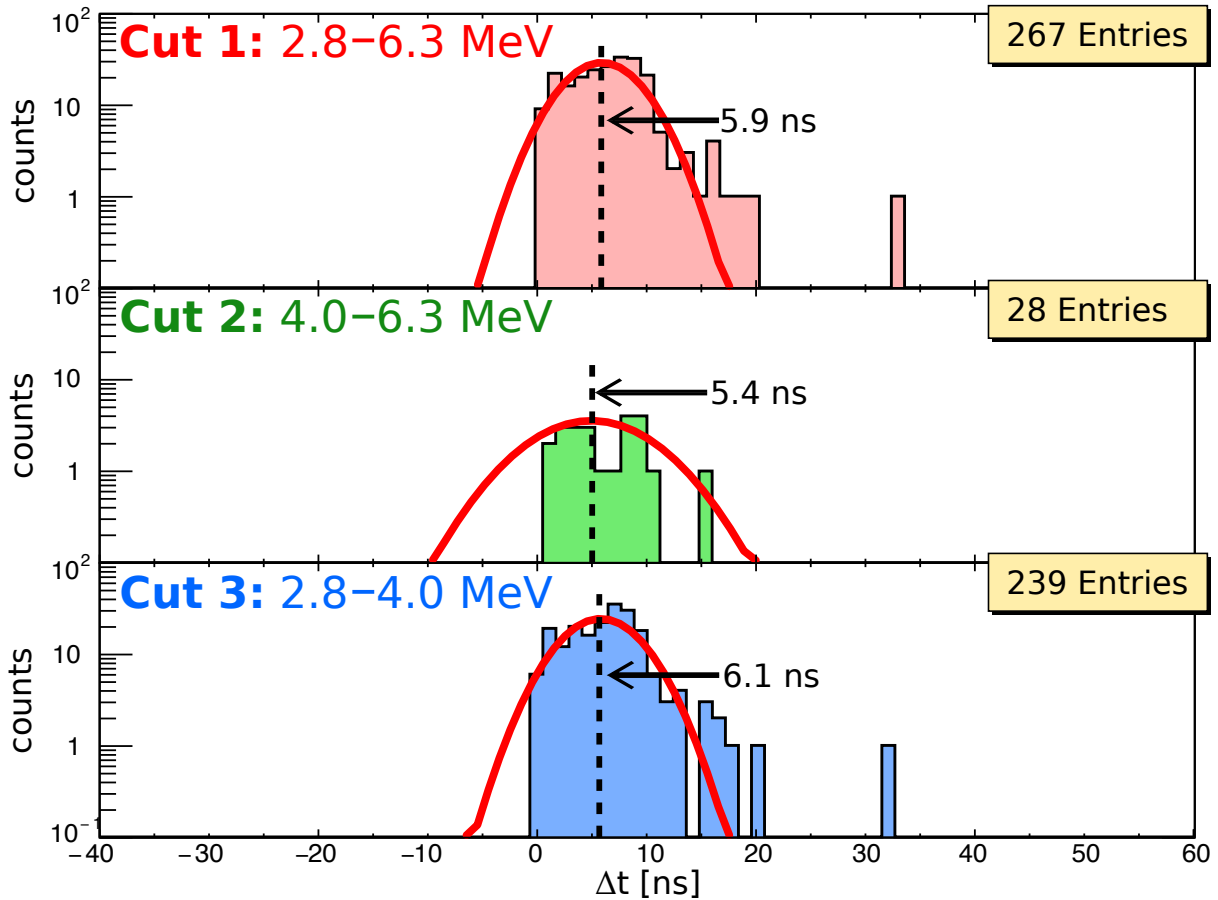


Figure 4.2.3: Flight-time spectra for tagged neutrons. Top panel: all neutrons identified by the island cut shown in Fig. 4.1.7. Middle panel: highest-energy neutrons. Bottom panel: lowest-energy neutrons. Gaussian fits are included to guide the eye and establish the mean values of the distributions shown (black arrow). The average values of the three distributions are 6.6, 6.2 and 6.7 ns for the top, middle and bottom panel, respectively.

Figure 4.2.3 shows flight-time spectra measured by PMT A for Bar 1 and PMT B for Bar 2 for events determined to be neutrons using the island-based cuts described in Sec. 4.1.3. Flight-time Δt represents the amount of time between signals being generated in Bar 1 and Bar 2 and was determined by evaluating the difference in the event timing measured with TDCs. Note that enforcing this timing condition on the events identified as neutrons by the island cut in the NE213 detector resulted in a dramatic reduction in the number of events producing the sought-after signals in the PUG bars. When the entire neutron distribution is considered (Cut 1 – see panel 1), the flight-time spectrum is centered at 5.9 ns. When highest-energy neutrons are considered (Cut 2 – see panel 2), the flight-time spectrum is centered at 5.4 ns. When lowest-energy neutrons are considered (Cut 3 – see panel 3), the flight-time spectrum is centered at 6.1 ns. Thus, a clear correlation between the neutron energy and flight-time between Bar 1 and Bar 2 is observed. Furthermore, the mean flight time measured for the three cuts also follows expectations, as the mean flight time of the highest-energy neutrons (Cut 2 – panel 2) is less than the mean flight time of the lowest-energy neutrons (Cut 3 – panel 3).

Consider Fig. 4.2.4, where two extreme neutron trajectories are illustrated.

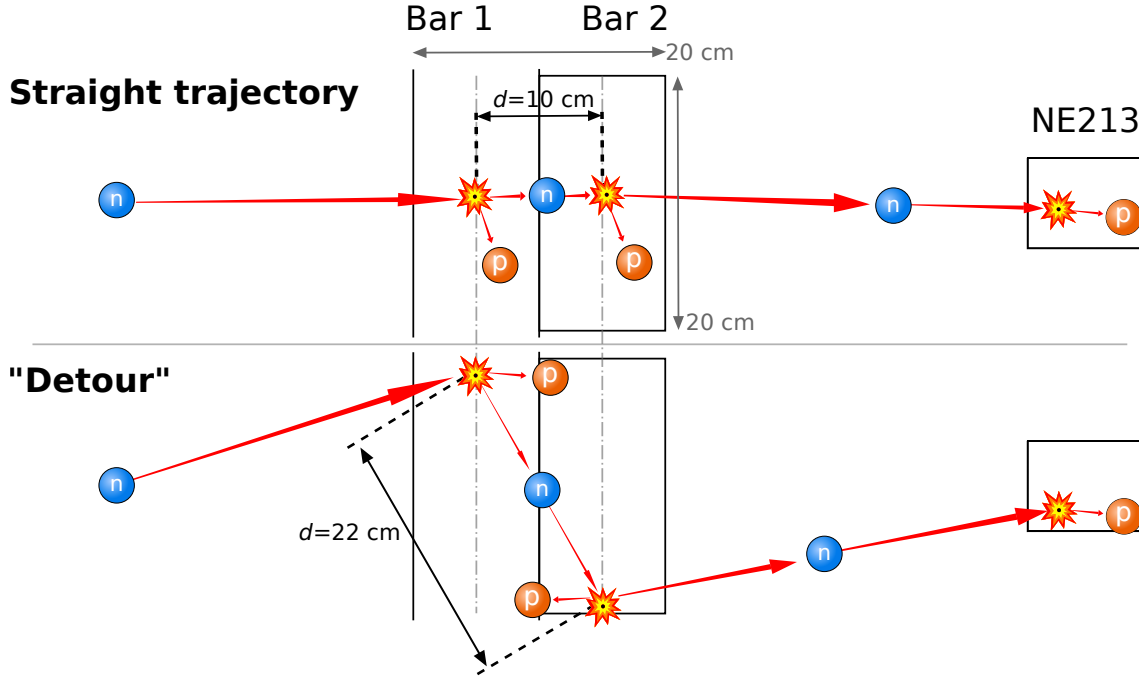


Figure 4.2.4: Extreme neutron trajectories. The top panel shows a straight trajectory and the bottom panel a “Detour” candidate. The straight trajectory travels a mean distance $d = 10$ cm between the two points of interaction. The “Detour” candidate travels a mean distance $d = 22$ cm between the two points of interaction. This results in different flight times.

Assuming the distributions in Fig. 4.2.3 correspond to a neutron passing through Bar 1 and Bar 2, a “straight” neutron trajectory corresponds to a mean distance between the two interactions of $d = 10$ cm (each bar is 10 cm thick, and an interaction on the midplane is assumed) and Δt is the flight time across this distance. The average neutron kinetic energy (\bar{E}_k^n) for each of Cuts 1, 2 and 3 gives the *expected* flight time as:

$$\Delta t = \frac{d}{v_n} = \frac{d}{c\sqrt{\frac{2\bar{E}_k^n}{m_n}}}, \quad (4.2.1)$$

where v_n is the velocity of the neutron and the neutron mass $m_n \approx 939.6$ MeV/ c^2 .

As summarized in Table 4.2.1, if a straight-neutron trajectory is considered and the interaction between the neutron and the bars is assumed to occur, on average, in the center of the bars, then the measured flight-time distributions should occur at just under 4 ns. If a different neutron trajectory is considered and the interaction between the neutron and the bars is assumed to occur on average symmetrically and at the midplane of the bars, but at the edges as defined by the downstream bar, then the measured flight-time distribution will be longer. The “Detour” neutron would travel a distance $d = 22$ cm which would give a larger flight time of about 8 ns as shown in Table 4.2.1. Reality likely lies somewhere in between these two extreme situations. Again, the situation arises that to better understand the data, a dedicated simulation suite using GEANT4 and/or

MCNP-X will need to be performed.

Table 4.2.1 presents the measured and expected flight times Δt for $d = 10$ cm and $d = 22$ cm. The measured flight time is always slightly longer than the expected flight time, but the crude model discussed above is surprisingly accurate, and the measured flight times are reasonably close to what is expected. More data are clearly needed to determine whether-or-not the flight-time distributions are Gaussian as assumed, or perhaps have tails to longer flight times.

	\bar{E}_k^n [MeV]	Measured flight time Δt [ns]	Expected flight time [ns] ($d = 10$ cm)	Expected flight time [ns] ($d = 22$ cm)
Cut 1	5.9	6.0	3.4	7.4
Cut 2	5.4	4.7	3.2	7.0
Cut 3	6.1	6.4	3.9	8.7

Table 4.2.1: Measured flight time. The average neutron kinetic energy \bar{E}_k^n is obtained by averaging the energy range for each cut. The expected flight time for two different distances $d = 10$ cm and $d = 22$ cm is shown.

Finally, considering all neutrons identified by the NE213 detector, $\sim 10\%$ left a time-correlated signal in both Bar 1 and Bar 2, which was a surprisingly large number. The expected detection efficiency of fast neutrons in NE110 plastic scintillator according to generally accepted “rule-of-thumb” is around $1\%/cm$ at these energies [30], which indicates a 10% efficiency per bar and thus a 1% absolute efficiency for the same neutron to leave a signal in both bars. Further, 90% of the neutrons identified by the island cut in the NE213 detector which left a time-correlated signal in both Bar 1 and Bar 2 had energies below 4 MeV. Clearly, this needs to be studied further. The simulation suite suggested previously would again allow for the measured flight times to be studied in detail and a better interpretation of the results.

Chapter 5

Summary

5.1 Overview

The ultimate goal of this project is the development of a fast-neutron detector which can be used to investigate and diagnose high-energy background, mainly from pulse-correlated prompt fast-neutrons, at spallation facilities. The Portable Fast-Neutron Diagnostic Detector (PUG) is planned to consist of two arrays of neutron-sensitive detectors which can move independently of each other that potentially could allow for TOF measurements with tracking capabilities.

In this thesis, the detector system was conceptualized and designed. Detector layout, material composition and support structure were all carefully considered. The scintillator material was prepared and assembled together with light guides and PMTs to make the two prototype bars. Extensive testing of the scintillator material was performed using cosmic-ray muons, which were used to study scintillator-light attenuation, position resolution and energy resolution. A comprehensive study of the fast-neutron energy response of the two PUG bars was then performed in the 2.8–6.3 MeV neutron energy range, and finally, fast-neutron tracking capabilities of the setup were investigated.

5.2 Conclusions

Two clear conclusions may be drawn from the PUG-bar results for the configuration considered.

Conclusion 1: neutron-energy deposition

As shown in Fig. 4.2.2, the neutron response of the PUG bars over the region-of-interest is clearly neutron-energy dependent. For neutron energies above 4 MeV, the response of Bar 1 is enhanced over that of Bar 2, while for neutron energies below 4 MeV, the responses of Bar 1 and Bar 2 are essentially the same.

Conclusion 2: flight time

As shown in Fig. 4.2.4, fast-neutron tracking with the present experimental setup is clearly possible. For neutron energies above 4 MeV, the number of neutrons successfully tracked is clearly less than for neutron energies below 4 MeV.

5.3 Outlook

The PUG prototype has thus produced results sufficient to warrant further study and development of the detector. The next steps in terms of the development of PUG are divided into “short term” and “long term”.

Short-term steps:

- develop an extensive simulation suite to better understand the measured behavior
- continue measurement program to increase the statistical certainty in the tracking measurement and to allow for the bars to be separated and thus further test their tracking capabilities

Long-term steps:

- assemble bars 3-8
- construct the PUG suspension frame
- develop of a dedicated data-acquisition system
- perform tests at an accelerator-based facility producing pulsed beams of mono-energetic neutrons such as LIBAF, the Lund University Ion Beam Analysis Facility
- perform tests at an spallation facility such as the spallation neutrons source at STFC Rutherford Appleton Laboratory, UK

5.4 Suggestions for Improvement

Several ways to improve the project are foreseen.

One of the largest drawbacks of the present experimental setup is the very low count rate for island neutrons in the NE213 detector. A straightforward method to increase this count rate would be to move the NE213 detector closer to Bar 2 so that the solid angle will increase. Another straightforward method to increase this count rate would be to increase the size of the NE213 detector, or even simply add another unit.

Once a setup with a higher count rate is configured, it will be feasible to vary the distance between Bar 1 and Bar 2 to study the neutron response and flight time as a function of distance between the bars. Alternatively, the NE213 detector could be fixed while the distance between Bar 1 (also fixed) and Bar 2 is varied. In this case, the neutron beam would be largely unaffected by the position of Bar 2, which would enable a direct comparison between the different positions. Information relating the distance between the bars to the neutron-energy response and flight-time response of the bars will be a huge step forwards towards understanding the functionality of PUG.

A study of the positional sensitivity for the detection of neutrons along each bar is also desirable. This would require an expansion of the current DAQ system to accommodate the four channels for the two PMTs per bar and the NE213 liquid scintillator. Since the scintillation light produced by a recoiling proton would give a signal in both PMTs, the

difference between their respective TDC values may be used to reconstruct the position along the bar where the neutron interacted.

Finally, even though PUG has been shown both to detect neutrons and even to track them, a potential redesign could alleviate the most difficult aspect of neutron tracking: neutron identification. It is likely very difficult to use plastic scintillator to identify neutrons by the signal they produce alone. To identify a neutron, a new setup is suggested to correlate a candidate neutron signal against the flight time between two detectors. The suggestion is to construct one (or even both) of the detectors employed based on liquid scintillators capable of PSD (such as NE213). This array could in principle be constructed of several smaller units which together cover an area comparable to the PUG bars. This hybrid (or even completely liquid-based) detector would facilitate neutron identification and could allow for substantially higher rates in the detectors due to superior particle identification capabilities.

Appendices

Appendix A

Contributions of the Author

The table and figure below shows the estimated time spent on the various tasks of the project. Total project time: 36 weeks.

Task	%	Description
Experiment	31	Setup, trial-and-error, testing, etc.
Analysis	25	Programming and analysis of data
Writing	11	Writing of this thesis
Design	8	CAD design of the detector, its frame and components
Logistics	8	Moving, documenting, shipping and other project management
Cutting	8	Experimenting with cutting of scintillator bars and final dimensioning
Assembly	6	Assembly of detector bars and components
Poster	3	Time spent on ICANS XXII poster and proceedings



Appendix B

Poster at ICANS XXII, 2017



Fast-Neutron Detector on Wheels

the Portable fast-neUtron diaGnostic project (PUG)

Nicholai Mauritzson^{1,2} - Philip M. Bentley^{2,3} - Kevin Fissum^{1,2} - Hanno Perrey^{1,2} - Douglas Di Julio^{1,2} - Carsten P. Cooper-Jensen^{2,3} - Emil Rofors¹ - Francesco Messi^{1,2}

1: Department of Nuclear Physics, Lund University, Sweden, 2: European Spallation Source ERIC, Sweden, 3: Department of Physics and Astronomy, Uppsala University, Sweden



Background at spallation sources

- High-energy secondaries
- Unwanted signal in instrumentation
- Beam-pulse correlated

Need

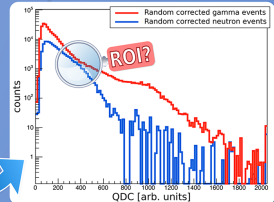
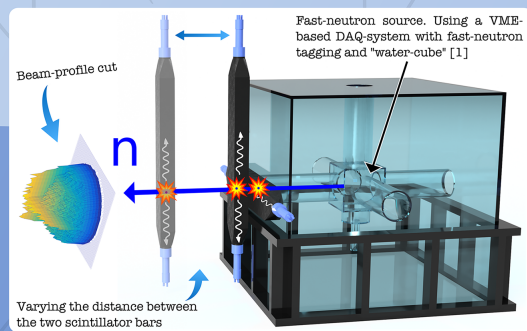
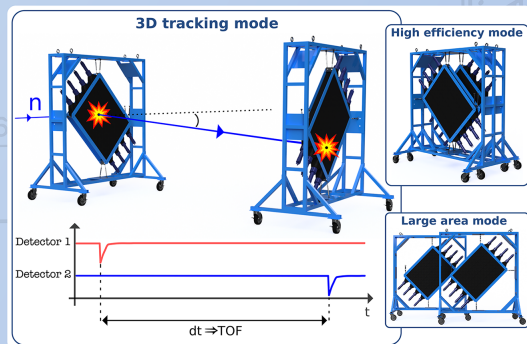
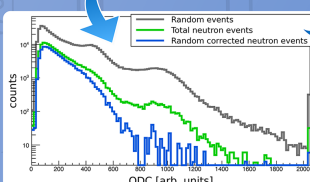
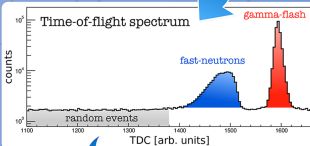
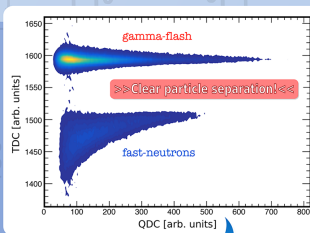
- Diagnostic detector
- Portable & large detection area
- Spatial resolution & energy

The Detector

- 8 plastic bars (NE110) & 16 PMTs
- Two independent detector arrays (4x4)
- Detector area: 0.64m²
- TOF functionality & 3D tracking
- Movable & suspendable

Experimental setup

- Initial tests with two scintillator bars
- Fast-neutron tagging



Outlook/Next step

- Further characterization & calibration
- Look into ROI above
- Assembly of full-size detector arrays
- Upgrade from NIM/CAMAC to digitizer
- Testing at spallation source



Author: Nicholai Mauritzson, nicholai.mauritzson@ess.se, ICANS 2017
 [1] Scherzinger, J., Annand, J. R. M., Davatz, G., Fissum, K. G., Gendotti, U., Hall-Wilton, R., ... & Nilsson, B. (2015). Tagging fast neutrons from a 241 Am/9 Be source. Applied Radiation and Isotopes, 98, 74-79.

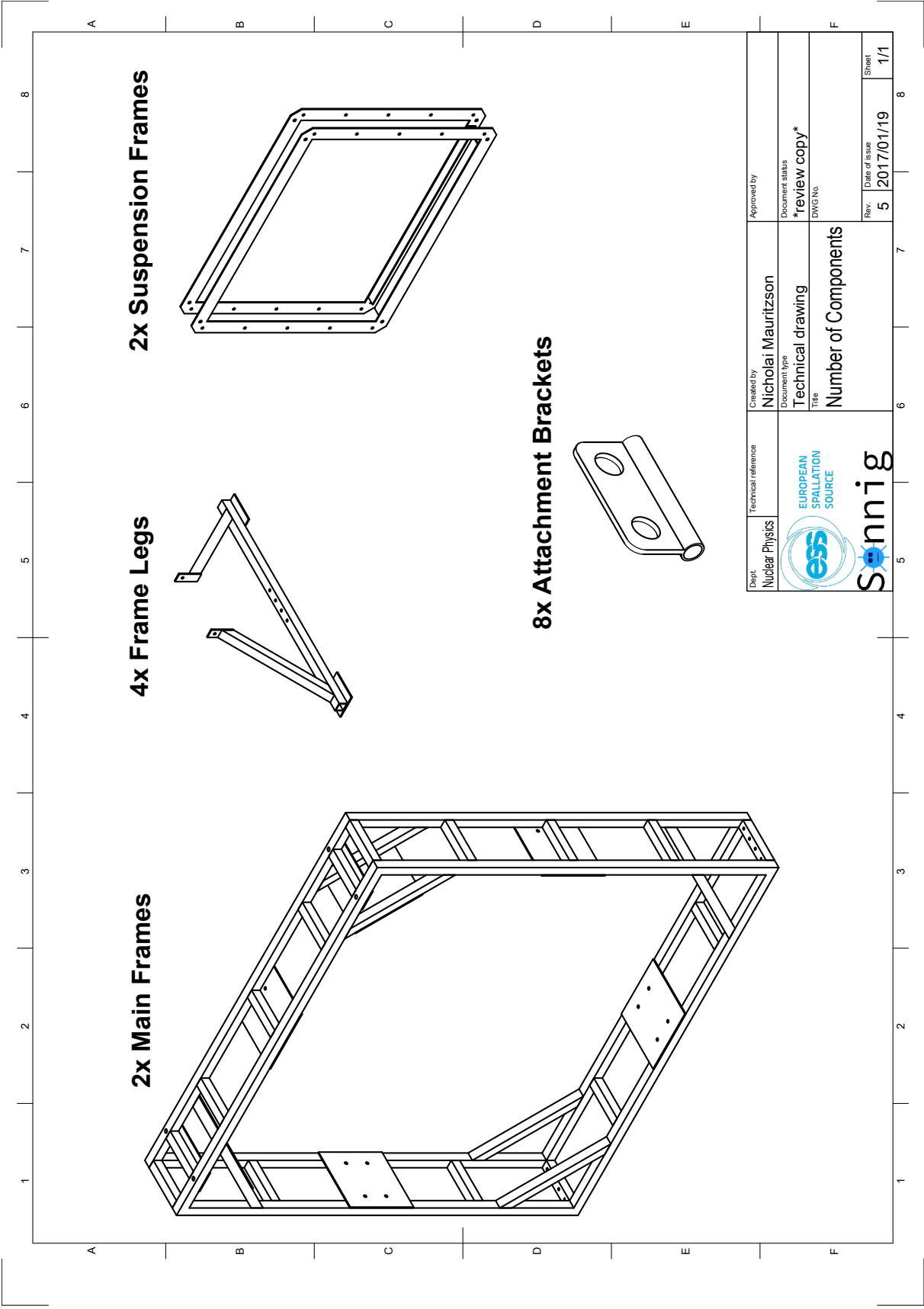
Appendix C

Technical Drawings and Bill of Materials

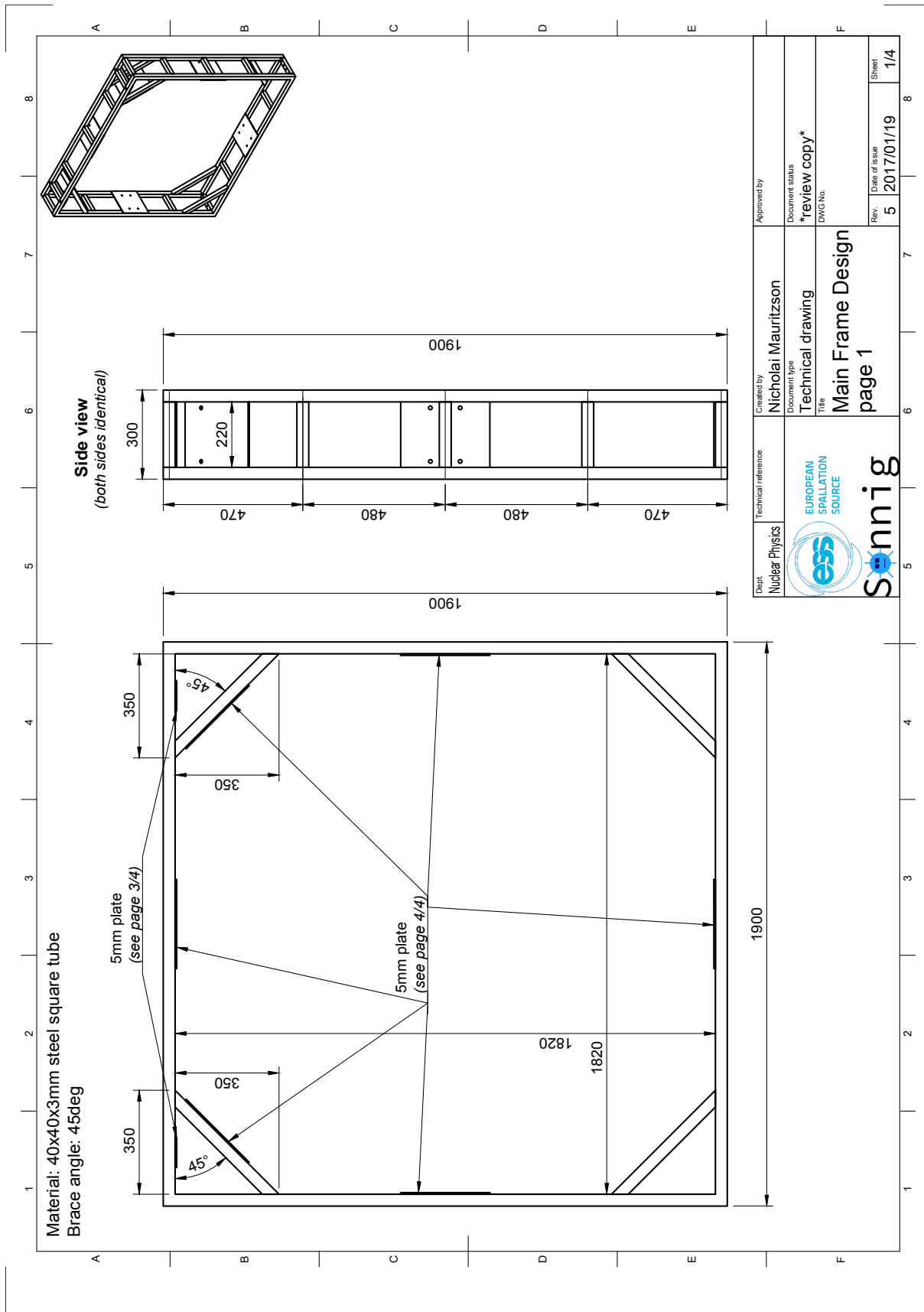
The bill of materials (BOM) and technical drawings of the full sized detector frame-assembly are shown here.


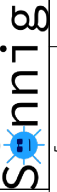
BOM:

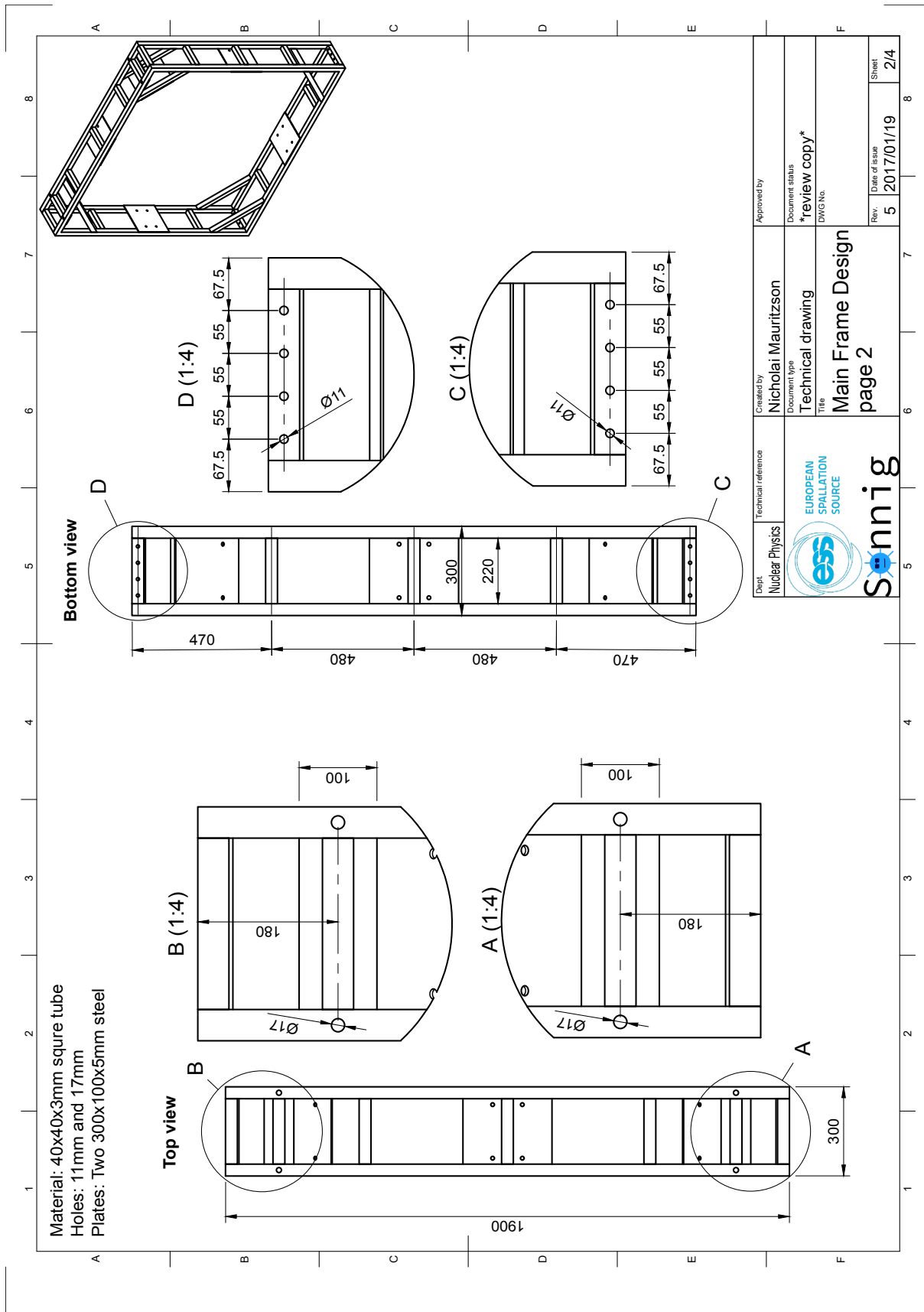
Item	pcs.	note
Main Frames	2x	See “Main Frame Design page 1-4”
Inner Frames	2x	See “Suspension Frame OVERVIEW page 1-3”
Frame Legs	4x	See “Legs Design”
Attachment Brackets	8x	See “Attachment Bracket”
Casters	8x	Ahlsell: 267175
Turn buckles (M10)	16x	Ahlsell: 280158
Eye bolts (M16)	8x	M16 fzv C15 DIN 580
Eye bolts (M12)	16x	M12 fzv C15 DIN 580
Hexbolt (M12)	8x	M6S A4/80 M12X130 DIN 931
Hexbolt (M10)	16x	M6S A4/80 M10X100 DIN 931
Hexbolt (M10)	8x	M6S A4/80 M10X65 DIN 931
Nyloc nuts (M16)	8x	A4/80 M16 DIN 985
Nyloc nuts (M12)	24x	A4/80 M12 DIN 985
Nyloc nuts (M10)	24x	A4/80 M10 DIN 985

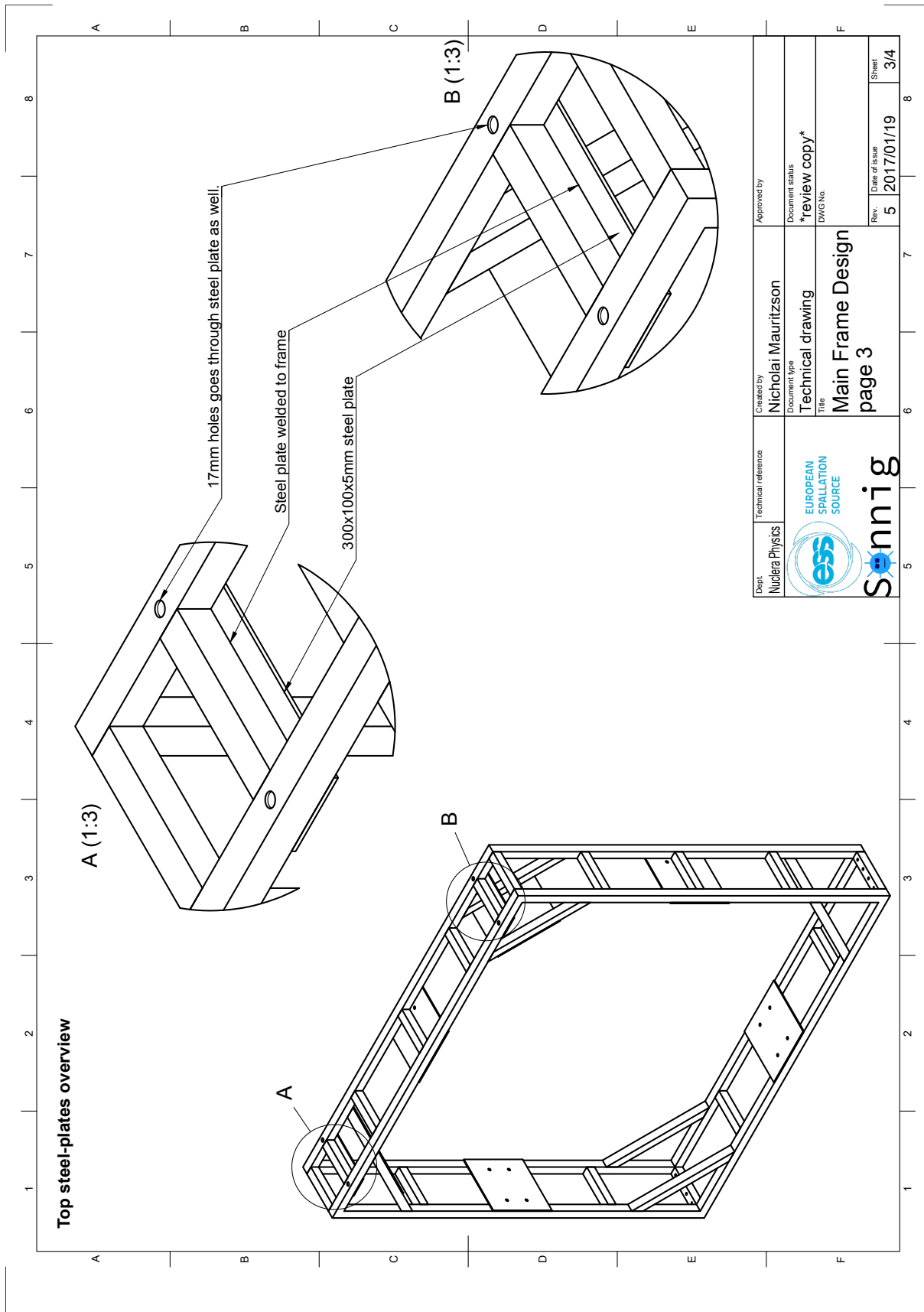


Dept Nuclear Physics	Technical reference	Created by Nicholai Mauritzson	Approved by
 EUROPEAN SPALLATION SOURCE	Document type Technical drawing	Document status *review copy*	
	Title Number of Components	DWG No.	
	Rev. 5	Date of issue 2017/01/19	Sheet 1/1



Dept Nuclear Physics	Technical reference	Created by Nicholai Mauritzson	Approved by
 	Document type Technical drawing	Document status *review copy*	
	Title Main Frame Design page 1	DWG No.	
		Rev. 5	Date of issue 2017/01/19
			Sheet 1/4





Top steel-plates overview

A (1:3)


B

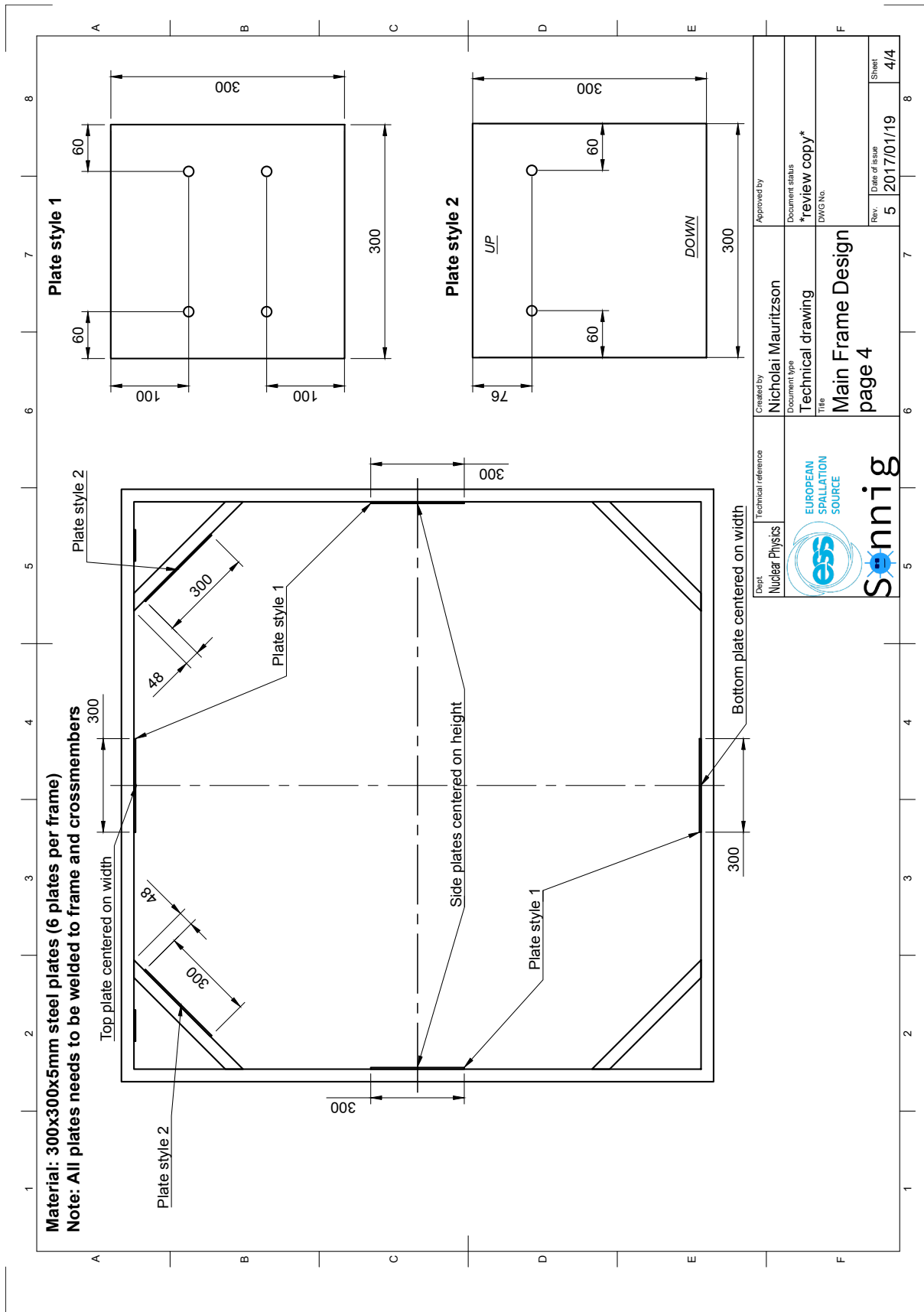
B (1:3)

17mm holes goes through steel plate as well.

Steel plate welded to frame


300x100x5mm steel plate

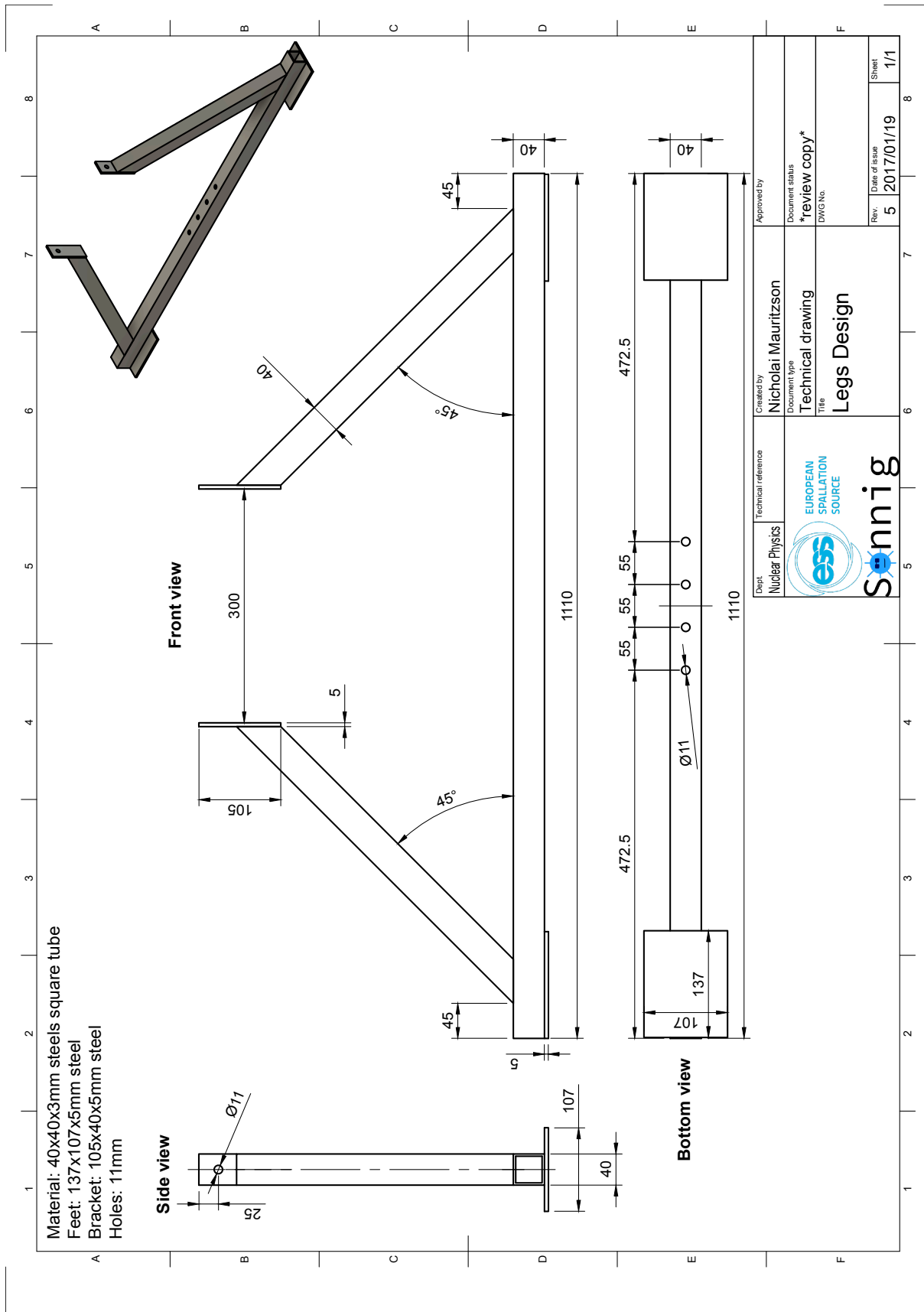
Dept Nuclear Physics	Technical reference	Created by Nicolai Mauritzson	Approved by
 EUROPEAN SPALLATION SOURCE	Document type Technical drawing	Document status *review copy*	
	Title Main Frame Design page 3		
		Rev. 5	Date of issue 2017/01/19
		Sheet 3/4	


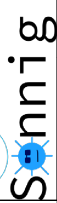


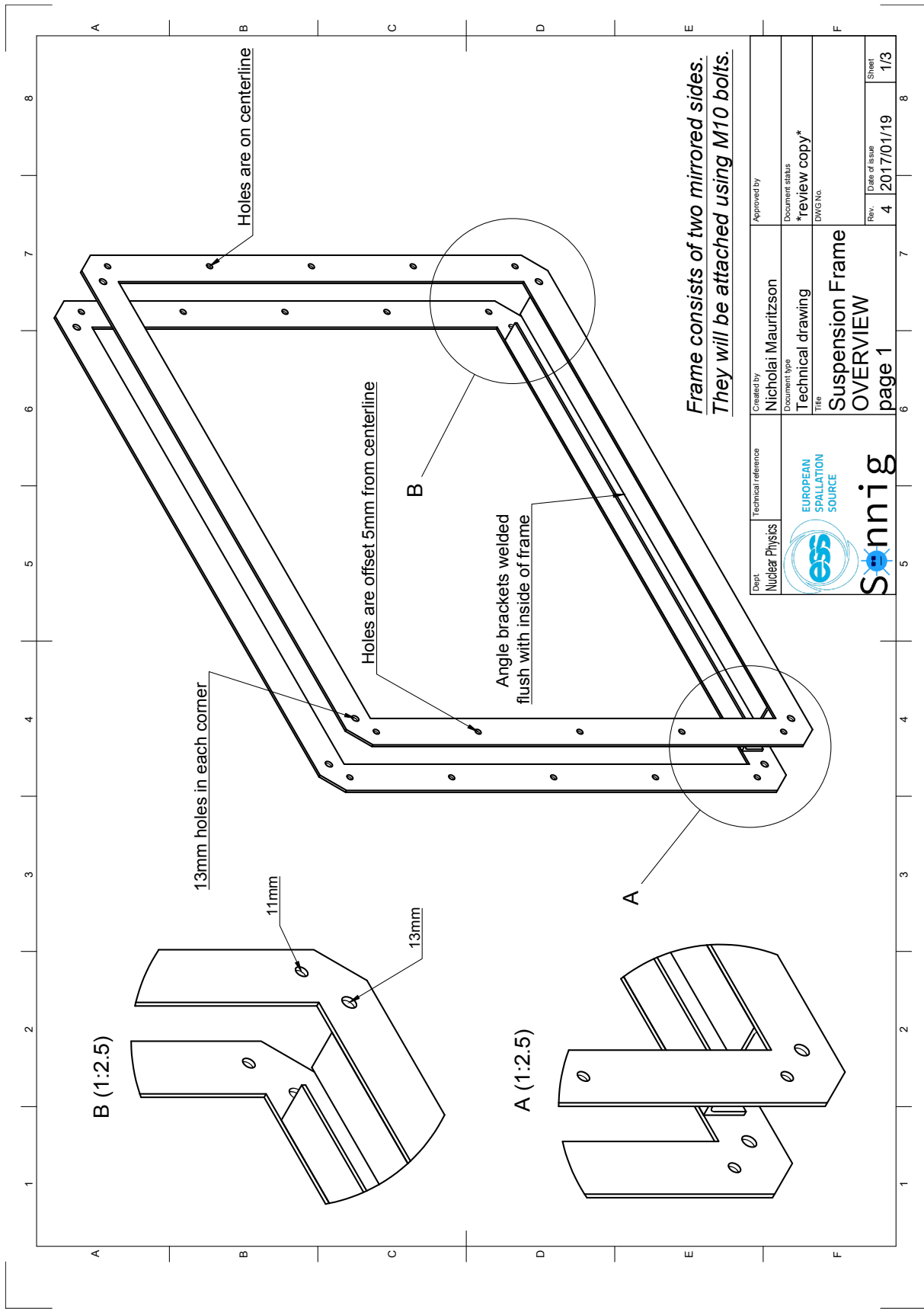
Material: 300x300x5mm steel plates (6 plates per frame)

Note: All plates needs to be welded to frame and crossmembers



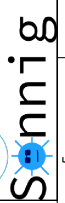
Dept	Nuclear Physics	Created by	Nicholai Mauritzson	Approved by	
Technical reference		Document type	Technical drawing	Document status	*review copy*
	 EUROPEAN SPALLATION SOURCE	Title	Main Frame Design		
	 Sonntag	page 4			
		Rev.	5	Date of issue	2017/01/19
		DWG.No.		Sheet	4/4

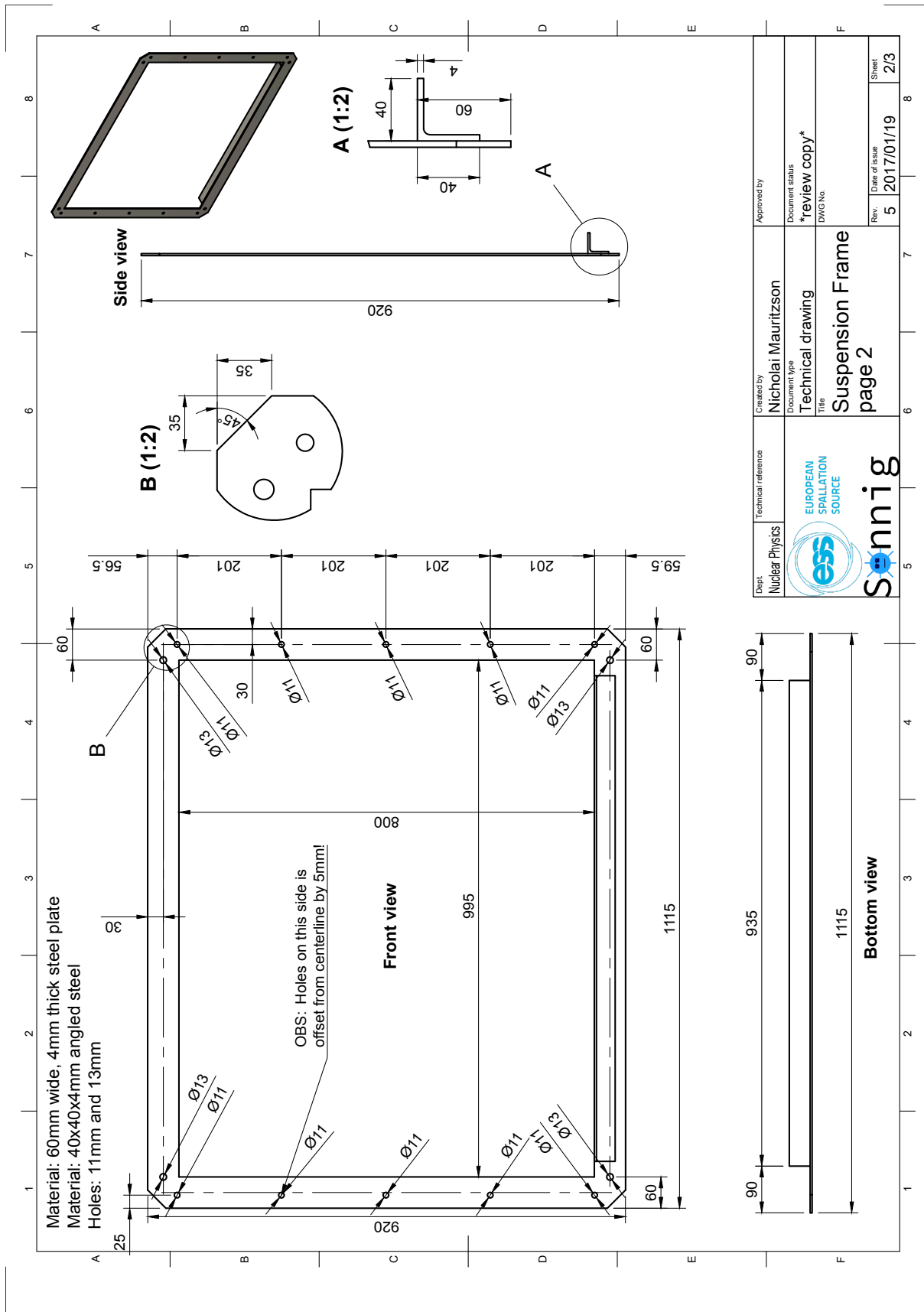


Dept	Nuclear Physics	Technical reference	Created by	Nicholai Mauritzson	Approved by	
			Document type	Technical drawing	Document status	*review copy*
			Title	Legs Design	DWG No.	
Rev.	5	Date of issue	2017/01/19	Sheet	1/1	

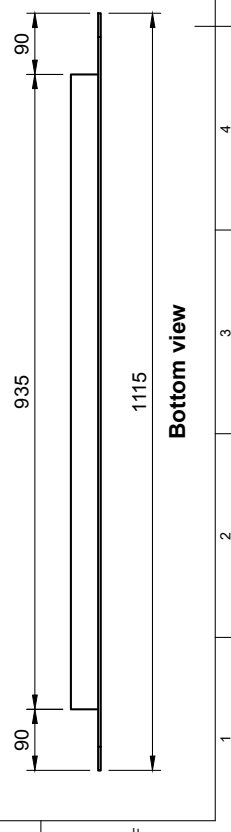
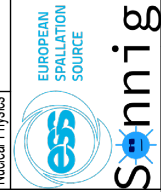


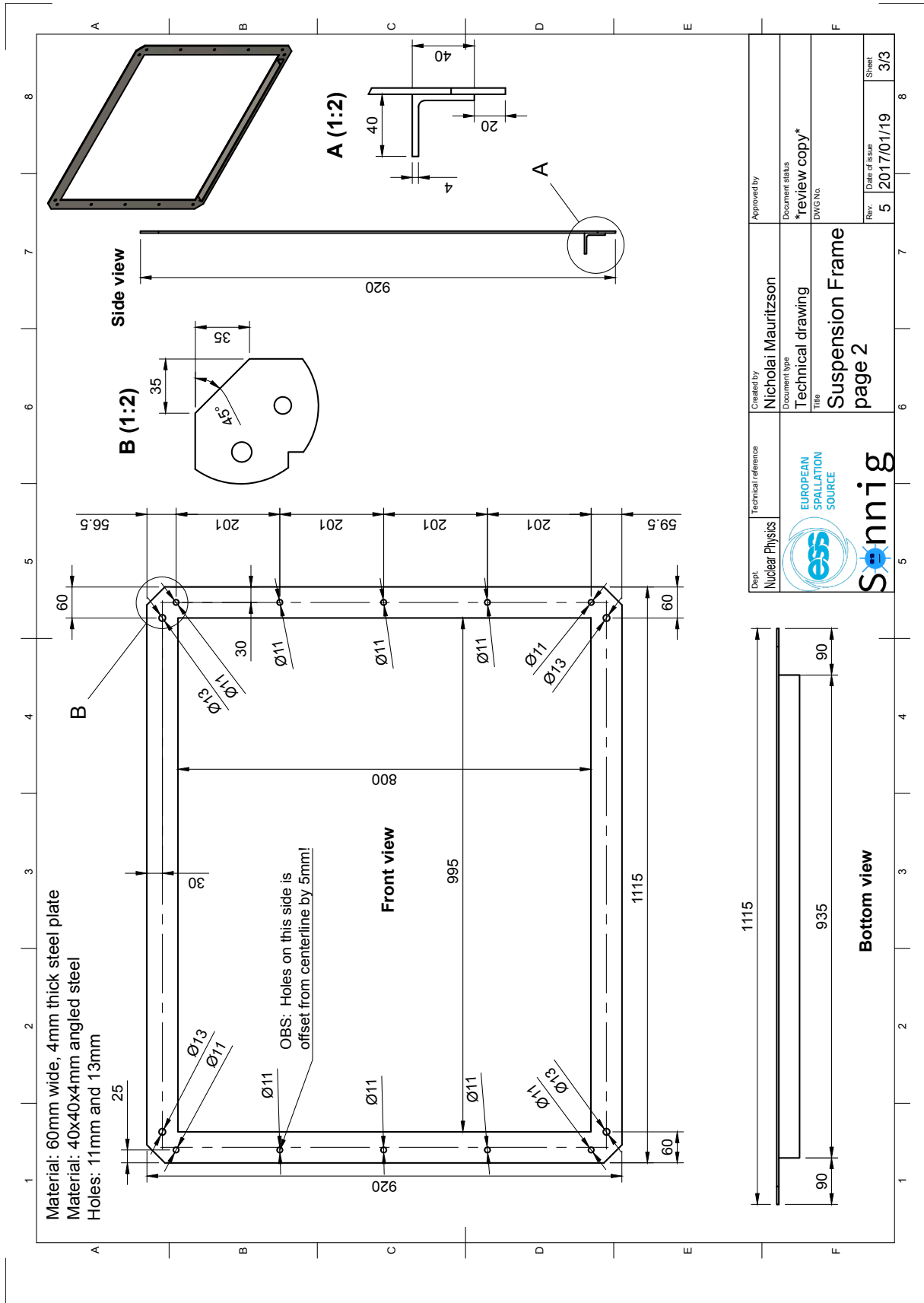
**Frame consists of two mirrored sides.
They will be attached using M10 bolts.**

Dept Nuclear Physics	Technical reference	Created by Nicholai Mauritzson	Approved by
		Document type Technical drawing	Document status *review copy*
	Title Suspension Frame OVERVIEW		
page 1			Rev. 4
Date of issue 2017/01/19			Sheet 1/3

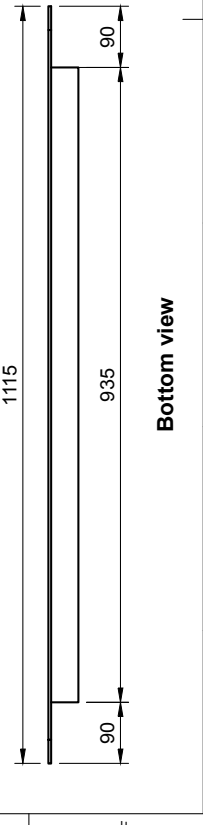


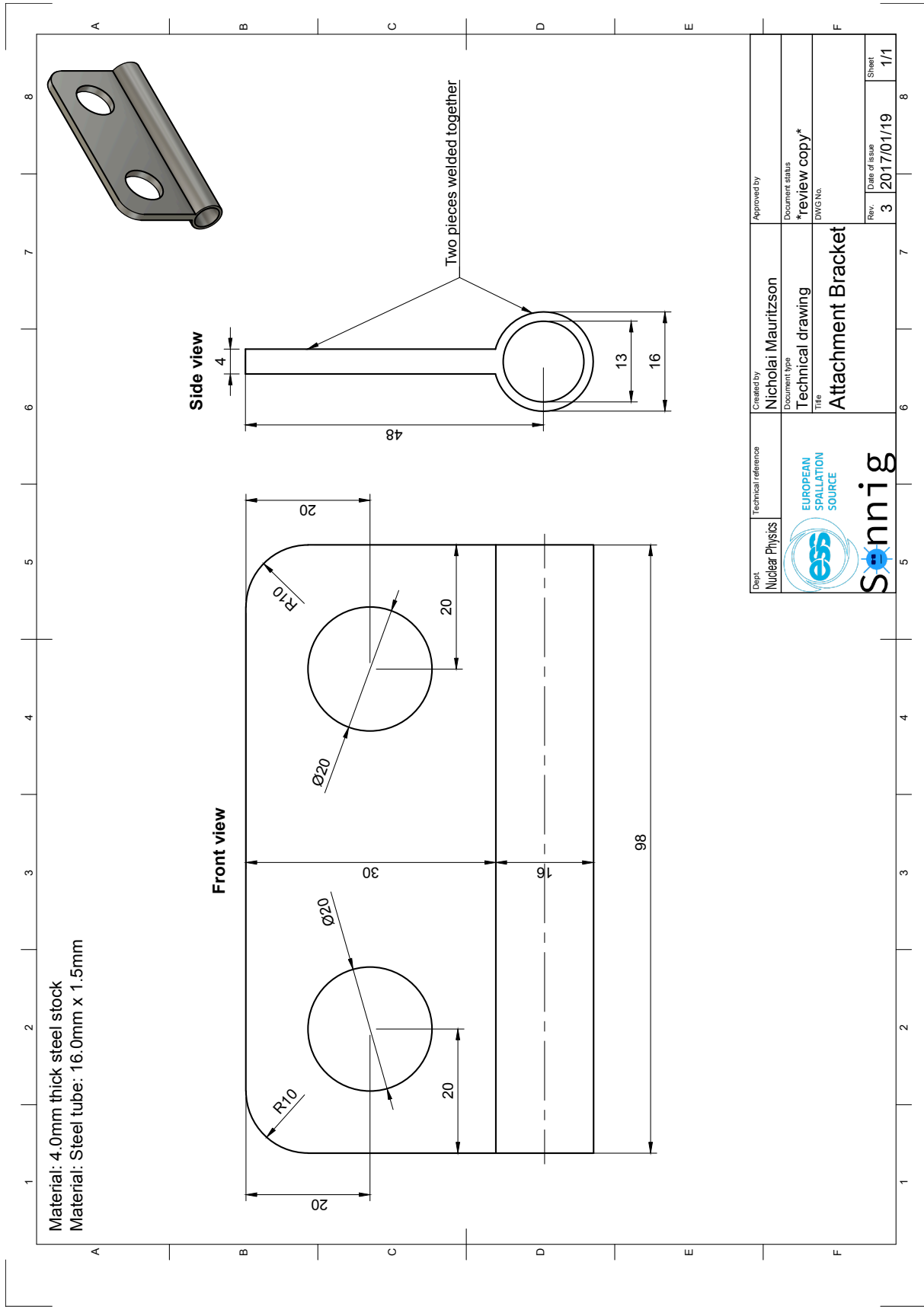
Dept	Nuclear Physics	Technical reference	Created by	Approved by
			Nicholai Mauritzson	
			Document type	Document status
			Technical drawing	*review copy*
			Title	DWG No.
			Suspension Frame	
			page 2	
			Rev.	Date of issue
			5	2017/01/19
			Sheet	
				2/3


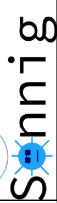




Dept	Nuclear Physics	Technical reference	Created by	Nicholai Mauritzson	Approved by	
			Document type	Technical drawing	Document status	*review copy*
			Title	Suspension Frame	DWG No.	
				page 2	Rev.	5
					Date of issue	2017/01/19
					Sheet	3/3





Dept Nuclear Physics	Technical reference	Created by Nicholai Mauritzson	Approved by
 EUROPEAN SPALLATION SOURCE	Document type Technical drawing	Document status *review copy*	
	Title Attachment Bracket		DWG No.
		Rev. 3	Date of issue 2017/01/19
		Sheet 1/1	

Bibliography

- [1] M Åberg, N Ahlfors, R Ainsworth, C Alba-Simionesco, S Alimov, N Aliouane, B Alling, Kasper Grann Andersson, Niels Hessel Andersen, and Britt Rosendahl Hansen. *ESS technical design report*. European Spallation Source, 2013.
- [2] James Chadwick. Possible existence of a neutron. *Nature*, 129(3252):312, 1932.
- [3] DB Lichtenberg and Wuk Namgung. Effects of diquarks and mesons on baryon magnetic moments. *Physical Review D*, 40(5):1606, 1989.
- [4] Günter Siegfried Bauer. Physics and technology of spallation neutron sources. *Nuclear Instruments and Methods in Physics Research Section A: Accelerators, Spectrometers, Detectors and Associated Equipment*, 463(3):505–543, 2001.
- [5] GJ Russel. Spallation physics—an overview. *ICANS*, 11:291, 1991.
- [6] Shin Takeda, Jiang Guo, Shinya Morita, Hirohisa Ono, Tatsuro Oda, Junichi Kato, Hirotaka Sato, Masahiro Hino, Yutaka Yamagata, and Michihiro Furusaka. Development of highly-mechanically polished metal-substrate for neutron supermirrors. In *Journal of Physics: Conference Series*, volume 528, page 012011. IOP Publishing.
- [7] DD DiJulio, CP Cooper-Jensen, H Perrey, K Fissum, E Rofors, J Scherzinger, and PM Bentley. A polyethylene-b 4 c based concrete for enhanced neutron shielding at neutron research facilities. *Nuclear Instruments and Methods in Physics Research Section A: Accelerators, Spectrometers, Detectors and Associated Equipment*, 2017.
- [8] DD DiJulio, Carsten P Cooper-Jensen, H Björgvinsdóttir, Z Kokai, and Phillip M Bentley. High-energy in-beam neutron measurements of metal-based shielding for accelerator-driven spallation neutron sources. *Physical Review Accelerators and Beams*, 19(5):053501, 2016.
- [9] Glenn F Knoll. *Radiation detection and measurement*. John Wiley and Sons, 2010.
- [10] Brian Robert Martin and Graham Shaw. *Particle physics*. John Wiley and Sons, 2016.
- [11] McClellan Nuclear Research Center, UC Davis. <http://mnrc.ucdavis.edu/radiography.html>. Accessed: 2017-05-02.
- [12] Douglas D DiJulio, Konstantin Batkov, John Stenander, Natalia Cherkashyna, and Phillip M Bentley. Benchmarking geant4 for spallation neutron source calculations. In *Journal of Physics: Conference Series*, volume 746, page 012032. IOP Publishing.

- [13] Douglas D DiJulio, Nataliia Cherkashyna, Julius Scherzinger, Anton Khaplanov, Dorothea Pfeiffer, Carsten P Cooper-Jensen, Kevin G Fissum, Kalliopi Kanaki, Oliver Kirstein, and Georg Ehlers. Characterization of the radiation background at the spallation neutron source. In *Journal of Physics: Conference Series*, volume 746, page 012033. IOP Publishing.
- [14] Nataliia Cherkashyna, Kalliopi Kanaki, T Kittelmann, U Filges, Pascale Deen, K Herwig, G Ehlers, G Greene, J Carpenter, and Robert Connatser. High energy particle background at neutron spallation sources and possible solutions. In *Journal of Physics: Conference Series*, volume 528, page 012013. IOP Publishing.
- [15] Michael BR Smith, Erik B Iverson, Franz X Gallmeier, and Barry L Winn. Mining archived hyspec user data to analyze the prompt pulse at the sns. Report, Oak Ridge National Laboratory (ORNL), Oak Ridge, TN (United States). Spallation Neutron Source, 2015.
- [16] Graham Roger Stevenson and RH Thomas. A simple procedure for the estimation of neutron skyshine from proton accelerators. *Health physics*, 46(1):115–122, 1984.
- [17] William R Leo. *Techniques for nuclear and particle physics experiments: a how-to approach*. Springer Science and Business Media, 1994.
- [18] Thomas K Gaisser. Cosmic rays and particle physics. *Comments on Nuclear and Particle Physics*, 11(1):25–39, 1982.
- [19] S Baccaro, K Blazek, F De Notaristefani, P Maly, JA Mares, R Pani, R Pellegrini, and A Soluri. Scintillation properties of yap: Ce. *Nuclear Instruments and Methods in Physics Research Section A: Accelerators, Spectrometers, Detectors and Associated Equipment*, 361(1-2):209–215, 1995.
- [20] Emil Rofors. Fast Photoneutron Detection. 2016. Student Paper.
- [21] <http://www.svemek.se>. Svedala Mekaniska AB (SveMek), Företagsgatan 13, 233 51 Svedala, Sweden.
- [22] Anthony Clarkson, Dave G Ireland, Ramsey Al Jebali, Ralf Kaiser, Scott Lumsden, David Mahon, David Mountford, Matt Ryan, Craig Shearer, and Guangliang Yang. Characterising encapsulated nuclear waste using cosmic-ray muon tomography (mt). In *Advancements in Nuclear Instrumentation Measurement Methods and their Applications (ANIMMA), 2015 4th International Conference on*, pages 1–7. IEEE.
- [23] LG Greeniaus. *TRIUMF Kinematics Handbook*. TRIUMF, 1987.
- [24] John Annand. Personal communication. 2017.
- [25] Julius Scherzinger, JRM Annand, G Davatz, KG Fissum, U Gendotti, Richard Hall-Wilton, E Håkansson, R Jebali, Kalliopi Kanaki, and Magnus Lundin. Tagging fast neutrons from an 241 am/9 be source. *Applied Radiation and Isotopes*, 98:74–79, 2015.
- [26] J Scherzinger, R Al Jebali, JRM Annand, KG Fissum, R Hall-Wilton, K Kanaki, M Lundin, B Nilsson, H Perrey, and A Rosborg. The light-yield response of a ne-213 liquid-scintillator detector measured using 2–6mev tagged neutrons. *Nuclear*

Instruments and Methods in Physics Research Section A: Accelerators, Spectrometers, Detectors and Associated Equipment, 840:121–127, 2016.

- [27] Julius Scherzinger. Neutron Irradiation Techniques. 2016. PhD Thesis.
- [28] Sea Agostinelli, John Allison, K al Amako, J Apostolakis, H Araujo, P Arce, M Asai, D Axen, S Banerjee, and G Barrand. Geant4—a simulation toolkit. *Nuclear instruments and methods in physics research section A: Accelerators, Spectrometers, Detectors and Associated Equipment*, 506(3):250–303, 2003.
- [29] Denise B Pelowitz. Mcnpx user’s manual version 2.5. 0. *Los Alamos National Laboratory*, 76, 2005.
- [30] John Annand. Personal communication. 2016.

Appreciation

I would like to thank all the wonderful people and groups with whom I have had the pleasure of working with for the past 9 months. To start off, a huge thanks to the Neutron Optics and Shielding Group of ESS, for giving me this amazing project in the first place, as well as a very generous stipend. I would especially like to thank Douglas Di Julio for your all your support and for always taking time with me when I needed it. Also, thank you Carsten Cooper-Jensen for your feedback and general advice throughout the project. I would like to thank the Detector Group of ESS, for their encouragement and support of the project. To Kevin Fissum and Hanno Perrey, thank you for all your patience and support during the project as well as your steady encouragement of me personally. Thank you. To the rest of the SONNIG group: Francesco Messi, Julius Scherzinger and Emil Rofors, thank you for all your help and the relaxed and fun working environment your all help to create. I would also like to thank John Annand and Ramsey Al Jebali of the University of Glasgow for all your invaluable input and help during this time. Finally, to my fellow students which I have had pleasure of sharing an office with during this time, Amanda Jalgén and Jessica Delgado. Thank you for all the discussions we have had, your support and of course the Spanish lessons.